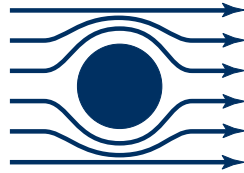Technische
Universität
München

Walther-Meißner
Institut

Bayerische
Akademie
der Wissenschaften

Spin Seebeck effect: a powerful probe for magnon properties in compensated ferrimagnets

Master's thesis

Maxim Dietlein

Supervisor: Prof. Dr. Rudolf Gross

Advisor: Dr. Stephan Geprägs

Garching – June 22, 2020

Contents

1. Introduction

Since at least when the giant magnetoresistance in magnetic multilayers was discovered in 1988, the vast opportunities by utilizing the spin degree of freedom in information technology started to emerge [1, 2]. Form that point on, a lot of research was conducted in the field of spin-based electronics investigating the influence of the spin on the conductivity of electrons. Together with further development of thin film fabrication techniques, this resulted in the great success of the hard disk drive, which is part of the everyday life today [3]. Another prominent example of modern spin-based electronics is represented by the successful development of the magnetic random access memory, which is a non-volatile memory and is commercially available since 2006 [4]. Nowadays, the modern research field spintronics, which further evolved from those great scientific findings, investigates spin currents carried by magnons, spin-triplet supercurrents, superconducting quasi-particles and so on [5]. One of the major research objectives is the improvement of modern electronics in terms of computational speed and energy efficiency by building spin current based logical devices. Therefore, further improvements of the generation, the detection and the manipulation of pure spin currents are mandatory.

An important mechanism for the generation of spin currents is the spin Hall effect, which was theoretically predicted in 1971 and experimentally verified in 2004 [6–8]. The spin Hall effect describes the process which converts a charge current partially into a transverse spin current in heavy metals with strong spin-orbit coupling. Furthermore, the inverse spin Hall effect, which originates from identical microscopic mechanisms as the spin Hall effect, describes the partially conversion of a spin current into a transverse charge current. Thus, the spin Hall effect together with the inverse spin Hall effect are important mechanisms for the detection and generation of spin currents. Additionally, the spin Seebeck effect describes a further generation mechanism for spin currents which are thermally activated by a temperature gradient across the interface of an magnetically ordered insulator (MI) and an adjacent heavy metal (HM) [9]. The spin Seebeck effect is the most important thermoelectric effect in the new field of spin caloritronics describing the interaction of heat and spin currents [10].

Recently, the non-local transport properties of magnons in magnetically ordered insulators have drawn the attention of today's research. So far it was shown, that the diffusive magnon transport through a magnetically ordered insulator e.g. $Y_3Fe_5O_{12}$ [11] and $Gd_3Fe_5O_{12}$ [12] can be measured and controlled over distances of up to $40\,\mu m$. These important findings provide the foundation for three terminal magnon based devices [13], which are a promising candidate for logical spin current based devices. Analogously to electrons, magnons which contribute to diffusive spin currents behave according to the spin wave

dispersion relation, i.e. the magnon band structure of the magnetically ordered insulator. Thus, a detailed knowledge of the spin wave dispersion relation of a wide range of magnetically ordered material systems is mandatory for the progress towards logical spin current based devices. This is the mainspring of this work, which focuses on the relation of the spin Seebeck effect in $Tb_3Fe_5O_{12}$ | Pt heterostructures to the spin wave dispersion relation of $Tb_3Fe_5O_{12}$. The aim of this thesis is the experimental verification of this connection, which consequently proposes the spin Seebeck effect as a probe of the spin wave dispersion relation of magnetically ordered insulators. This would result in a simplified experimental accessibility of key properties of the spin wave dispersion relation via spin Seebeck effect experiments.

Up to now, the temperature profile of the amplitude of the spin Seebeck effect was connected to calculated spin wave dispersion relations in $Y_3Fe_5O_{12}$ [14, 15] and $Gd_3Fe_5O_{12}$ [16]. The ferrimagnetic insulator $Y_3Fe_5O_{12}$ is a prominent candidate for magnon based experiments due to its quasi-ferromagnetic behavior originating from two strongly antiferromagnetically coupled magnetic sublattices together with its record low Gilbert-damping. This results in a simple one-band spin wave dispersion relation up to $25\,\mathrm{meV}$ and a positive spin Seebeck effect amplitude in $Y_3Fe_5O_{12}$ | Pt heterostructures up to room temperature. On the other hand, the compensated ferrimagnetic insulator $Gd_3Fe_5O_{12}$ which consists of three antiferromagnetically coupled magnetic sublattices exhibits a more complicated spin wave dispersion relation. Thus, the temperature profile of the spin Seebeck effect amplitude in $Gd_3Fe_5O_{12}$ | Pt heterostructures is non-monotonic up to room temperature and additionally shows two sign changes [16]. Both temperature profiles of the spin Seebeck effect have been explained using calculated spin wave dispersion relations but these dispersion relations have not yet been experimentally verified.

Within this work, the compensated ferrimagnetic insulator $Tb_3Fe_5O_{12}$ is used as showcase material system. $Tb_3Fe_5O_{12}$ is similar to $Gd_3Fe_5O_{12}$ with three antiferromagnetically coupled magnetic sublattices. Since Gd has a large cross section to capture thermal neutrons [17], $Tb_3Fe_5O_{12}$ is chosen to allow for inelastic neutron scattering experiments. As a first step, the spin wave dispersion relation is determined experimentally by inelastic neutron scattering with polarization analysis on a $Tb_3Fe_5O_{12}$ single crystal at temperatures between $10\,\mathrm{K}$ and $280\,\mathrm{K}$. With the experimentally obtained data, the full spin wave dispersion relation is simulated using the software package SpinW. This spin wave dispersion relation is then connected to the temperature profile of the spin Seebeck effect in $Tb_3Fe_5O_{12}$ | Pt heterostructures. Overall, this work aims to provide the experimental proof for the already proposed connection of the temperature profile of the spin Seebeck effect amplitude to the spin wave dispersion relation.

This work consists of 6 chapters and is structured as follows: In **chapter 2**, the theory of spin currents and the spin Seebeck effect is summarized. Additionally, the material properties and crystallographic structure of the discussed material systems $Y_3Fe_5O_{12}$, $Gd_3Fe_5O_{12}$ and $Tb_3Fe_5O_{12}$ are presented. **Chapter 3** then outlines the theory of inelastic neutron scat-

tering experiments with polarization analysis. Subsequently, the experimental results of inelastic neutron scattering with polarization analysis on a $Tb_3Fe_5O_{12}$ single crystal at temperatures between $10\,K$ and $280\,K$ are presented and discussed. **Chapter 4** focuses on SpinW-simulations of the full spin wave dispersion relation of $Y_3Fe_5O_{12}$, $Gd_3Fe_5O_{12}$ and $Tb_3Fe_5O_{12}$. This results in a full description of the spin wave dispersion relation of $Tb_3Fe_5O_{12}$ from $10\,K$ to $280\,K$. The experimental procedure and sample preparation for spin Seebeck effect experiments is described in **chapter 5**. The obtained temperature profile of the spin Seebeck effect amplitude in $Tb_3Fe_5O_{12}$ single crystal | Pt heterostructures is then connected to the spin wave dispersion relation. Additionally, experiments on $Tb_3Fe_5O_{12}$ thin film | Pt heterostructures are discussed in detail. **Chapter 6** summarizes the results obtained within this work and gives an outlook on future investigations in context with the spin Seebeck effect and its connection to the spin wave dispersion relation.

2. Theory

This chapter outlines the theoretical foundations of this work. In the first part, an intuitive model is introduced to describe spin currents in electrically conducting materials. The second part describes the spin Hall effect and its inverse, which is used as a spin current detection mechanism. Subsequently, the theory behind the spin Seebeck effect is summarized and a qualitative expectation of the signal in field-dependent and angle-dependent spin Seebeck experiments is given. The last part of this chapter describes the key physical properties of rare-earth iron garnets, which are used as a sample system to gain insight into the connection between the spin Seebeck effect and the magnon dispersion relation.

2.1. Spin currents

Electrons do not only carry the charge $q = -e$ but also the intrinsic angular momentum $s = \pm\frac{\hbar}{2}$, the spin. Due to the quantization of space, this spin can only align parallel ($s = \frac{\hbar}{2} = \uparrow$) or anti-parallel ($s = -\frac{\hbar}{2} = \downarrow$) relative to a quantization axis. Thus, a full description of electronic currents needs to include the transport of angular momentum next to the charge transport. To cover this, Mott's two channel model will be introduced here [18].
Within the two channel model, a charge current $\mathbf{J}_C$ is described as the sum of two fully spin polarized charge currents:

$$\mathbf{J}_C = \mathbf{J}_\uparrow + \mathbf{J}_\downarrow \,, \tag{2.1}$$

where each current or channel ($\mathbf{J}_\uparrow$, $\mathbf{J}_\downarrow$) describes the charge current carried by electrons with $s = \pm\frac{\hbar}{2}$, respectively.
A pure charge current within this model consists of two equal sized fully spin polarized currents ($\mathbf{J}_\uparrow = \mathbf{J}_\downarrow$) (see Fig. 2.1.1 (a)). If the two channels have different absolute values ($|\mathbf{J}_\uparrow| \neq |\mathbf{J}_\downarrow|$), the model describes a spin polarized current, which transports electronic charge as well as spin angular momentum (see Fig. 2.1.1 (b)). The size of the spin current $\mathbf{J}_S$, which is flowing parallel or anti-parallel to the charge current, is proportional to the difference of the two channels ($\mathbf{J}_\uparrow - \mathbf{J}_\downarrow$):

$$\mathbf{J}_S = -\frac{\hbar}{2e} \left(\mathbf{J}_\uparrow - \mathbf{J}_\downarrow \right) \,. \tag{2.2}$$

Therefore, in this simple two channel model, a pure spin current consists of two equal sized channels flowing in opposite directions ($\mathbf{J}_\uparrow = -\mathbf{J}_\downarrow$) (see Fig. 2.1.1 (c)).
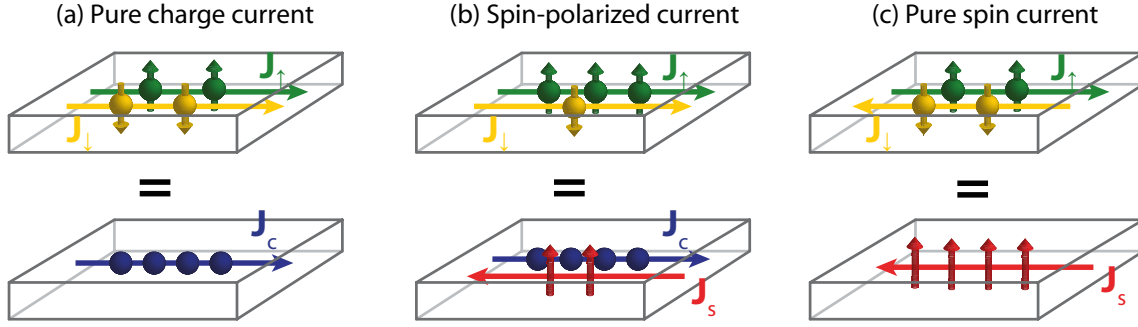
Figure 2.1.1.: Two channel model: (a) Pure charge current: the charge current is carried by $s = \uparrow$ and $s = \downarrow$ electrons in equal amounts. (b) Spin polarized current: the charge current is mainly carried by $s = \uparrow$ electrons. This current transports charge and spin angular momentum. (c) Pure spin current: $s = \uparrow$ electrons and $s = \downarrow$ electrons are moving in equal amounts in opposite direction. Only spin angular momentum is transported. Figure taken from Ref. [18].

The two channel model for spin currents can give an intuitive understanding of spin currents, but is only suitable for metals, where the spin current is carried by electrons.

In the framework of this thesis, we will discuss spin currents in ferrimagnetic insulators in detail. In those material systems, spin currents are carried by magnons. Magnons are the quasi-particle excitations of the magnetically ordered ground state of electron spins and can propagate through ordered spin systems according to their dispersion relation. Here, we will investigate the propagation of magnons in ferrimagnetic insulators caused by thermal excitation. The application of a finite temperature difference across the sample volume causes a finite temperature gradient ∇T. This temperature gradient leads to a finite gradient in the chemical potential of magnons, the so-called spin chemical potential $\nabla \mu_S$, which is resulting in a diffusive spin current

$$\mathbf{J}_S = \frac{\hbar}{2} \sigma_S \cdot \nabla \mu_S \tag{2.3}$$

parallel to the gradient in a closed boundary condition. The characteristics of this diffusive spin current are depending on the spin conductivity σ_S and the level of the chemical potential within the magnon dispersion relation. Thus, the characteristics can be tuned by experiments at different temperatures and with different materials. This work focuses on the group of the rare-earth iron garnets, since these material systems offer non-trivial magnon dipersion relations, long spin diffusion lengths and high spin conductivities σ_S.

2.2. Spin Hall effect

The spin Hall effect offers a possibility to generate spin currents in metals with large spin orbit coupling. Therefore, this effect is large in heavy metals such as Platinum.

Due to the spin Hall effect, a charge current $\mathbf{J}_C$ propagating through a heavy metal gets partially transformed into a transverse spin current $\mathbf{J}_S$ parametrized by

$$\mathbf{J}_S = \Theta_{SH} \left(-\frac{\hbar}{2e} \right) [\mathbf{J}_C \times \mathbf{s}] . \tag{2.4}$$

Here, s is the spin polarization and $\Theta_{\mathrm{SH}} = \frac{\sigma_{\mathrm{SH}}}{\sigma}$ is the dimensionless spin Hall angle, which is the ratio of the spin hall conductivity σ_{SH} and the electrical conductivity σ and determines the efficiency of the charge to spin current conversion. For the heavy metal Platinum, the spin Hall angle is $\Theta_{\mathrm{SH}} = 0.11$.
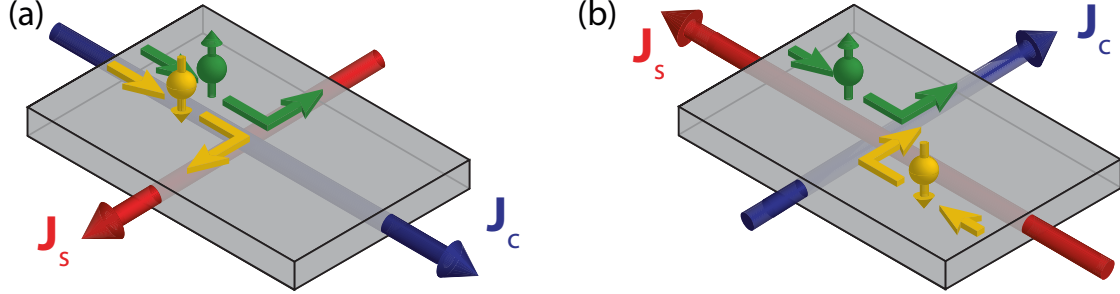
Figure 2.2.1.: (a) Spin Hall effect: A charge current $\mathbf{J}_{\mathrm{C}}$ propagating through a heavy metal with large spin orbit coupling is partially converted to a transverse spin current $\mathbf{J}_{\mathrm{S}}$. (b) Inverse spin Hall effect: A spin current $\mathbf{J}_{\mathrm{S}}$ is partially converted to a transverse charge current $\mathbf{J}_{\mathrm{C}}$. Both effects originate from the same microscopic mechanisms. Figure taken from Ref. [18].

There are three main mechanisms underlying the spin Hall effect. Two of them, the side-jump scattering and the skew scattering, are extrinsic and describe spin dependent scattering. The third mechanism is intrinsic and arising from the electronic band structure, which leads to spin dependent deflection of electrons [19].

The reciprocal effect is called the inverse spin Hall effect. Due to the inverse spin Hall effect, a spin current $\mathbf{J}_{\mathrm{S}}$ propagating through a heavy metal with large spin orbit coupling gets partially converted into a transverse charge current $\mathbf{J}_{\mathrm{C}}$, orthogonal to the spin polarization s of the spin current:

$$\mathbf{J}_{\mathrm{C}} = \Theta_{\mathrm{SH}} \left(-\frac{2e}{\hbar} \right) [\mathbf{J}_{\mathrm{S}} \times \mathbf{s}] . \tag{2.5}$$

The inverse spin Hall effect is providing a method to detect and quantify spin currents in an adjacent magnetic material. In this work, the inverse spin Hall effect is used to investigate the characteristics of spin currents in rare-earth iron garnets via a simple voltage measurement in an open boundary condition within the adjacent platinum layer.

2.3. Spin Seebeck effect

The spin Seebeck effect provides another possibility to generate spin currents. In contrary to the spin Hall effect, a heavy metal | magnetic insulator (HM | MI) interface with a temperature gradient parallel to the interface normal is mandatory, which results in a spin current propagating through the HM | MI interface.

2.3.1. Theory of the spin Seebeck effect

In this section, a brief summary of the theory behind the spin Seebeck effect, according to the work of Hoffman *et al.* is presented [20].
The dynamics inside the bulk of a magnetic material at temperatures well below the Curie temperature are described by the Landau-Lifshitz-Gilbert (LLG) equation in the following form:

$$\partial_t \mathbf{m} = -\gamma \mathbf{m} \times (\mathbf{H}_{\text{eff}} + \mathbf{h}_l) + \alpha \mathbf{m} \times \partial_t \mathbf{m} . \tag{2.6}$$

Here, $\mathbf{m} = \mathbf{M}/M_s$ is the unit-vector of the magnetization direction with the saturation magnetization M_S, $\mathbf{H}_{\text{eff}}$ the effective magnetic field acting on the magnetization $\mathbf{M}$, $\mathbf{h}_l$ a random 'white' field accounting for stochastic fluctuations according to the fluctuation-dissipation theorem, γ the gyromagnetic ratio and α the Gilbert-damping. The effective magnetic field

$$\mathbf{H}_{\text{eff}} = H_{\text{ext}} \cdot \mathbf{e}_z + A_x \nabla^2 \mathbf{m} \tag{2.7}$$

within this theory consists of the external magnetic field $\mathbf{H}_{\text{ext}} = H_{\text{ext}} \mathbf{e}_z$ along the **z**-direction and the exchange field $A_x \nabla^2 \mathbf{m}$. The random Langevin field $\mathbf{h}_l$ hereby is described by the correlator

$$< h_{l,i}(\mathbf{r}, t) h_{l,j}(\mathbf{r}', t') > = \frac{2\alpha}{\gamma M_s} k_B T(\mathbf{r}) \delta_{ij} \delta(\mathbf{r} - \mathbf{r}') \delta(t - t') . \tag{2.8}$$

The following part outlines the theory within the classical limit $\hbar\omega < k_B T$. In the first step the LLG equation is transformed into a spin density representation by application of the following transformation:

$$\mathbf{s} = s\mathbf{n} = -\frac{M_S}{\gamma} \mathbf{m} . \tag{2.9}$$

In this representation, $s = M_S/\gamma$ describes the saturated spin density and $\mathbf{n} = -\mathbf{m}$ its polarization direction. After the transformation, the LLG equation has the form

$$s(1 + \alpha \mathbf{n} \times) \partial_t \mathbf{n} + \mathbf{n} \times (H\mathbf{z} + \mathbf{h}) + \partial_i \mathbf{J}_{s,i} = 0 \tag{2.10}$$

where

$$\mathbf{J}_{s,i} = -A\mathbf{n} \times \partial_i \mathbf{n} \tag{2.11}$$

is defined as the spin current density in i-direction (i = **x**, **y**, **z**) and **h** is the random magnetic field taking thermal and quantum fluctuations into account, equivalent to Eq. (2.8). The magnetic field is redefined as $H = M_S H_{\text{ext}}$ and the exchange field as $A = M_S A_x = A_x s/\gamma$. The experimental setup which is considered within this theory is shown in Fig. 2.3.1. The trilayer heavy metal 1 | ferromagnetic insulator | heavy metal 2 (HM1 | FMI | HM2) struc-

ture is built up of a ferromagnetic insulator with thickness d sandwiched between a heavy metal, which is a very poor spin sink (HM1) and thus does not allow any spin current across the HM1 | F interface, and a heavy metal 2, which is a perfect spin sink and thus allows the electrons to thermalize with the magnons inside the ferromagnet.
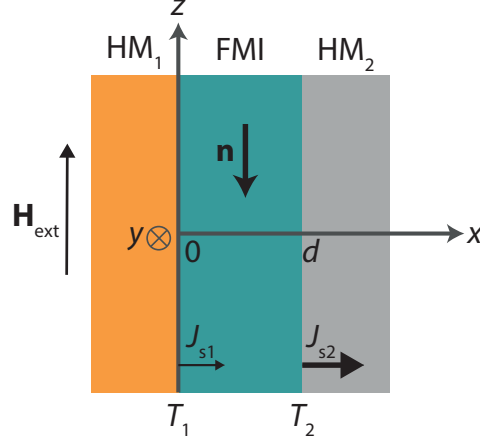
Figure 2.3.1.: Setup considered by Hoffman *et al.*. The trilayer structure consists of a ferromagnetic insulator (FMI) sandwiched between a heavy metal (HM1) which is a poor spin sink such that $J_{s1} = 0$ and a heavy metal (HM2) which is an ideal spin sink resulting in $J_s \approx J_{s,2}$. The force driving the spin current originates from a constant thermal gradient applied across the ferromagnetic insulator in **x**-direction. The external magnetic field $\mathbf{H}_{\text{ext}}$ is considered to be along the **z**-direction. Figure adapted from Ref. [20].

The temperature gradient $\nabla T = d_x T(x)\mathbf{x}$ driving the spin Seebeck effect is parametrized as

$$T(x) = T_1 + \frac{x}{d}(T_2 - T_1) \,, \tag{2.12}$$

assuming that the magnon-phonon scattering is the main contribution to the Gilber damping α.

The resulting boundary conditions for the setup shown in Fig. 2.3.1 at $T \to 0$ are

$$\mathbf{J}_{\text{s,x}} = 0 \quad (x = 0) \tag{2.13}$$

and

$$\mathbf{J}_{\text{s,x}} = \frac{\hbar g^{\uparrow\downarrow}}{4\pi}\mathbf{n} \times \frac{d\mathbf{n}}{dt} \quad (x = d) \,, \tag{2.14}$$

which is the spin pumping current across the FMI | HM2 interface under the assumption of HM2 being a perfect spin sink. Here, the real part of the spin-mixing conductance $g^{\uparrow\downarrow} = \text{Re}\, g_{\text{tot}}^{\uparrow\downarrow}$ describes the transparency of the FMI | HM2 interface with regard to DC spin currents.

At finite temperatures, the boundary condition at $x = d$ has to be modified by a stochastic term $\mathbf{h}'$, analogously to the LLG equation, yielding the modified boundary condition

$$A\partial_{\text{x}}\mathbf{n} + \frac{\hbar g^{\uparrow\downarrow}}{4\pi}\partial_{\text{t}}\mathbf{n} + \mathbf{h}' = 0 \quad (x = d) \,, \tag{2.15}$$

where $\mathbf{h}'$ describes the stochastic and thermal fluctuations at the interface.

The main outcome of a temperature gradient across the HM1 | FMI | HM2 trilayer structure is a spin current across the FMI | HM2 interface, which is described by equation (2.11). Under the assumption that the polarization of the spin current is parallel to the $\mathbf{z}$-axis in thermal average ($< \mathbf{J}_{s,x} > = J_s \mathbf{z}$), the spin current can be rewritten by introducing a complex notation $n = n_x - i n_y$:

$$J_s = A \operatorname{Im} < n^* \partial_x n > |_{x=d} . \tag{2.16}$$

Due to the translational invariance within the yz-plane, this can be expressed as

$$J_s = A \operatorname{Im} \int \frac{d^2\mathbf{q}\, d\omega}{(2\pi)^3} \frac{< n^*(\mathbf{q},\omega) \partial_x n(\mathbf{q}',\omega') >}{(2\pi)^3 \delta(\mathbf{q} - \mathbf{q}') \delta(\omega - \omega')} \tag{2.17}$$

where

$$n(\mathbf{q},\omega) = \int d^2\boldsymbol{\rho}\, dt\, e^{i(\omega t - \mathbf{q}\cdot\boldsymbol{\rho})} n(\boldsymbol{\rho}, d, t) \tag{2.18}$$

is the Fourier transform over the in-plane coordinate $\boldsymbol{\rho}$ on the FMI | HM2 interface and time t.

The same two-dimensional Fourier transformation is applied to the random field generators $\mathbf{h}$ and $\mathbf{h}'$ leading to the two dimensional Fourier transformed and linearized stochastic LLG equation

$$A(\partial_x^2 - \kappa^2) n(x, \mathbf{q}, \omega) = h(x, \mathbf{q}, \omega). \tag{2.19}$$

Here, κ is defined as

$$\kappa^2 = q^2 + \frac{H - (1 + i\alpha)\omega}{A_x/\gamma}. \tag{2.20}$$

The Fourier transformed boundary conditions are

$$A(\partial_x - \kappa') n(x, \mathbf{q}, \omega) = -h'(\mathbf{q}, \omega) \quad (x = d) \tag{2.21}$$

and

$$\partial_x n = 0 \quad (x = 0). \tag{2.22}$$

Here, κ' is defined as

$$\kappa' = i\frac{\alpha' \gamma \omega}{A_x}, \tag{2.23}$$

where

$$\alpha' = \frac{\hbar g^{\uparrow\downarrow}}{4\pi s} \tag{2.24}$$

has the dimensions of length. α'/d is the enhanced Gilbert damping due to spin pumping across the interface for a monodomain precession of the ferromagnetic layer. Equations (2.19) to (2.22) form a closed system of differential equations, which was solved for $n(\mathbf{q}, \omega)$ by Hoffman *et al.* [20].

With the definition of the spin Seebeck coefficient

$$S = \frac{J_s}{k_B(T_1 - T_2)} \tag{2.25}$$

and the substitution of the solution for $n(\mathbf{q}, \omega)$ into Eq. (2.17), the final form of the spin

Seebeck coefficient becomes

$$S = \frac{\alpha\alpha' s^2}{8\pi^3 A^2 d} \int_{-\infty}^{\infty} d^2\mathbf{q} \int_{-\infty}^{\infty} \frac{d\omega\omega(\mathbf{q}, d)}{|\kappa\sinh(\kappa d) - \kappa'\cosh(\kappa d)|^2} \times \left[\frac{\sin^2(\kappa_{\mathrm{i}} d)}{\kappa_{\mathrm{i}}^2} + \frac{\sinh^2(\kappa_{\mathrm{r}} d)}{\kappa_{\mathrm{r}}^2}\right] , \quad (2.26)$$

where κ_{r} and κ_{i} is the real and imaginary part of κ, respectively.

To account for the quantum mechanical statistics of magnons for $\hbar\omega \approx 1/\beta$, which are distributed according to Bose-Einstein statistics, an additonal factor

$$F(\beta\hbar\omega) = \left[\frac{\beta\hbar\omega/2}{\sinh(\beta\hbar\omega/2)}\right]^2 \quad (2.27)$$

has to be taken into account. This factor effectively cuts off the contribution from magnons with energy $\hbar\omega \gg k_{\mathrm{B}} T$. This finally yields

$$S = \frac{\alpha\alpha' s^2}{8\pi^3 A^2 d} \int_{-\infty}^{\infty} d^2\mathbf{q} \int_{-\infty}^{\infty} \frac{d\omega\omega(\mathbf{q}, d)F(\beta\hbar\omega)}{|\kappa\sinh(\kappa d) - \kappa'\cosh(\kappa d)|^2} \times \left[\frac{\sin^2(\kappa_{\mathrm{i}} d)}{\kappa_{\mathrm{i}}^2} + \frac{\sinh^2(\kappa_{\mathrm{r}} d)}{\kappa_{\mathrm{r}}^2}\right]. \quad (2.28)$$

2.3.2. Spin Seebeck effect in the bulk limit

For large thicknesses, the boundary condition at the HM1 | FMI interface becomes irrelevant, since only magnons within a distance smaller than the decay length for thermal magnons

$$l = \frac{1}{\alpha}\sqrt{\frac{\hbar A_{\mathrm{x}}}{\gamma k_{\mathrm{B}} T}} \quad (2.29)$$

from the interface contribute to the spin Seebeck effect. In rare-earth iron garnets l is $\leq$ $10\,\mu\mathrm{m}$. In the limit $d \gg l$, we can take $d \to \infty$ for the integrand in Eq. (2.28), which gives

$$S = \frac{\alpha\alpha' s^2}{8\pi^3 A^2 d} \int_{-\infty}^{\infty} d^2\mathbf{q} \int_{-\infty}^{\infty} \frac{d\omega\omega(\mathbf{q}, d)F(\beta\hbar\omega(\mathbf{q}, d))}{\kappa_{\mathrm{r}}^2|\kappa - \kappa'|^2}. \quad (2.30)$$

Within this limit, the integrand is independent of the thickness d, which yields $S \propto 1/d$, as expected. Here, the two-dimensional dispersion relation at the FMI | HM2 interface $\omega(\mathbf{q}, d)$ inside the integrand is related to the bulk magnon dispersion relation $\omega(\mathbf{q})$ [20].

In a ferrimagnetic showcase material system with two magnetic sublattices $\mathbf{M}_{\mathrm{red}}$ and $\mathbf{M}_{\mathrm{blue}}$, which are antiferromagnetically coupled with $|\mathbf{M}_{\mathrm{red}}| > |\mathbf{M}_{\mathrm{blue}}|$, the first, acoustic magnon band describes the precession of the two sublattices in phase yielding a quasi-ferromagnetic behavior with $\mathbf{M}_{\mathrm{tot}} = \mathbf{M}_{\mathrm{red}} + \mathbf{M}_{\mathrm{blue}}$ (see red band in Fig. 2.3.2). According to Eq. (2.9) this magnon band is described by

$$\mathbf{M}_{\mathrm{tot}} = \sum_{\mathrm{i}} \mathbf{M}_{\mathrm{i}} = -\gamma_{\mathrm{tot}} s_{\mathrm{tot}} \mathbf{n}_{\mathrm{tot}} \quad (2.31)$$

with $s_{\mathrm{tot}} > 0$.

The upper, optical band (see blue band in Fig. 2.3.2) is related to the precession of the weaker magnetic sublattice, with the sublattice magnetization $\mathbf{M}_{\mathrm{blue}} \uparrow\downarrow \mathbf{M}_{\mathrm{tot}}$, inside the exchange field of the stronger magnetic sublattice $\mathbf{M}_{\mathrm{red}} \uparrow\uparrow \mathbf{M}_{\mathrm{tot}}$ leading to an energy gap E_{gap} at the center of the Brillouin-zone. Thus, for a showcase dispersion relation with the

two bands, well separated in energy as shown in Fig. 2.3.2, the spin Seebeck coefficient S can be split up into the sum of two parts

$$S = S_{\text{red}} + S_{\text{blue}}, \tag{2.32}$$

where

$$S_{\text{i}} = \frac{\alpha \alpha' s_{\text{i}}^2}{8\pi^3 A^2 d} \int_{-\infty}^{\infty} d^2\mathbf{q} \int_{-\infty}^{\infty} \frac{d\omega_{\text{i}} \omega_{\text{i}}(\mathbf{q}, d) F(\beta \hbar \omega_{\text{i}}(\mathbf{q}, d))}{\kappa_{\text{r}}^2 |\kappa - \kappa'|^2} . \tag{2.33}$$

Due to the opposite chiralities of the magnon bands resulting from $\mathbf{M}_{\text{red}} \upharpoonleft\downharpoonright \mathbf{M}_{\text{blue}}$, the spin density s_{i} is positive for the red band and negative for the blue band, yielding $S_{\text{red}} \propto s_{\text{red}} > 0$ and $S_{\text{blue}} \propto s_{\text{blue}} < 0$. At finite temperatures, the contribution of the gapped, blue mode is exponentially suppressed for $1/\beta = k_{\text{B}}T < E_{\text{gap}}$ due to $F(\beta \hbar \omega(\mathbf{q}, d)) \propto e^{-\beta E_{\text{gap}}}$ in this temperature regime. Thus, for temperatures $T < E_{\text{gap}}/k_{\text{B}}$ the contribution from the red band dominates the total spin Seebeck coefficient $S \approx S_{\text{red}}$. With rising temperatures, the blue magnon mode gets populated, such that a gradual sign change at $T \gtrsim E_{\text{gap}}/k_{\text{B}}$ of the spin Seebeck coefficient is expected.
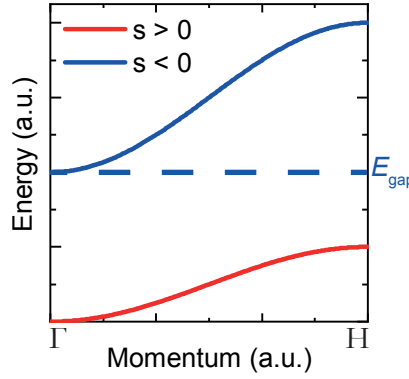
Figure 2.3.2.: Showcase dispersion relation for a ferrimagnetic material with two sublattices resulting in two magnon bands with opposite chirality and thus opposite spin densities s_{i} within the LLG theory of the spin Seebeck effect. The upper, blue band is gapped by the Energy E_{gap} at the Γ point and thus exponentially suppressed by a factor of $e^{-\beta E_{\text{gap}}}$ for $T < E_{\text{gap}}/k_{\text{B}}$. Similar magnon dispersion relations are present in compensated rare-earth iron garnets.

2.3.3. Experimental accessibility of the magnon-driven spin Seebeck effect

J. Barker and G.E.W. Bauer found that the spin-spin correlation function at the interface of a FMI | HM heterostructure is equivalent to the wave vector and frequency integral of the power spectrum of a bulk ferrimagnet in perturbation theory:

$$< \partial_{\text{x}} n_{\text{y}} \, n_{\text{x}} - \partial_{\text{x}} n_{\text{x}} \, n_{\text{y}} > = \iint d^3\mathbf{q} \, d\omega \, \omega (S^{xy}(\mathbf{q}, \omega) - S^{yx}(\mathbf{q}, \omega)) \tag{2.34}$$

with

$$S^{\alpha\beta} = < M^{\alpha*}(\mathbf{q}) M^{\beta}(\mathbf{q}) >_{T,\omega} , \tag{2.35}$$

where M^α is the α-component of the local magnetization [15]. Overall, this can be connected to Eq. (2.16), which yields

$$\frac{J_s}{A} = \text{Im} < n^* \partial_x n > |_{x=d} \propto \text{Im} \iint d^3\mathbf{q}\, d\omega\, n_{\text{BE}}(\omega, k_{\text{B}}T)\, \omega (S^{xy}(\mathbf{q}, \omega) - S^{yx}(\mathbf{q}, \omega)) \quad (2.36)$$

where $n_{\text{BE}}(\omega, k_{\text{B}}T)$ is the Bose-Einstein distribution for the thermal energy $k_{\text{B}}T$ and $(S^{xy}(\mathbf{q}, \omega) - S^{yx}(\mathbf{q}, \omega))$ is the power spectrum of the transverse spectral function and J_s the spin current across the FMI | HM interface. Here, $n_{\text{BE}}(\omega, k_{\text{B}}T)$ is again included to account for the bosonic statistics of spin wave excitations. The bulk quantity $\text{Im}(S^{xy}(\mathbf{q}, \omega) - S^{yx}(\mathbf{q}, \omega)) = -\text{i} \cdot (S^{xy}(\mathbf{q}, \omega) - S^{yx}(\mathbf{q}, \omega))$ is directly accessible via inelastic neutron scattering with polarization analysis and can furthermore be extracted from simulations of spin wave dispersion relations with SpinW, which both will be conducted within this work. Overall, Eq. (2.36) states that the sign and the size of the spin current across the interface are depending on the sign and the size of the power spectrum of the bulk spin wave dispersion relation $-\text{i} \cdot (S^{xy}(\mathbf{q}, \omega) - S^{yx}(\mathbf{q}, \omega))$ as well as on the thermal energy $k_{\text{B}}T$ which defines the statistics of the spin wave excitations within the Bose-Einstein distribution $n_{\text{BE}}(\omega, k_{\text{B}}T)$.

2.3.4. Sample geometry and measurement setup for spin Seebeck effect experiments

This work will focus on the longitudinal spin Seebeck effect in FMI | HM samples, as shown in Fig. 2.3.3 (a). For the application of the thermal gradient, the heavy metal layer is heated by the application of a heating current orthogonal to the voltage detection direction. The spin current across the FMI | HM interface, caused by the spin Seebeck effect, is partially converted into a charge current J_c^{ISHE} by the inverse spin Hall effect, which can be detected as a voltage drop in an open boundary condition.

There are two options to measure the amplitude V_{SSE} of the spin Seebeck effect. The first one is field-dependent measurements of the voltage drop across the interface (FD-SSE). Within these experiments, the orientation of the externally applied magnetic field $\mu_0\mathbf{H}_{\text{ext}}$ is constant at $\alpha = 0°$ and the magnitude of the field is varied from $+\mu_0 H_{\text{ext,max}}$ to $-\mu_0 H_{\text{ext,max}}$ to $+\mu_0 H_{\text{ext,max}}$ so that the full magnetic hysteresis of the ferrimagnetic insulator is covered. Since the magnon polarization is proportional to the magnetization of the ferrimagnetic insulator, the expectation is that the voltage drop V measured in the HM layer mimics the the magnetic hysteresis $M_{\text{tot}}(\mu_0 H_{\text{ext}})$ (see Fig. 2.3.3 (b)). Here, the field dependent amplitude $V_{\text{SSE}}(\mu_0 H_{\text{ext}})$ of the spin Seebeck effect is defined as

$$V_{\text{SSE}}(\mu_0 H_{\text{ext}}) = \frac{V(+\mu_0 H_{\text{ext}}) - V(-\mu_0 H_{\text{ext}})}{2}. \quad (2.37)$$

The second type of experiment is the angle-dependent measurement of the spin Seebeck effect (AD-SSE). For this experiment, the external magnetic field $\mu_0\mathbf{H}_{\text{ext}}$ is rotated inside the interface plane with a fixed magnitude. Here, the angle α describes the orientation of the external magnetic field $\mu_0\mathbf{H}_{\text{ext}}$ with respect to the applied current direction ($\alpha = 0°$ for the magnetic field parallel to the current direction, see Fig. 2.3.3 (a)). When the external magnetic field is rotated with its magnitude larger than the saturation field, the sublattice

magnetizations of the ferrimagnetic insulator follow the magnetic field and thus also the magnon polarizations. This results in an overall rotation of the inverse spin Hall effect charge current $\mathbf{J}_c^{\text{ISHE}}$ direction parallel to the FMI | HM interface. Due to our fixed detection scheme, we can only probe the projection of $\mathbf{J}_c^{\text{ISHE}}$ along the **x**-axis leading to a $\cos(\alpha)$-dependent voltage signal

$$V(\alpha) = V_{\text{SSE}} \cdot \cos(\alpha) \tag{2.38}$$

with the amplitude of the spin Seebeck effect V_{SSE} as the oscillation amplitude (see Fig. 2.3.3 (c)).

Overall, the AD-SSE experiment offers a more precise measurement of the spin Seebeck effect amplitude V_{SSE} due to larger statistics by fitting a cosine-function to the experimental data, but is only applicable to magnetically softer materials and does not cover effects depending on the field magnitude. On the other hand, the FD-SSE experiment allows to align the magnetization parallel to the magnetic easy axis allowing experiments with magnetically anisotropic FMIs and gives insight into effects depending on the field magnitude.
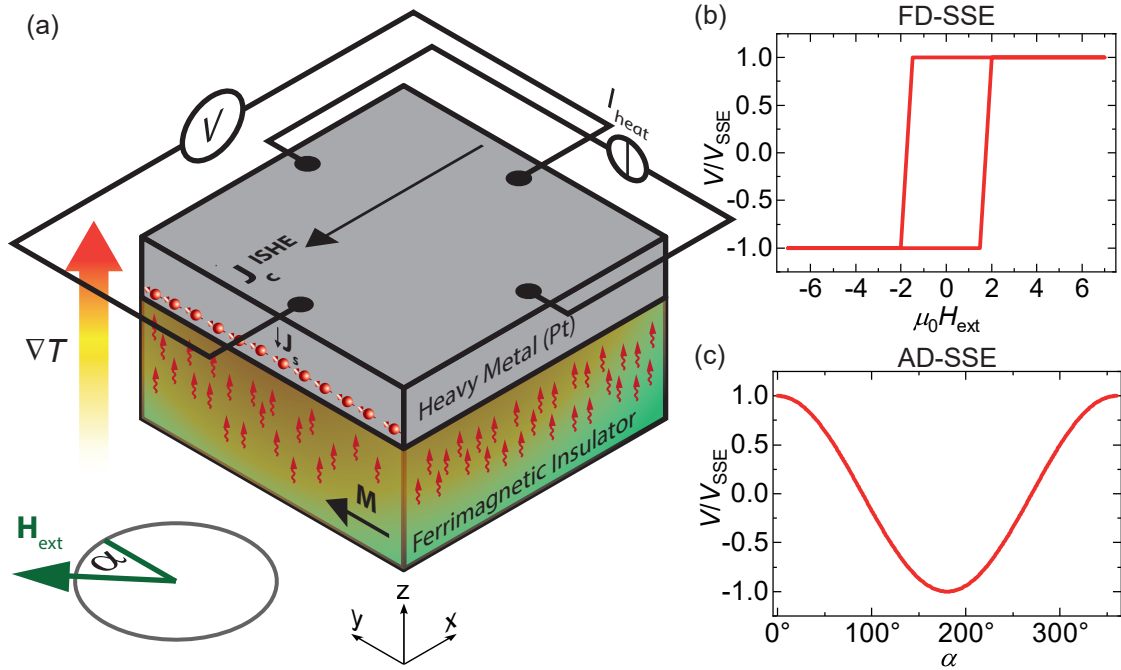
Figure 2.3.3.: (a) Measurement setup for longitudinal spin Seebeck effect (SSE) experiments carried out within this work. The temperature gradient across the ferrimagnetic insulator (FMI) is generated by resistive heating of the heavy metal layer (Pt) applying the current I_{heat}. The spin current across the interface is partially converted into a charge current by the inverse spin Hall effect resulting in a voltage drop $V \propto \mathbf{J}_S$ in an open boundary condition. (b) Qualitative normalized voltage drop within the Pt-layer expected for field dependent SSE experiments (FD-SSE) with $\alpha = 0°$. (c) Qualitative normalized voltage drop within the Pt layer expected for angle-dependent SSE experiments (AD-SSE) with fixed external magnetic field magnitude H_{ext}

2.4. Rare-earth iron garnets

This section outlines the main physical properties of rare-earth iron garnets (REIG), which are used as ferrimagnetic insulators for spin Seebeck effect experiments within this work. The first identified REIG was $Y_3Fe_5O_{12}$, which was described by Bertaut *et al.* in 1956 [21]. REIGs are famous for their low Gilbert damping and large magnon propagation lengths, making them an ideal material system for magnon transport experiments.

Rare earth iron garnets are commonly described within a body centered cubic (bcc) unit cell with the space group Ia3d [22]. REIGs have the chemical formula $RE_3Fe_5O_{12}$ with 4 formula units per lattice point, resulting in a total of 160 atoms per bcc unit cell (see Fig. 2.4.1). As rare earth (RE) all of the $4f$-Lanthanoides as well as Yttrium can be substituted, which allows to tune the materials properties over a wide range.
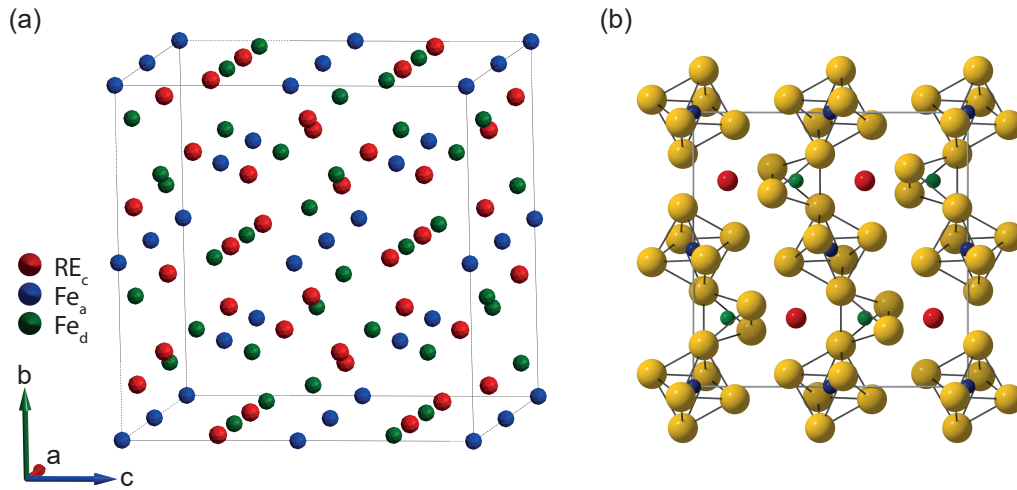
Figure 2.4.1.: (a) Body centered cubic (bcc) unit cell of REIGs with the space group Ia3d. For clarity, the O^{2-} ions are neglected. Within the Ia3d space group, the Fe^{3+} ions are located on the $24d$- (green spheres) and $16a$-sites (blue spheres) leading to two magnetic sublattices, which are strongly antiferromagnetically coupled resulting in a Néel temperature $T_N \approx 550\,K$ almost independent of the RE-ion on the $24c$-site (red spheres). (b) Center layer of the bcc unit cell including the O^{2-} ions (yellow spheres). The Fe_a and Fe_d sites are octahedrally and tetrahedrally coordinated with the O^{2-} ions, respectively.

Within the Ia3d space group the RE^{3+} ions are located on the $24c$ sites and the Fe^{3+} ions on the $24d$ and $16a$ sites [23]. The ratio of $16a : 24d$ Fe^{3+} sites is $2 : 3$. Thus, the chemical formula is often written as $Re_3Fe_2Fe_3O_{12}$. The two Fe^{3+} sites form strongly coupled magnetic sublattices with antiparallel aligned sublattice magnetizations $\mathbf{M}_{Fea} \upharpoonleft\!\downharpoonright \mathbf{M}_{Fed}$ resulting in a ferrimagnetic order with a Néel temperature of $T_N \approx 550\,K$. Due to the overall strong magnetic Fe-Fe coupling, the Néel temperature is nearly independent of the RE-ion (see Fig. 2.4.2). The magnetic exchange mechanism is the indirect antiferromagnetic superexchange mediated by the O^{2-} ions on the $96h$ sites, leading to an antiferromagnetic inter- and intra-sublattice coupling with different magnitudes resulting in an antiparallel magnetic structure of the two Fe^{3+} sublattices.
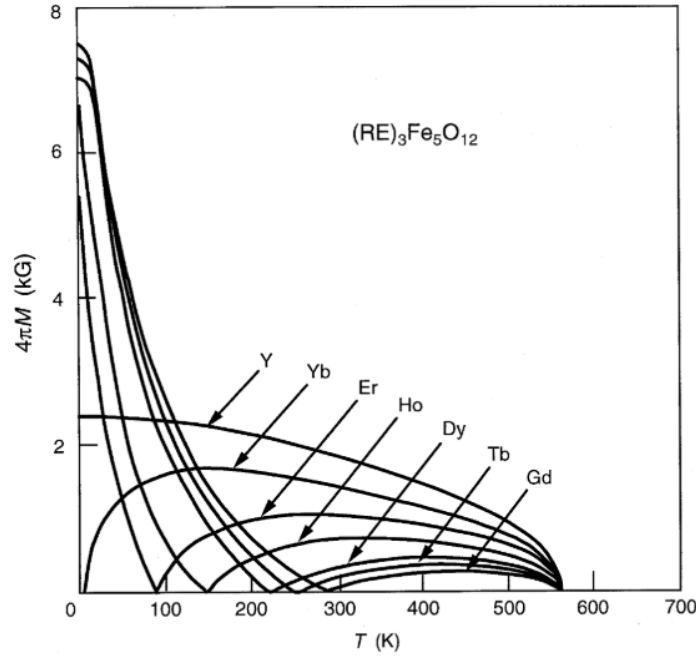
Figure 2.4.2.: Magnetization versus temperature of rare-earth iron garnets (REIGs) for several REs from Bertaut and Pauthenet [21, 24]. For all REIGs, the Néel temperature $T_N \approx 550\,\text{K}$ is similar demonstrating that the strongly antiferromagnetically coupled Fe-sublattices determine T_N. The magnetic compensation temperature T_{comp}, where the total remanent magnetization M_{tot} vanishes, exists for all REIGs with RE^{3+}-ions possessing a finite magnetic moment and is strongly depending on the RE^{3+}-ion. Figure taken from Ref. [25].

2.4.1. Yttrium-Iron-Garnet

Yttrium-Iron-Garnet (YIG) with the chemical formula $Y_3Fe_5O_{12}$ is the most prominent REIG due to its smallest known Gilbert damping $\alpha = 4 \cdot 10^{-5}$ [26] and thus very high magnon propagation and coherence lengths. Even for YIG thin films grown by pulsed laser deposition, the Gilbert-damping is smaller than $\alpha \lessapprox 1 \cdot 10^{-3}$ [27].

Due to the non-magnetic RE-ion Y^{3+}, YIG is a ferrimagnet with two antiferromagnetically coupled Fe^{3+}-sublattices and thus the magnetically simplest REIG. Due to the very strong inter-sublattice coupling $J_{\text{ad}} = 6.8\text{meV}$ [28], YIG has a quasi ferromagnetic behavior. This attribute is also found in the spin wave dispersion relation (see Fig. 2.4.3), where the red, parabolic band up to $f \approx 7.5\,\text{THz}$ ($E \approx 31\text{meV}$) mimics a ferromagnetic dispersion relation. This band describes the spin wave excitation, where the local magnetic moments from the two magnetic sublattices precess in phase. The color code describes the spin current chirality from red ($\chi = +1$) to blue ($\chi = -1$).
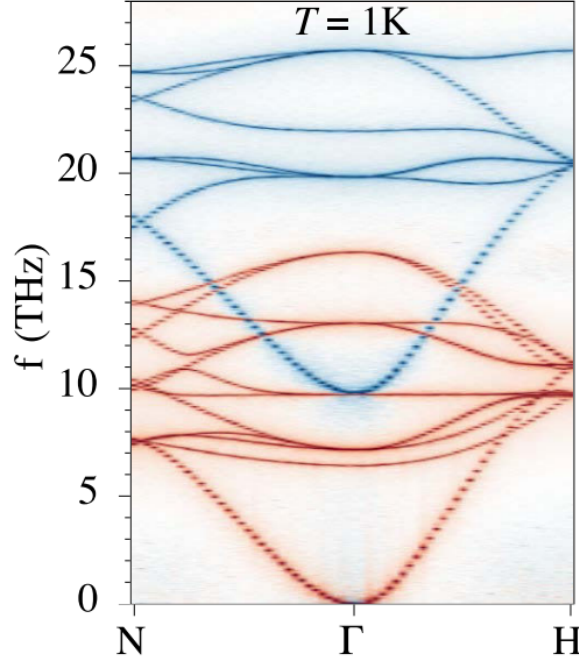
Figure 2.4.3.: Spin wave dispersion relation for $Y_3Fe_5O_{12}$ at $T = 1\,K$ calculated by J. Barker and G.E.W. Bauer. The key feature is the red, parabolic band up to $f = 7.5\,THz \approx 31\,meV/h$ allowing a quasi ferromagnetic description up to room temperature. Figure taken from Ref. [15].

2.4.2. Gadolinium-Iron-Garnet

With Gadolinium-Iron-Garnet (GdIG), a third magnetic sublattice $\mathbf{M}_{Gdc}$ within the Ia3d is introduced due to the Gd^{3+}-ions on the $24c$ site exhibiting a spin moment of $S = 7/2$. The magnetic sublattice consisting of the Gd^{3+}-ions is only weakly coupled to the two magnetic Fe^{3+}-sublattices with a ratio of exchange constants $J_{dc}/J_{ad} = 0.29$ and $J_{ac}/J_{ad} = 0.07$ [16]. Its remanent sublattice magnetization $\mathbf{M}_{Gdc}$ is oriented antiparallel to the total magnetization of the Fe^{3+}-sublattices ($\mathbf{M}_{Gdc} \uparrow\downarrow \mathbf{M}_{Fe} = \mathbf{M}_{Fea} + \mathbf{M}_{Fed}$). The weak coupling of $\mathbf{M}_{Gdc}$ to the two magnetic Fe^{3+}-sublattices is leading to a strong temperature dependence of $\mathbf{M}_{Gdc}$ resulting in a magnetic compensation temperature T_{comp}, where the remanent sublattice magnetizations sum up to $M_{tot}(T_{comp}) = 0$. When crossing T_{comp} in finite magnetic fields, the sublattice magnetizations invert their orientations to ensure that the total magnetization $\mathbf{M}_{tot}$ is aligned along the external magnetic field $\mathbf{H}_{ext}$. In a small temperature region around the magnetic compensation temperature T_{comp}, the sublattice magnetizations are not aligned collinear to each other and form the so-called canting phase in finite external magnetic fields [29].

The presence of a third magnetic sublattice with sublattice magnetization $\mathbf{M}_{Gdc}$ causes fundamental changes in the spin wave dispersion relation. Figure 2.4.4 shows the calculated spin wave dispersion relation of GdIG. The first, gapless mode describes the ferrimagnetic resonance mode, where at the Γ-point the sublattice magnetizations of the three magnetic sublattices ($\mathbf{M}_{Fea}, \mathbf{M}_{Fed}, \mathbf{M}_{Gdc}$) precess in phase. This mode has a parabolic dispersion around the Γ point, which is typical for ferrimagnetic materials. The upper boundary of the ferrimagnetic resonance mode is defined by the energy level of the approximately dispersionless, red flat bands which describe the precession of the Gd^{3+}-moments in the local

exchange field of the Fe^{3+}-moments. The flatness can be explained by the negligible intra-sublattice coupling constant J_{cc} of Gd^{3+}-moments.

Above the flat bands, the spin wave dispersion relation exhibits a strongly dispersing, first optical mode with opposite chirality ($\chi = -1$, blue) which is attributed to the precession of the Fe^{3+} moments in the exchange field originating from the Gd^{3+}-moments. Thus, the energy gap E_{gap} of this first optical mode is proportional to the size of the exchange field acting on the total Fe-sublattice magnetization ($\mathbf{M}_{Fe} = \mathbf{M}_{Fea} + \mathbf{M}_{Fed}$). Due to the antiparrallel orientation of the Gd-sublattice magnetization to the total Fe-magnetization ($\mathbf{M}_{Gd} \uparrow\downarrow \mathbf{M}_{Fe}$) and the antiparallel configuration of the Fe-sublattice magnetizations ($\mathbf{M}_{Fed} \uparrow\uparrow \mathbf{M}_{Fe}$ and $\mathbf{M}_{Fea} \uparrow\downarrow \mathbf{M}_{Fe}$), this yields the following proportionality of the energy gap:

$$E_{gap} \propto |\mathbf{M}_{Gd}|(J_{dc}|\mathbf{M}_{Fed}| - J_{ac}|\mathbf{M}_{Fea}|) , \tag{2.39}$$

where $(J_{dc}|\mathbf{M}_{Fed}| - J_{ac}|\mathbf{M}_{Fea}|) > 0$. Thus, E_{gap} is strongly temperature dependent due to the strong temperature dependence of $\mathbf{M}_{Gd}$, which is leading to a gradual sign change in the temperature profile of the amplitude of the spin Seebeck effect in GdIG | Pt bilayer structures [16].
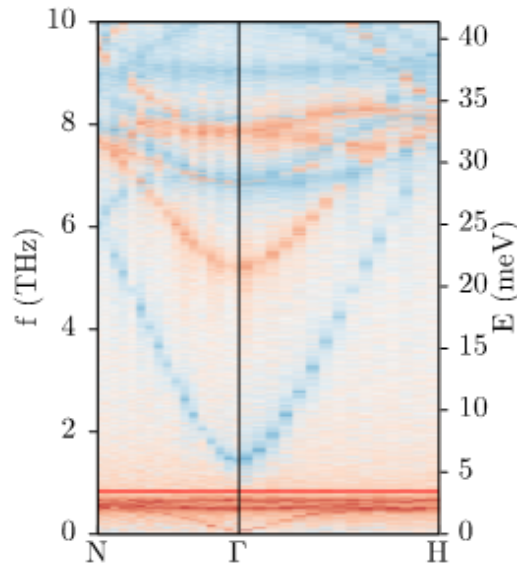
Figure 2.4.4.: Calculated spin wave dispersion relation for $Gd_3Fe_5O_{12}$ at $T = 40\,K$. The color code depicts the chirality of the magnon modes. The interplay between the gapless, red band which describes the ferrimagnetic resonance mode and the first optical, blue mode with opposite chirality causes a gradual sign change in $V_{SSE}(T)$ measured in $Gd_3Fe_5O_{12}$ | Pt bilayer structures. Figure taken from Ref. [16].

2.4.3. Terbium-Iron-Garnet

The reason for introducing TbIG as a showcase material system is the extraordinary large cross section for capture of thermal neutrons of Gd [17]. Since the motivation of this work is the relation of the spin wave dispersion relation measured by inelastic neutron scattering to the spin Seebeck effect, GdIG cannot be used as a showcase material system. Thus, TbIG is chosen as material system due to its smaller cross section for capture of thermal neutrons, non-trivial spin wave dispersion relation and low Gilbert-damping. In total, this

makes TbIG a good showcase material system for studying the origin of the spin Seebeck effect.

The material system Terbium-Iron-Garnet $Tb_3Fe_5O_{12}$(TbIG) is the next step in complexity in terms of REIGs by substitution of the Gd^{3+}-ions by Tb^{3+}-ions with the ground state $^7F_6$ on the $24c$ site. The finite orbital momentum as well as the highly anisotropic properties in terms of crystal field and exchange interactions of the Tb^{3+}-moments lead to a very strong cubic anisotropy parallel to the cubic $[111]_{bcc}$-directions [30]. Similar to GdIG, TbIG has a magnetic compensation temperature $T_{comp} = 250.5\,K$, where the total remanent magnetization vanishes.

TbIG, in contrast to YIG and GdIG, is subject to a rhombohedral distortion for $T < T_{rh} \approx 190\,K$ (see Fig. 2.4.5) [23, 31].
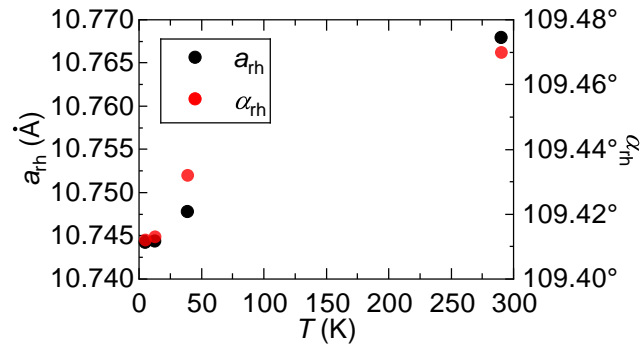
Figure 2.4.5.: Rhombohedral lattice constant a_{rh} and rhombohedral angle α_{rh} of the primitive unit cell for TbIG as a function of temperature. At $T = 280\,K$, the primitive, rhombohedral unit cell (spacegroup $R\bar{3}$) and the conventional, cubic unit cell (spacegroup Ia3d) are equivalent. Data taken from Ref. [23].

The second key feature of TbIG is the so called 'double umbrella' structure found by Lahoubi *et al.* [32]. It describes the gradual formation of a non-collinear magnetic structure below $T_{du} \approx 160\,K$, where the magnetic moments of the Tb^{3+}-ions tilt away from the cubic $[111]_{bcc}$-direction. Due to the rhombohedral distortion, the degeneration of the $24c$ sites in the cubic Ia3d space group is lifted to non-degenerate $6e$ and $6e'$ sites with equal occupation numbers within the rhombohedral $R\bar{3}$ space group. For each Tb^{3+}-site ($6e$ and $6e'$), there are three degenerate orientations for the magnetic moments within the $[111]_{bcc} \times [100]_{bcc}$ and equivalent planes in the cubic description, which can be fully described by the opening angle θ and θ' with $\theta > \theta'$ (see Fig. 2.4.6 (a)). The 'double umbrella' structure with finite angles θ and θ' starts gradually below $T_{du} \approx 160\,K$ and reaches the maximum opening angle in the $0\,K$ limit. Experimentally, the maximum values of the opening angles are found to be $\theta = 32°$ and $\theta' = 27°$ at $5\,K$. (see Fig. 2.4.6 (b)) [33].

The influence of the double umbrella structure on the magnon dipersion relation is yet unknown and will be discussed in chapter 4.
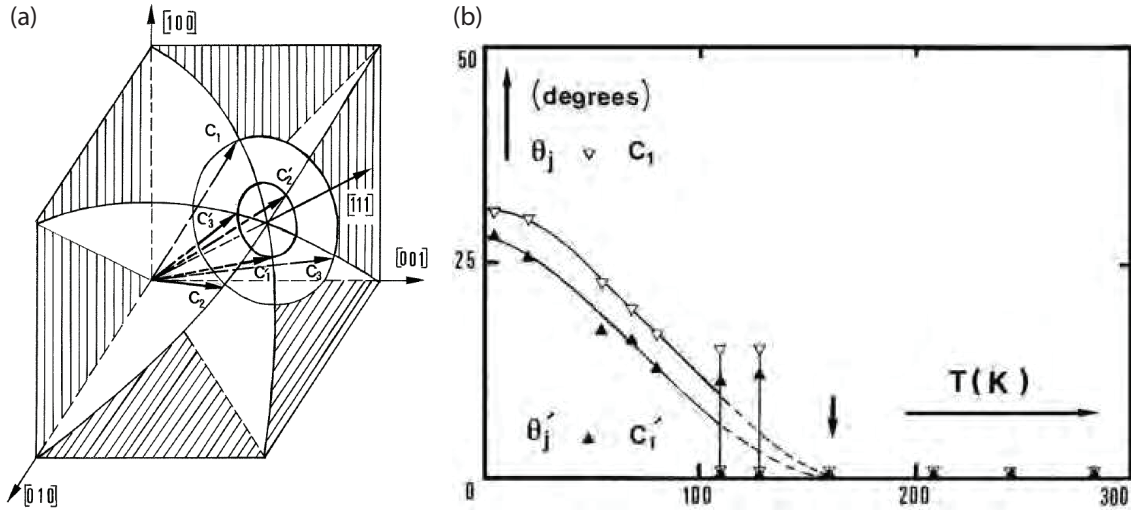
Figure 2.4.6.: (a) Illustration of the magnetic double umbrella structure within the cubic description of TbIG. The Tb^{3+}-moments tilt away from the cubic $[111]_{bcc}$-direction within three equivalent glide planes and thus can be fully described by the opening angles θ and θ'. (b) Opening angles θ and θ' of the double umbrella structure as a function of temperature. The opening angles become finite below $T_{du} \approx 160$ K reaching their maximum slope around 80 K and saturate at 5 K with $\theta = 32°$ and $\theta' = 27°$. Figures taken from Ref. [33]

Furthermore, Kang *et al.* found a coupling between magnons at the Γ-point and ligand field excitations by performing far-infrared spectroscopy on TbIG single crystals at different temperatures (see Fig. 2.4.7) [34]. The authors identified the magnetic excitation and the ligand field excitation due to their strong and weak temperature dependence, respectively. The avoided-crossing visible in Fig. 2.4.7 indicates a coupling between the magnon and the ligand-field excitation leading to the hybrid modes $\Omega^{(1)}_{LF-M}$ and $\Omega^{(2)}_{LF-M}$.
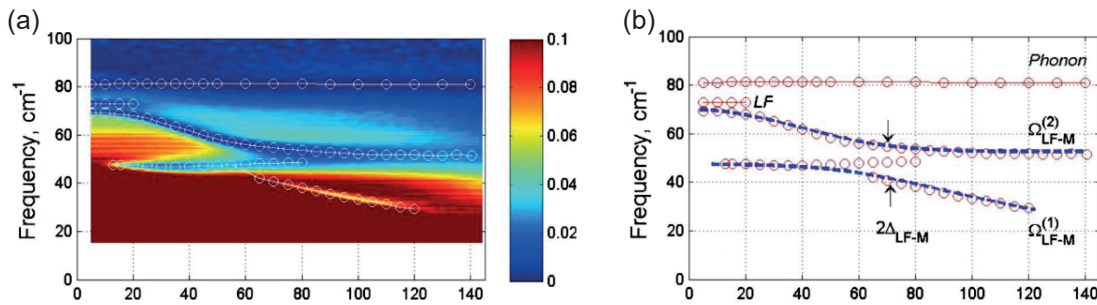
Figure 2.4.7.: Far-infrared spectroscopy of TbIG as a function of temperature. (a) Color map of the normalized transmitted light intensity as a function of temperature and frequency for a TbIG single crystal. (b) Extracted experimental data for hybridized excitations $\Omega^{(1)}_{LF-M}$ and $\Omega^{(2)}_{LF-M}$ originating from a coupling of the ligand-field excitations and magnons at the Γ-point. The frequency gap Δ_{LF-M} determines the strength of the interaction between magnons and ligand field excitations. Figures taken from Ref. [34].

3. Inelastic neutron scattering on a Tb$_3$Fe$_5$O$_{12}$ single crystal

This chapter describes the results of inelastic neutron scattering with polarization analysis on a Tb$_3$Fe$_5$O$_{12}$ single crystal at $280\,\mathrm{K}$, $100\,\mathrm{K}$ and $10\,\mathrm{K}$. In the first part, the theory of neutron scattering on magnetic structures is summarized and connected to the spin Seebeck effect. Subsequently, the experimental setup for inelastic neutron scattering with polarization analysis is explained together with the experimental procedure and the performed data analysis. The main part of this chapter then focuses on the presentation and interpretation of the experimental results.

3.1. Inelastic neutron scattering with polarization analysis - A powerful investigation technique for magnetic properties

Inelastic neutron scattering is a powerful technique for the investigation of magnetic properties, since it directly measures the Fourier transform of the time dependent magnetic pair correlations. In the following, a brief introduction into the fundamentals of neutron scattering according to the lecture of M. Enderle is given [35].

The experiments within this work are conducted with thermal neutrons, which show weak interaction with matter in general. The reason is either the weakness of the interaction itself (e.g. dipole-dipole scattering on magnetic moments of the electrons) or the short range character of the interaction (e.g. strong interaction with the nucleus). Thus, the neutron probes the whole sample volume and multiple scattering can be neglected. In mathematical words, the Born approximation is valid and the scattering on the scattering potential V is treated as first order perturbation such that Fermi's golden rule for the differential cross section applies. This is resulting in the following main equation for the differential cross section:

$$\frac{d^2\sigma}{d\Omega dE_\mathrm{f}} = \frac{k_\mathrm{f}}{k_\mathrm{i}} \left(\frac{m}{2\pi\hbar^2}\right)^2 \sum_{\mathbf{s}_\mathrm{i}, \mathbf{s}_\mathrm{f}, n_0, n_1} p(\mathbf{s}_\mathrm{i}) p(n_0) | < \mathbf{k}_\mathrm{f} \mathbf{s}_\mathrm{f} n_1 | V | \mathbf{k}_\mathrm{i} \mathbf{s}_\mathrm{i} n_0 > |^2 \, \delta(\epsilon_1 - \epsilon_0 - \hbar\omega) \, . \quad (3.1)$$

Here, $\hbar\omega = E_\mathrm{i} - E_\mathrm{f}$ is the energy transfer of the scattered neutron with initial energy E_i and final energy E_f, $\mathbf{k}_\mathrm{i}$ and $\mathbf{k}_\mathrm{f}$ are the wave vectors of the incident and the final, scattered state of the neutron with spin $\mathbf{s}_\mathrm{i}$ and $\mathbf{s}_\mathrm{f}$, respectively. The sample properties are described by the states n_0 and n_1 with energies ϵ_0 and ϵ_1. The description of the neutron as a plane wave $\propto e^{\mathrm{i}\mathbf{k}\cdot\mathbf{r}} = |\mathbf{k}>$ is valid due to the generation and detection of the neutron far away from the sample. This is leading to a Fourier-transformation of the scattering potential at $\mathbf{q} = \mathbf{k}_\mathrm{f} - \mathbf{k}_\mathrm{i}$. The Fourier transformation is allowed, if $\mathbf{q} \cdot \mathbf{r}$ commutes with the scattering

potential V, which is true for magnetic dipole-dipole scattering. A schematic drawing of a neutron scattering mechanism is shown in Fig. 3.1.1.
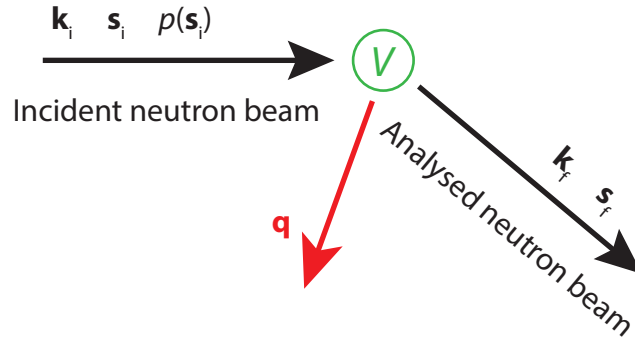
Figure 3.1.1.: Schematic drawing of inelastic neutron scattering. The incident neutron beam with wave vector $\mathbf{k}_i$, spin $\mathbf{s}_i$ and polarization $p(\mathbf{s}_i)$ is scattered on a scattering potential V. The final state of the neutron beam is described by the wave vector $\mathbf{k}_f$ and spin $\mathbf{s}_f$. In total a coherent scattering mechanism (e.g. neutron-magnon scattering) is fully described by $E(\mathbf{q}) = \frac{\hbar^2}{2m_{\text{neutron}}} \cdot (\mathbf{k}_i^2 - \mathbf{k}_f^2)$ with $\mathbf{q} = \mathbf{k}_f - \mathbf{k}_i$.

The scattering potential V_M considered here is the magnetic interaction potential of the neutron magnetic moment μ_n with the magnetic field from the electrons $\mathbf{B}_e$:

$$V_M = -\mu_n \cdot \mathbf{B}_e(\mathbf{r}) . \tag{3.2}$$

Here, $\mathbf{B}_e(\mathbf{r})$ is the local magnetic field emitted by the magnetic moments of the electronic crystal structure. This leads to the following matrix-element describing the scattering process, where the plane wave states of the incident and final neutron state are contracted $e^{i\mathbf{k}_f \cdot \mathbf{r}} \cdot e^{-i\mathbf{k}_i \cdot \mathbf{r}} = e^{i\mathbf{q} \cdot \mathbf{r}}$. By subsequent integration over space the matrix-element is then Fourier transformed:

$$< \mathbf{k}_f \mathbf{s}_f n_1 | - \mu_n \cdot \mathbf{B}_e(\mathbf{r}) | \mathbf{k}_i \mathbf{s}_i n_0 > = < \mathbf{s}_f n_1 | - \mu_n \cdot \mathbf{B}_e(\mathbf{q}) | \mathbf{s}_i n_0 > . \tag{3.3}$$

The Fourier transformation is allowed due to the vanishing commutator $[V_M, \mathbf{q} \cdot \mathbf{r}] = 0$, with $\mathbf{q} = \mathbf{k}_f - \mathbf{k}_i$. Additionally, the Fourier transformation of the Maxwell equation that states a divergence free magnetic field yields

$$\nabla \cdot \mathbf{B}_e(\mathbf{r}) = 0 \Leftrightarrow \mathbf{q} \cdot \mathbf{B}_e(\mathbf{q}) = 0. \tag{3.4}$$

Physically, this means that the neutron is only interacting with the magnetic field perpendicular to the momentum transfer $\mathbf{q}$ due to the divergence-free character of the magnetic field. For the magnetic moment of a single electron $\mu_e^{tot} = \mu_e^S + \mu_e^L$ at $\mathbf{r} = 0$, the interaction potential can be written as

$$V_M(\mathbf{r}) = -\mu_n \cdot \nabla \times (\nabla \times \frac{\mu_e^S}{r} + \nabla \times \frac{\mu_e^L}{r}) = -\mu_n \cdot \nabla \times \nabla \times \frac{\mu_e^{tot}}{r} \tag{3.5}$$

due to $\mathbf{B} = \nabla \times \mathbf{A}$ and $\mathbf{A} = \nabla \times \frac{\mu}{r}$. By Fourier transforming the interaction potential with the contraction of the plane wave states, $\nabla \times$ is transformed to $-i\mathbf{q} \times$, which is a non-trivial

step leading to the matrix-element

$$< s_f n_1 | \mu_n \cdot \left(\hat{q} \times (\hat{q} \times \mu_e^{tot}) \right) | s_i n_0 > \; = \; < s_f n_1 | -\mu_n \cdot \mu_{e\perp}^{tot}(q) | s_i n_0 > \quad (3.6)$$

$$\propto \; < s_f n_1 | -s \cdot \mu_{e\perp}^{tot}(q) | s_i n_0 > \, . \quad (3.7)$$

For an ensemble of magnetic moments, e.g. a magnetically ordered system $\mu_{e\perp}^{tot}$ is essentially substituted by

$$\mathbf{M}_\perp(\mathbf{q}) = \sum \mu_{e\perp}^{tot}(\mathbf{q}) \, . \quad (3.8)$$

This is leading to the cross section for inelastic neutron scattering on magnetically ordered system

$$\frac{d^2\sigma}{d\Omega dE_f} = \frac{k_f}{k_i} \left(\gamma r_0^2 \right)^2 \sum_{s_i,s_f,n_0,n_1} p(s_i)p(n_0) | < s_f n_1 | s \cdot \mathbf{M}_\perp(\mathbf{q}) | s_i n_0 > |^2 \, \delta(\epsilon_1 - \epsilon_0 - \hbar\omega) \quad (3.9)$$

with

$$\mathbf{M}_\perp(\mathbf{q}) = \hat{q} \times (\mathbf{M}(\mathbf{q}) \times \hat{q}) \quad (3.10)$$

and

$$\mathbf{M}(\mathbf{q}) = \int d^3r \, e^{i\mathbf{q}\cdot\mathbf{r}} \mathbf{M}(\mathbf{r}) \, , \quad (3.11)$$

where $\mathbf{M}(\mathbf{q})$ is the Fourier transformation of the magnetization within the sample.
The following step is conducted for an incoming unpolarized neutron beam and no polarization analysis of the scattered beam such that the sum over the neutron polarizations is straightforward. Furthermore, the δ-function is rewritten in its integral form:

$$\frac{d^2\sigma}{d\Omega dE_f} = \frac{k_f}{k_i} \left(\gamma r_0 \right)^2 \sum_{\substack{s_i \, s_f \\ n_0 n_1}} p(s_i)p(n_0) | < s_f n_1 | s \cdot \mathbf{M}_\perp(\mathbf{q}) | s_i n_0 > |^2 \, \delta(\epsilon_1 - \epsilon_0 - \hbar\omega) \quad (3.12)$$

$$= \frac{k_f}{k_i} \left(\gamma r_0 \right)^2 \sum_{n_0} p(n_0) \frac{1}{2\pi\hbar} \int dt \, e^{-i\omega t} < n_0 | \mathbf{M}_\perp^*(\mathbf{q},0) \cdot \mathbf{M}_\perp(\mathbf{q},t) | n_0 > \quad (3.13)$$

$$= \frac{k_f}{k_i} \left(\gamma r_0 \right)^2 < \mathbf{M}_\perp^*(\mathbf{q}) \cdot \mathbf{M}_\perp(\mathbf{q}) >_{T,\omega} \quad (3.14)$$

$$= \frac{k_f}{k_i} \left(\gamma r_0 \right)^2 \sum_{\alpha\beta} (\delta_{\alpha\beta} - \hat{q}^\alpha \hat{q}^\beta) < M^{\alpha*}(\mathbf{q}) M^\beta(\mathbf{q}) >_{T,\omega} \quad (3.15)$$

$$= \frac{k_f}{k_i} \left(\gamma r_0 \right)^2 \left(S^{xx}(\mathbf{q},\omega) + S^{yy}(\mathbf{q},\omega) \right) \quad (3.16)$$

with

$$S^{\alpha\beta} = < M^{\alpha*}(\mathbf{q}) M^\beta(\mathbf{q}) >_{T,\omega} \, . \quad (3.17)$$

In the last step, the coordinate system used within this work is considered, which is defined by $\mathbf{B} \uparrow\uparrow \mathbf{q} \uparrow\uparrow \hat{z}$. The main result is the connection of the differential scattering cross section

with the Fourier transformation of the magnetic pair-correlation function in Eq. (3.16). This proves that neutron scattering can directly access the Fourier transformation of the magnetic pair-correlation function, which makes neutron scattering a unique technique for the investigation of magnetic properties.

For inelastic neutron scattering with polarization analysis, the calculation of the cross section is more complicated. Up to Eq. (3.11), the calculation is performed for a general type of neutron scattering mechanism. Since in the case of inelastic neutron scattering with polarization analysis the sum over the neutron polarization is not straightforward, the result of the cross section for inelastic neutron scattering with polarization analysis will be presented without further derivation. A more detailed derivation is given in the lecture from M. Enderle [35].

In the following, the neutron polarization of the incident and final, scattered neutron beam is described relative to $\mathbf{q} \Uparrow \mathbf{H}_{\text{ext}} \Uparrow \hat{\mathbf{z}}$, where z is indicating $\mathbf{s}_n \Uparrow \hat{\mathbf{z}}$ and $\bar{z}$ is indicating $\mathbf{s}_n \Downarrow \hat{\mathbf{z}}$. Within an inelastic neutron scattering experiment with polarization analysis, three main types of scattering events can be investigated independently within three consecutively probed channels. The three channels are monitoring three different differential cross sections: Two channels track spin-flip scattering mechanisms ($z \to \bar{z}$ and $\bar{z} \to z$) and one channel tracks non-spin-flip scattering mechanisms ($z \to z$). Incoherent scattering is neglected in the following. The cross-section of the non-spin-flip channel is given by

$$\frac{d^2\sigma}{d\Omega dE_{\text{f}}}|_{z \to z} = < N^*N >_{T,\omega} \, , \tag{3.18}$$

while the cross-sections of the two spin-flip channels yield

$$\frac{d^2\sigma}{d\Omega dE_{\text{f}}}|_{z \to \bar{z}} = < \mathbf{M}^*_\perp \cdot \mathbf{M}_\perp >_{T,\omega} + i < \mathbf{M}^*_\perp \times \mathbf{M}_\perp >_{T,\omega} \cdot \hat{z} \tag{3.19}$$

$$= S^{\text{xx}} + S^{\text{yy}} + i \cdot (S^{\text{xy}} - S^{\text{yx}}) \tag{3.20}$$

$$\frac{d^2\sigma}{d\Omega dE_{\text{f}}}|_{\bar{z} \to z} = < \mathbf{M}^*_\perp \cdot \mathbf{M}_\perp >_{T,\omega} - i < \mathbf{M}^*_\perp \times \mathbf{M}_\perp >_{T,\omega} \cdot \hat{z} \tag{3.21}$$

$$= S^{\text{xx}} + S^{\text{yy}} - i \cdot (S^{\text{xy}} - S^{\text{yx}}) \, . \tag{3.22}$$

Here, $< N^*N >_{T,\omega}$ with $N = N(\mathbf{q})$ describes coherent scattering on the nuclear structure of the sample (e.g. Bragg scattering or neutron-phonon scattering). Within this work the quantity of interest is the spectral function $i \cdot (S^{\text{xy}} - S^{\text{yx}})$ (see Eqs. (3.20), (3.22)), which is the Fourier transformation in space and time of the transversal spin-spin correlation function and related to chiral spin wave excitations. The chirality of magnetic excitations is defined as

$$\chi = \frac{i \cdot (S^{\text{xy}} - S^{\text{yx}})}{S^{\text{xx}} + S^{\text{yy}}} \, . \tag{3.23}$$

Thus, the chirality can only take values $-1 < \chi < +1$, due to the physical constraint of positive definite differential cross sections (see Eqs. (3.20) and (3.22)). In general, magnetic excitations appear in both spin-flip channels. If an excitation is fully chiral ($|\chi| = 1$), it appears in only one of the spin-flip channels depending on the chirality ($\chi = +1$ ($z \to \bar{z}$), $\chi = -1$ ($\bar{z} \to z$)).

The quantity $i \cdot (S^{xy} - S^{yx})$, which is only finite for chiral magnetic excitations ($\chi \neq 0$), is directly related to the amplitude of the spin Seebeck effect according to J. Barker and G.E.W. Bauer [15] (see section 2.3.3). Thus, the microscopic origin of the spin Seebeck effect can be directly accessed by the investigation of spin-flip scattering events within an inelastic neutron scattering experiment with polarization analysis.

3.1.1. Experimental setup for inelastic neutron scattering with polarization analysis

The inelastic neutron scattering experiments with polarization analysis are carried out at the instrument IN20 of the Institut Laue-Langevin (ILL) in Grenoble. The instrument IN20 is a triple axis spectrometer with polarization analysis offering a polarized neutron beam with a very high flux Φ_n within thermal energy range due to close vicinity to the reactor core ($\Phi_n(k_i = 2.662 \, \text{Å}^{-1}) = 1.05 \times 10^7 \, \text{cm}^{-2}\text{s}^{-1}$) [36]. A schematic drawing of the setup of IN20 is shown in Fig. 3.1.2. Due to legal issues a photograph of the setup cannot be provided.

Inelastic neutron scattering with polarization analysis

- ■ Heusler crystals (monochromator & analyzer)
- ■ Monitor (BF_3)
- ■ Neutron spin flipper
- ■ Sample inside magnet cryostat with $\mathbf{H}_{ext} \Uparrow \mathbf{q}$
- ■ Detector
- Incoming unpolarized neutron beam
- Polarized neutron beam (channel $z \rightarrow \bar{z}$)
- Polarized neutron beam (channel $\bar{z} \rightarrow z$)
- Polarized neutron beam (channel $z \rightarrow z$)
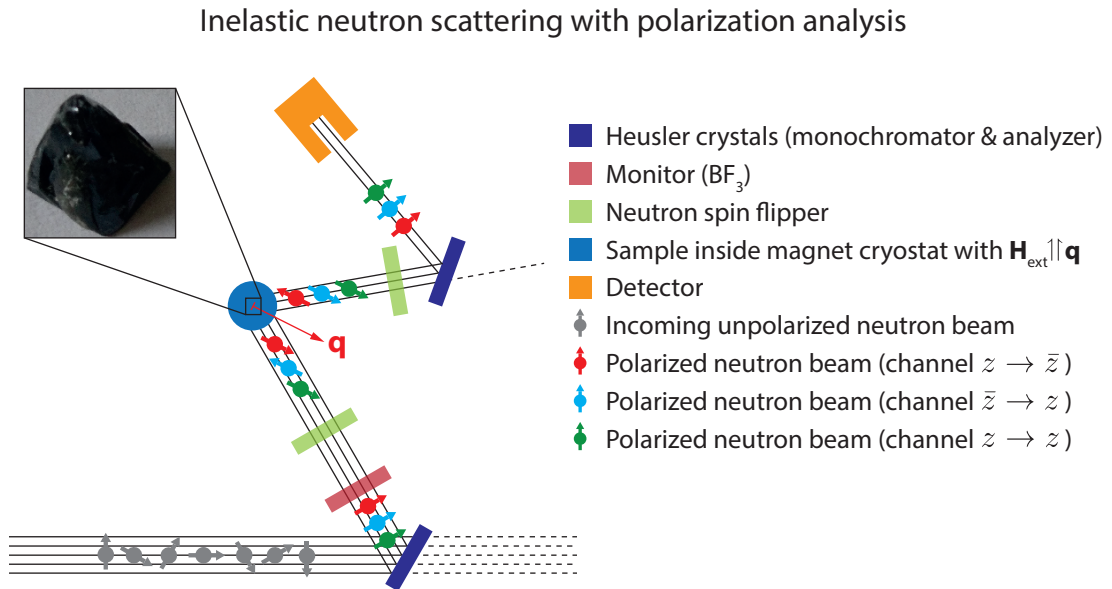
Figure 3.1.2.: Schematic drawing of the experimental setup for inelastic neutron scattering with polarization analysis. The incoming thermalized, diffuse neutron beam is monochromatized and polarized by scattering on a Heusler crystal. Subsequently, the monochromatic beam intensity is measured by a monitor filled with BF_3. To switch the spin polarization, the incident neutron beam is passed through a neutron spin flipper before being scattered on the sample inside a magnet cryostat, which is aligned such that $\mathbf{H}_{ext} \Uparrow \mathbf{q}$. The final beam is again passed through a neutron spin flipper, since the analyzing Heusler crystal is only selecting one neutron energy with fixed spin polarization to be analyzed in the detector. This setup with two Heusler crystals and two neutron spin flippers allows to separate spin-flip (red and blue neutrons) and non-spin-flip (green neutrons) scattering mechanisms. With this technique chiral spin wave excitations can be identified. The arrows on the neutrons depict the neutron spins $\mathbf{s}_n$.

Since the property under investigation is $\mathrm{i} \cdot (S^{\mathrm{xy}} - S^{\mathrm{yx}})$, which is related to chiral spin wave excitations, the external magnetic field $\mathbf{H}_{\mathrm{ext}}$ with a magnitude of $1\,\mathrm{T}$ has to be aligned parallel to the scattering vector $\mathbf{q}$. To identify the chiral spin wave excitations, the intensity of all three channels (two spin-flip channels $z \to \bar{z}$ (red), $\bar{z} \to z$ (blue) and one non-spin-flip channel $z \to z$ (green)) is measured at every measurement point in the four dimensional energy-momentum space. This allows to separate magnon-neutron and magnon-phonon scattering. For the control of the sample temperature and the external magnetic field, the Tb$_3$Fe$_5$O$_{12}$ single crystal (see inset of Fig. 3.1.2) is mounted on a cold finger inside a magnet cryostat. The experimental data is acquired at sample temperatures of $280\,\mathrm{K}$, $100\,\mathrm{K}$ and $10\,\mathrm{K}$ to cover all known magnetically ordered and structural phases of Tb$_3$Fe$_5$O$_{12}$ (see section 2.4.3).

3.1.2. Measurement procedure and data analysis

In the following, the vectors of the reciprocal space are given in lattice units relative to the conventional, bcc unit cell (conv. l. u.) of $Tb_3Fe_5O_{12}$ (TbIG). The experiments are conducted with the scattering vector parallel to the crystallographic $[111]_{bcc}$-direction of the cubic bcc-lattice: $\mathbf{q} \parallel [111]_{bcc}$. This is mandatory, since the measurement of spin wave excitations requires the magnetization to be aligned parallel to the scattering vector ($\mathbf{M}_{TbIG} \parallel \mathbf{q}$) (see section 3.1). Due to the large magnetic anisotropy of TbIG in particular at low temperatures, the measurement geometry is set with $\mathbf{q} \parallel [111]_{bcc}$, which is a magnetically easy axis, to ensure saturation of the magnetization of TbIG within an external magnetic field of $\mu_0 H_{ext} = 1\,T$ at all temperatures.

Since small angle scattering is not possible with a triple axis spectrometer, the experiment is carried out along the $[111]_{bcc}$-direction around the TbIG Bragg-reflection (444) with reciprocal lattice vector $[444]_{bcc}$, which is the Γ-point in this Brillouin-zone. Thus, the experiments are performed for $\mathbf{q} \in [\Gamma P]$ with the center of the Brillouin-zone Γ and the corner of the Brillouin-zone $P = [3.5\ 3.5\ 3.5]_{bcc}$, at a fixed scattering vector $\mathbf{q}$ with a step size of $\Delta \mathbf{q} = [0.1\ 0.1\ 0.1]_{bcc}$, while scanning the energy loss of the scattered neutron $E = E_i - E_f$. The energy loss is scanned within estimated regions of interest according to previous simulations of spin wave dispersion relations for the similar material system $Gd_3Fe_5O_{12}$ (GdIG) [16]. Depending on the energy range, an energy step size between $\Delta E = 0.1\,meV - 1\,meV$ is used.

Furthermore, the experiments are conducted with a fixed final wave vector of the neutron $\mathbf{k}_f$ while sweeping the size of the initial wave vector $\mathbf{k}_i$. In this way $\mathbf{k}_f$ can be selected to match a peak of the analyzer and detector efficiency. Additionally, this procedure guarantees a constant detector efficiency such that no post-processing of the data is required. To calculate the scattering rate, the events counted by the detector are normalized to the monitor counts, which are chosen as 10^6 monitor counts for both spin-flip channels ($z \rightarrow \bar{z}$ (red), $\bar{z} \rightarrow z$ (blue)) and 10^5 monitor counts for the non-spin-flip channel ($z \rightarrow z$ (green)). In total, this procedure gives a three-dimensional intensity-map $I(E, \mathbf{q})$ consisting of energy loss line scans at fixed scattering vectors $I(E, \mathbf{q})|_{\mathbf{q} \in [\Gamma P]}$.

For the processing of a chirality dependent spin wave dispersion relation, the line scans of the three channels (red, blue, green) are fitted by a superposition of Gaussian-functions on top of a baseline accounting for the background. The resulting peak positions are then plotted with corresponding colors as data points in an $E - \mathbf{q}$ diagram revealing the chirality dependent spin wave dispersion relation of TbIG.

3.2. Inelastic Neutron scattering with polarization analysis at 280 K

At $280\,K$, $Tb_3Fe_5O_{12}$ (TbIG) shows no rhombohedral distortion and is described by the body centered cubic Ia3d space-group, which is identical to the space-group of $Gd_3Fe_5O_{12}$ (GdIG). The cubic magnetic anisotropy with magnetically easy axes along the cubic $[111]_{bcc}$-directions present in TbIG is considerably weak and thus negligible. The magneti-

zation of the magnetic Tb^{3+}-sublattice is small within the collinear ferrimagnetic structure of TbIG at $280\,K$. Overall, the properties of TbIG are similar to that of GdIG at $280\,K$. Thus, the expectation is to find a spin wave dispersion relation similar to the theoretically calculated spin wave dispersion relation previously reported by Geprägs *et al.* (see Fig. 2.4.4) [16].

The experimental data of inelastic neutron scattering with polarization analysis at a sample temperature of $280\,K$ is shown in Fig. 3.2.1. The raw data normalized to the monitor counts is plotted as data points in colors depicting the different scattering channels ($z \to \bar{z}$ (red), $\bar{z} \to z$ (blue), $z \to z$ (green)) together with the fitted superposed Gaussian-functions as solid lines in respective colors (see Fig. 3.2.1 (a)). The extracted peak positions are then plotted in Fig. 3.2.1 (b) for all measurements at different scattering vectors $\mathbf{q}$.

At the Γ-point ($\mathbf{q} = [444]$, see Fig. 3.2.1 (a)), magnon modes around $30\,meV$ to $37\,meV$ are clearly visible in the blue spin-flip channel with $i \cdot (S^{xy} - S^{yx}) < 0$, while only at low energy loss ($E < 15\,meV$) a finite intensity is observed in the red spin-flip channel with $i \cdot (S^{xy} - S^{yx}) > 0$. The tail at low energies is considered as a data point in Fig. 3.2.1 (b) with a large error bar (see also Fig. B.0.1). For $\mathbf{q} = [3.8\ 3.8\ 3.8]$ a chiral magnon mode in the blue channel ($i \cdot (S^{xy} - S^{yx}) < 0$) at an energy loss of $37\,meV$ is found. The tail in the red channel at an energy loss $E < 25\,meV$ is considered as data point with large uncertainty in Fig. 3.2.1 (b). At $\mathbf{q} = [3.7\ 3.7\ 3.7]$ another chiral magnon mode in the red channel is located, which seems to be connected to the red modes found at scattering vectors $\mathbf{q}$ closer to the Γ-point ($\mathbf{q} = [444]$). Additionally, a chiral magnon mode in the red channel is visible at $\mathbf{q} = [3.5\ 3.5\ 3.5]$ with an energy loss of $E = 32\,meV$. The pronounced intensity increase at low energy loss ($E < 8\,meV$) is considered as artefact of elastic scattering (see finite intensity in the non-spin flip (green) channel) and is not related to magnetic excitations.

Overall, the measurement at $280\,K$ shows a strongly dispersing fully chiral band in the red channel ($i \cdot (S^{xy} - S^{yx}) > 0$) starting at low energy at the Γ-point up to $32\,meV$ at the P-point (see Fig. 3.2.1 (b)). Furthermore, the peak positions extracted from the blue ($i \cdot (S^{xy} - S^{yx}) < 0$) spin-flip channel with $30\,meV$ at Γ and with $37\,meV$ at $\mathbf{q} = [3.8\ 3.8\ 3.8]$ correspond to a second optical mode with opposite chirality to the red mode at lower energies. Compared to the spin wave dispersion relation in GdIG at $40\,K$ (see Fig. 2.4.4), all modes found here have opposite chirality. This is attributed to the crossing of the magnetic compensation temperature $T_{comp,TbIG} = 250.5\,K$ leading to an inversion of all magnetic moments and spin wave chiralities in a finite external magnetic field.

Due to the leakage of the elastic scattering into the spin-flip channels and the low energy resolution, no magnon bands could be resolved in the low energy region with $E < 3\,meV$. Presumably, those bands, which should be chiral as well, could be found in inelastic neutron scattering experiments with cold neutrons due to the higher energy resolution in the low energy regime.
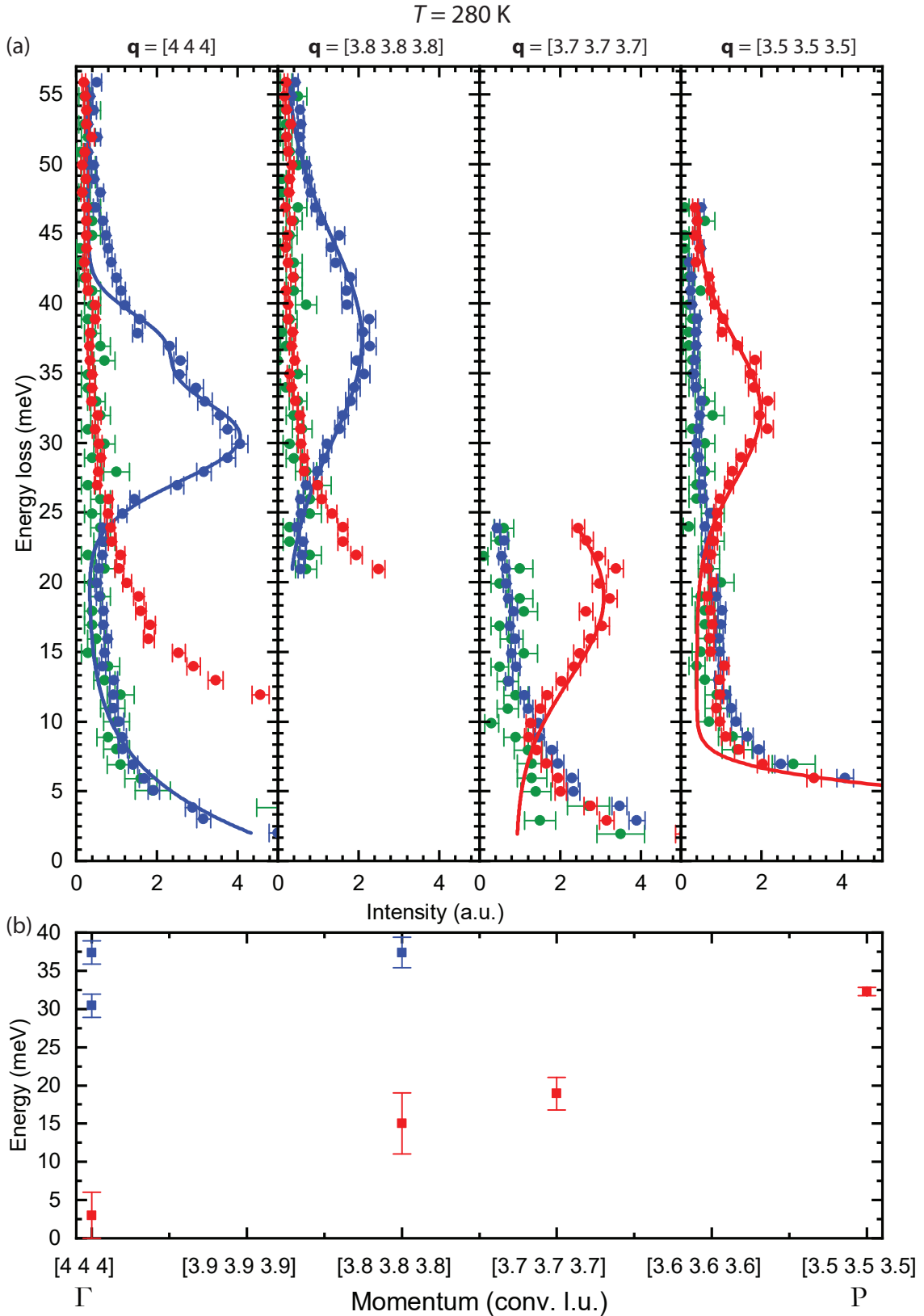
Figure 3.2.1.: Inelastic neutron scattering with polarization analysis at $T = 280\,\mathrm{K}$. The color depicts the different scattering channels: non-spin-flip channel (green), spin-flip channel with $\mathrm{i} \cdot (S^{xy} - S^{yx}) < 0$ (blue) and $\mathrm{i} \cdot (S^{xy} - S^{yx}) > 0$ (red). (a) Intensity normalized to the monitor counts as a function of the energy loss for different scattering vectors **q**. The intensity is fitted with superposed Gaussian-functions (solid lines). (b) Extracted energy values of magnon modes. The tail in the red channel ($\mathrm{i} \cdot (S^{xy} - S^{yx}) > 0$) at **q** $= [444]$ (Γ-point) in (a) is considered as a data point with a large uncertainty in (b) (see also Fig. B.0.1).

3.3. Inelastic Neutron scattering with polarization analysis at 100 K

With decreasing the sample temperature to $100\,K$, changes in the crystal structure and the magnetic structure of TbIG occur. At $100\,K$, TbIG exhibits a rhombohedral distortion, characterized by an angle $\Delta\alpha_{rh,280K-100K} = 0.03°$. This leads to a reduction of the crystal symmetry to the rhombohedral R$\bar{3}$ space group. Within the R$\bar{3}$ space group, the degeneracy of the Tb^{3+}-ions is lifted to two non-degenerate $6e$ (Tb) and $6e'$ (Tb') sites. Additionally, the magnetic structure changes to the non-collinear 'double-umbrella' structure, where the magnetic moments of the Tb- and Tb'-ions form a cone with opening angles $\theta > \theta'$ around the magnetic easy axis parallel to the cubic $[111]_{bcc}$-direction within three degenerate glide planes $[111]_{bcc} \times [100]_{bcc}$ [23, 33] (see section 2.4.3). With decreasing temperature, the Tb-sublattice magnetization increases, which is typical for rare-earth iron garnets with magnetic rare-earth-ions (see Fig. 2.4.2).

The experimental data acquired by inelastic neutron scattering with polarization analysis on a TbIG single crystal at a sample temperature of $100\,K$ is shown in Fig. 3.3.1. To extract the energy position of the magnon modes, the intensity as a function of energy loss (data points) is fitted by superposed Gaussian-functions (see solid lines in Fig. 3.3.1 (a)). The extracted peak positions are then plotted as a function of the momentum (see Fig. 3.3.1 (b)).

Compared to the inelastic neutron scattering experiment at a sample temperature of $280\,K$, the coloring of all modes, i.e. the chirality, is inverted due to the crossing of the magnetic compensation temperature $T_{comp} = 250.5\,K$. The previously strongly dispersing mode (red mode in Fig. 3.2.1) is shifted to higher energies with an energy gap of $E_{gap} = 5\,meV$ at the Γ-point and a maximum energy of $40\,meV$ at the P-point. The opening and the size of the energy gap at the Γ-point is mainly correlated to the increasing Tb-sublattice magnetization with decreasing temperatures. The splitting of this mode into two modes at $\mathbf{q} = [444]$, $\mathbf{q} = [3.7\ 3.7\ 3.7]$ and $\mathbf{q} = [3.5\ 3.5\ 3.5]$ is most likely related to the coupling of magnons to ligand-field excitations in TbIG previously reported by Kang *et al.* [34]. The energy of the second optical mode at the Γ-point (finite signal at $E > 35\,meV$ in the red spin-flip channel) also shifted up in energy compared to $280\,K$, which was also found in simulations of spin wave dispersion relations in the material system GdIG [16]. In line with the data at a sample temperature of $280\,K$, magnon modes at low energy ($E < 3\,meV$) could not be resolved. In particular, the acoustic magnon modes as well as expected flat bands which are visible in the spin wave dispersion relation of the similar material system GdIG (see red bands with $E < 3\,meV$ in Fig. 2.4.4) need to be verified in further experiments with cold neutrons. Overall, the experimental spin wave dispersion relation at $100\,K$ matches the simulated dispersion relation of GdIG at $40\,K$ except the splitting of the low energy magnon mode due to the ligand-field excitations. Hence, the experimentally determined spin wave dispersion relation does not show attributes which can be directly connected to the non-collinear 'double-umbrella' magnetic structure.
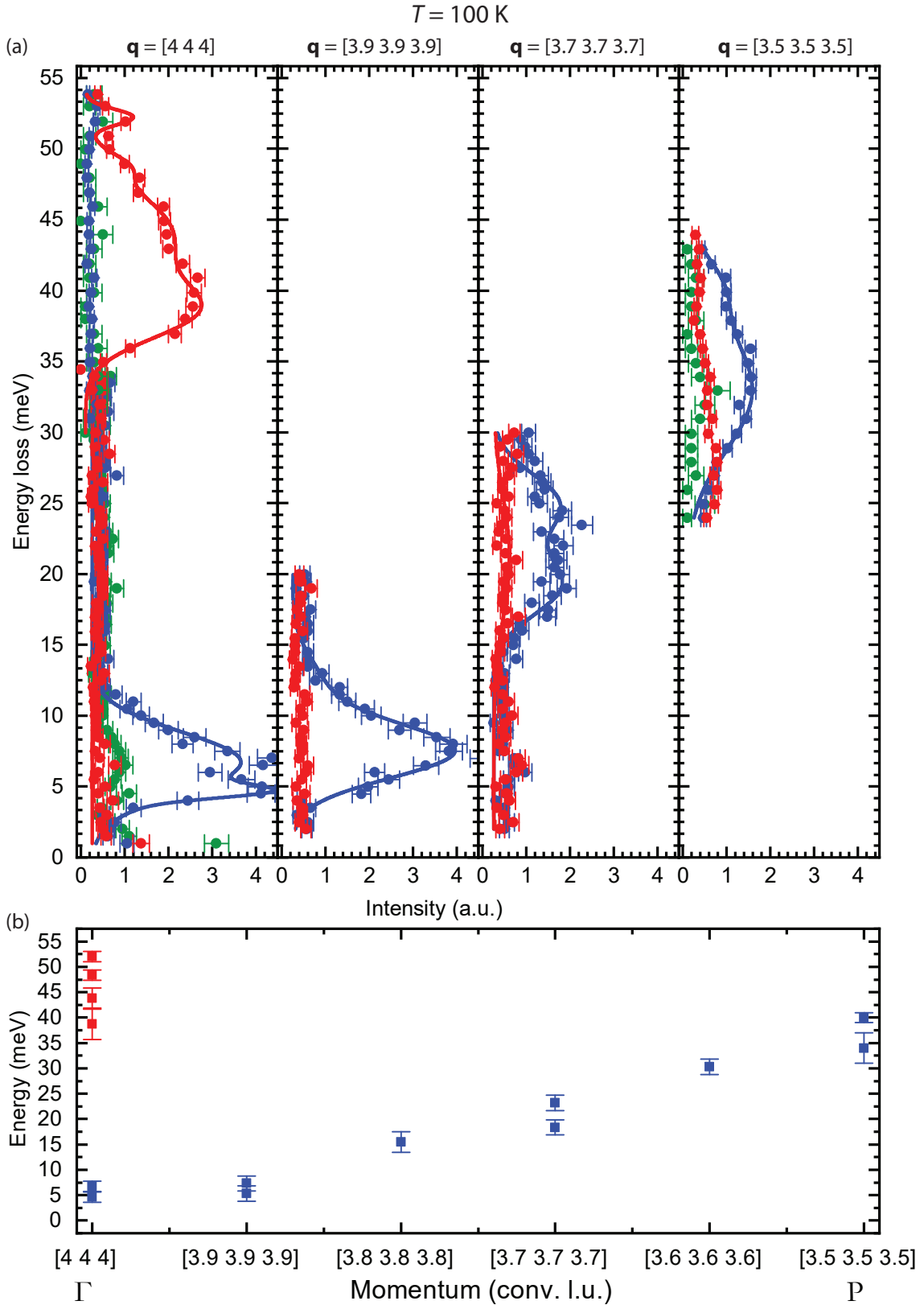
Figure 3.3.1.: Inelastic neutron scattering with polarization analysis at $T = 100$ K. The color depicts the different scattering channels: non-spin-flip channel (green), spin-flip channel with $i \cdot (S^{xy} - S^{yx}) < 0$ (blue) and $i \cdot (S^{xy} - S^{yx}) > 0$ (red). (a) Intensity normalized to the monitor counts as a function of the energy loss for different scattering vectors $\mathbf{q}$. The intensity is fitted with superposed Gaussian-functions (solid lines). (b) Extracted energy values of magnon modes. The data shows clearly the first optical mode in blue which is split due to the coupling of magnons to ligand field excitations.

3.4. Inelastic Neutron scattering with polarization analysis at 10 K

At a sample temperature of $10\,\mathrm{K}$, the rhombohedral distortion increases further to $\Delta\alpha_{\mathrm{rh,280K-10K}} = 0.06°$ as well as the opening angles $\theta = 31.37°$ and $\theta' = 26.46°$ of the 'double-umbrella' structure. The Tb-sublattice magnetization is saturated with $7.6\mu_{\mathrm{B}}/\mathrm{ion}$ at $10\,\mathrm{K}$ with a large cubic magnetic anisotropy of the total magnetization along the cubic $[111]_{\mathrm{bcc}}$-directions.

The results of the inelastic neutron scattering experiment with polarization analysis on a TbIG single crystal at a sample temperature of $10\,\mathrm{K}$ are shown in Fig. 3.4.1. The energy positions of the magnon modes are extracted by fitting the intensity (data points) with superposed Gaussian functions (solid lines in Fig. 3.4.1 (a)). The extracted energies of the magnon modes are then plotted as a function of momentum in Fig. 3.4.1 (b).

In line with the previously discussed results, the experiment at $10\,\mathrm{K}$ is able to track the first optical, blue mode from the Γ-point at $10\,\mathrm{meV}$ to the P-point at $41\,\mathrm{meV}$. Additionally, the second optical, red mode is found at the Γ-point. These two optical modes shift further upwards in energy with decreasing temperatures, again, in agreement with simulations of the spin wave dispersion in GdIG [16]. In accordance with the data published by Kang *et al.* on the coupling of magnons at the Γ-point of the first optical blue mode to ligand-field excitations in TbIG (see Fig. 2.4.7), the splitting at the Γ-point increased relatively to the splitting at $100\,\mathrm{K}$.

In addition to the two optical modes, the experiment revealed two dispersionless red bands at $11\,\mathrm{meV}$ and $30\,\mathrm{meV}$. At around $11\,\mathrm{meV}$, a small intensity above the noise level within the green, non-spin-flip channel is observed. Due to the low intensity in the green channel, a leakage from a phonon-neutron scattering mechanism, which should only appear in the non-spin-flip channel, into the spin-flip channels can be excluded. Nevertheless, a structural excitation is visible, which should be subject to further investigation.

Similar to the data acquired at $280\,\mathrm{K}$ and $100\,\mathrm{K}$, the experiment could not resolve any of the acoustic and flat bands in the low energy region $< 10\,\mathrm{meV}$, which are predicted for the similar material system GdIG (see Fig. 2.4.4).
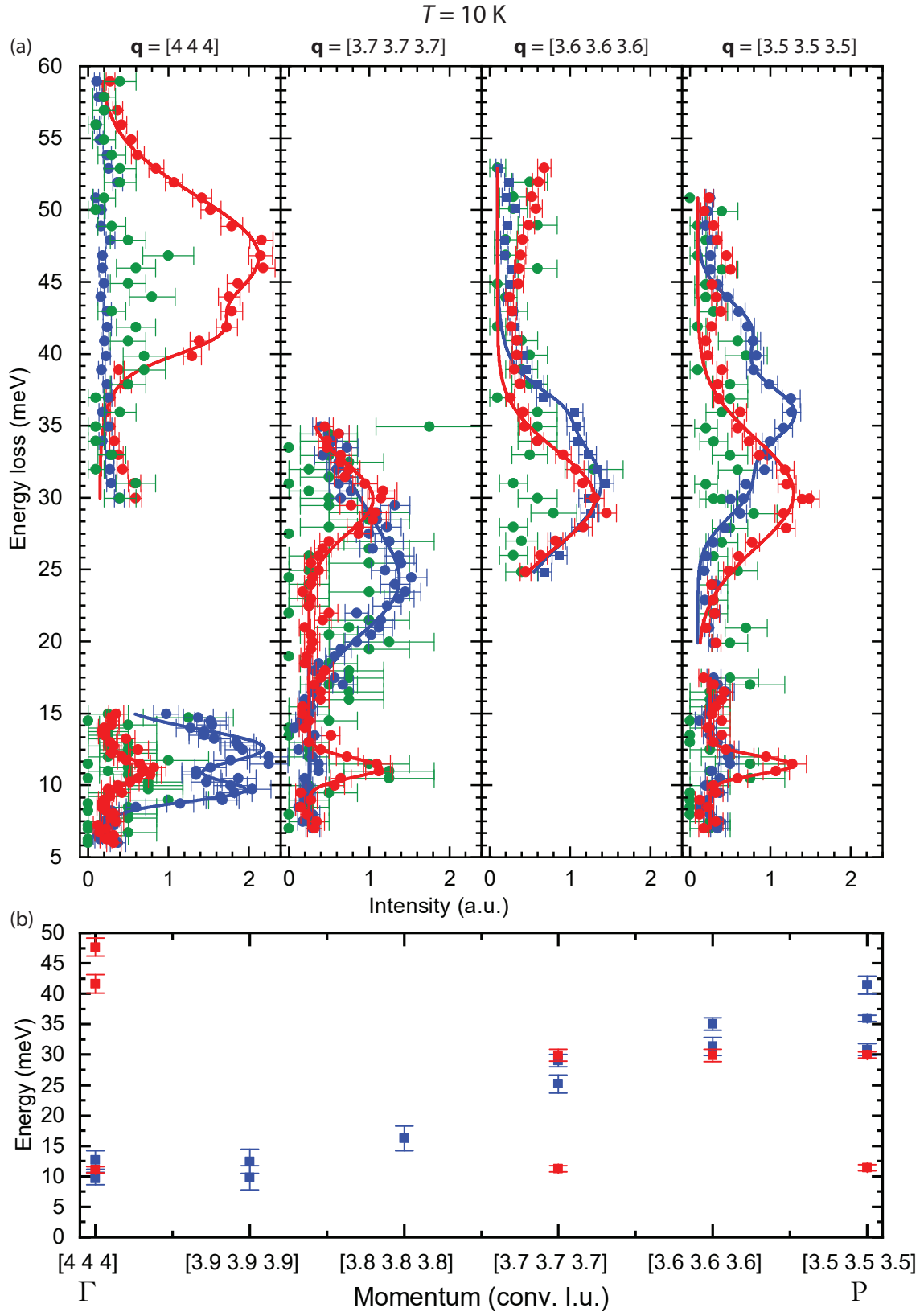
Figure 3.4.1.: Inelastic neutron scattering with polarization analysis at $T = 10\,K$. The color depicts the different scattering channels: non-spin-flip channel (green), spin-flip channel with $i \cdot (S^{xy} - S^{yx}) < 0$ (blue) and $i \cdot (S^{xy} - S^{yx}) > 0$ (red). (a) Intensity normalized to the monitor counts as a function of the energy loss for different scattering vectors **q**. The intensity is fitted with superposed Gaussian-functions (solid lines). (b) Extracted energy values of magnon modes. Compared to the data at $100\,K$, the energy gap of the first optical mode increased with an increase of the splitting at the Γ-point which is attributed to the coupling of magnons to ligand-field excitations [34].

3.5. Summary - Inelastic neutron scattering with polarization analysis on a $Tb_3Fe_5O_{12}$ single crystal

In total, inelastic neutron scattering with polarization analysis is able to reveal the first optical and second optical mode with opposite chirality at $10\,\mathrm{K}$, $100\,\mathrm{K}$ and $280\,\mathrm{K}$. Both modes are fully chiral ($|\chi| = 1$) at the investigated temperatures. With increasing temperature, the first optical mode shifts downwards in energy from $10\,\mathrm{meV}$ at $10\,\mathrm{K}$ to approximately zero energy at $280\,\mathrm{K}$. Also the second optical mode shifts down in energy with increasing temperatures. These shifts are mainly correlated to the decreasing Tb-sublattice magnetization with increasing temperatures, which is leading to a decrease of the exchange-field originating from the Tb-sublattice. Overall, this results in a decrease of the energy at the Γ-point of both optical modes. Additionally, an inversion of the chirality of all magnon modes at $280\,\mathrm{K}$ compared to $100\,\mathrm{K}$ and $10\,\mathrm{K}$ is observed due to the inversion of the sublattice magnetizations while crossing the magnetic compensation at $T_{\mathrm{comp}} = 250.5\,\mathrm{K}$ (see section 2.4.3). The acoustic bands and flat band structure which are expected at low energies $E < 5\,\mathrm{meV}$ could not be resolved within the experiments and should be subject to further inelastic neutron scattering experiments on TbIG with cold neutrons in the low energy range.

In the following chapter, the experimental data discussed here is used to simulate the full spin wave dispersion relation in TbIG at $10\,\mathrm{K}$, $100\,\mathrm{K}$ and $280\,\mathrm{K}$ and to extract the exchange constants of TbIG at different temperatures.

4. Simulation of spin wave dispersion relations with SpinW

This chapter describes the simulation of the full spin wave dispersion of $Tb_3Fe_5O_{12}$ for different temperatures using SpinW. The goal is to get the best possible agreement between the simulated spin wave dispersion relation and the data of the inelastic neutron scattering experiment with polarization analysis discussed in the previous chapter. In the first part, the theory behind the used simulation tool SpinW is presented. Subsequently, the simulation of the spin wave dispersion relation in $Tb_3Fe_5O_{12}$ is obtained by first simulating the spin wave dispersion relations in the well known material systems $Y_3Fe_5O_{12}$ and $Gd_3Fe_5O_{12}$. The main part of this chapter then focuses on the simulation results for spin wave dispersion relations in $Tb_3Fe_5O_{12}$ at $280\,K$, $100\,K$ and $10\,K$, to cover all magnetic and structural phases present in $Tb_3Fe_5O_{12}$.

4.1. Simulation of spin wave dispersion relations with SpinW

SpinW is a MATLAB-based simulation tool which allows to simulate spin wave dispersion relations within an advanced Heisenberg model using a semi-classical ansatz [37]. SpinW considers the Hamilton operator

$$H = \sum_{mi,nj} \mathbf{S}_{mi}^T \cdot J_{mi,nj} \cdot \mathbf{S}_{nj} + \sum_{mi} \mathbf{S}_{mi}^T \cdot A_i \cdot \mathbf{S}_{mi} + \mu_B \mathbf{H}^T \sum_{mi} g_i \mathbf{S}_{mi} \,, \tag{4.1}$$

which allows to simulate a specific material system considering magnetic exchange interactions $J_{mi,nj}$, where m, n label the unit cell and i, j the magnetic moment within the unit cell, as well as the Dzyaloshinskii–Moriya interaction and anisotropies A_i acting on the magnetic moments $\mathbf{S}_{mi}$ under an external magnetic field $\mathbf{H}$. Here, g_i is the g-factor for the atom on site i, which can differ from the free-ion value due to e.g. crystal field effects. SpinW diagonalizes the Hamiltonian by applying the Holstein-Primakoff transformation as well as by subsequently applying a numerical method of the Bogoliubov transformation for antiferromagnets or ferrimagnets. For the diagonalization of the Hamiltonian, SpinW uses approximations within the linear spin wave theory. The eigenvalues of the diagonalized Hamiltonian describe the dispersion relation and the spin-spin correlation function

$$S^{\alpha\beta}(\mathbf{q}, \omega) = \frac{1}{2\pi\hbar} \int dt\, e^{-\mathrm{i}\omega t} < S^\alpha(\mathbf{q}, 0) S^\beta(\mathbf{q}, t) > \tag{4.2}$$

is determined from the eigenvectors. SpinW does not account for thermal effects and thus can only provide insights into magnon properties at $0\,K$, neglecting second or higher order processes e.g. magnon-magnon and magnon-phonon scattering. A more detailed descrip-

tion of the algorithm used to diagonalize the Hamiltonian (4.1) is given in Ref. [37]. The schematic work-flow for the setup of a simulation with SpinW is shown in Fig. 4.1.1. The required inputs are the crystallographic structure defined by its space group, and the magnetic coupling constants $J_{\mathrm{mi,nj}}$ as well as the spin-values for each ion site which in total defines the structure of the magnetic interaction. Additionally, one can define site-dependent g-factors and anisotropies A. In the next step, the magnetic structure can be generated by SpinW using a mean field optimization or can be directly input using e.g. an experimentally determined magnetic structure. In both cases, SpinW allows a multi-sublattice ferrimagnetic structure, which is present in compensated ferrimagnets such as $Y_3Fe_5O_{12}$, $Gd_3Fe_5O_{12}$ and $Tb_3Fe_5O_{12}$.

According to J. Barker and G.E.W. Bauer [15], the spin Seebeck effect is mainly driven by the frequency and wave vector integral over

$$\mathrm{Im}\big(<\omega S^{\mathrm{x}}(\mathbf{q},\omega)S^{\mathrm{y}*}(\mathbf{q},\omega)> - <\omega S^{\mathrm{y}}(\mathbf{q},\omega)S^{\mathrm{x}*}(\mathbf{q},\omega)> \big) = \omega\,\mathrm{Im}\big(S^{\mathrm{xy}}(\mathbf{q},\omega) - S^{\mathrm{yx}}(\mathbf{q},\omega)\big) \tag{4.3}$$

multiplied with the Bose-Einstein distribution (see section 2.3.3). Thus, in the following together with the spin wave dispersion relation also the antisymmetric transverse spectral function $\mathrm{i}\cdot(S^{\mathrm{xy}}(\mathbf{q},\omega) - S^{\mathrm{yx}}(\mathbf{q},\omega))$ is plotted in a false color representation. The color indicates the chirality of the spin wave excitations, which is equivalent to the spin of the magnon in a particle picture. Here, the $+$ $(-)$ sign represents the magnon spin parallel (antiparallel) to the external magnetic field as well as the polarization strength of the band.
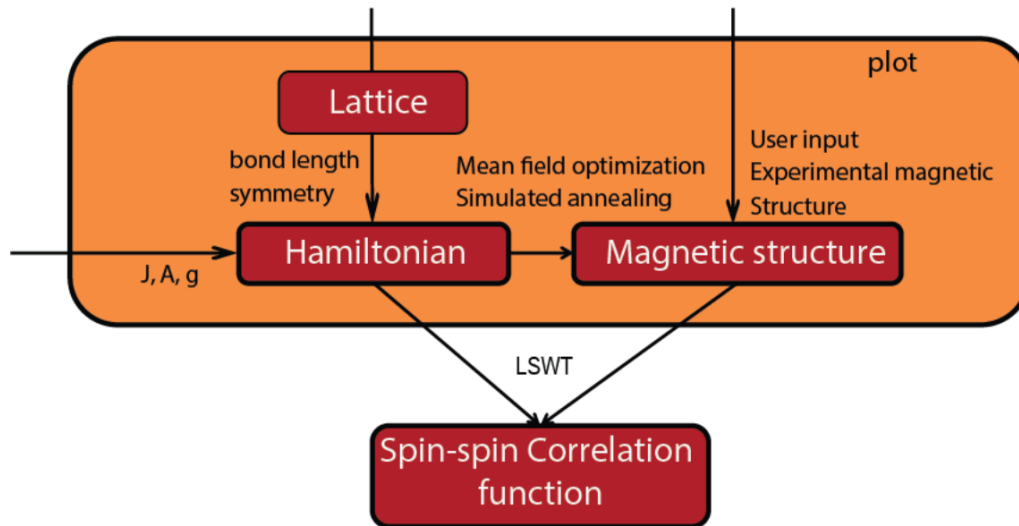
Figure 4.1.1.: Schematic work-flow for the setup of a SpinW simulation. The required inputs for the simulation are the lattice structure and all microscopic parameters for the definition of the structure of the magnetic interaction (exchange interaction matrix J, anisotropy vector A, g-factor). The magnetic structure can be generated by SpinW using a mean field optimization or an experimentally determined magnetic structure can be input directly. The result of the simulation is the spin wave dispersion relation and the spin-spin correlation function, which is obtained by diagonalization of the Hamiltonian within the linear spin wave theory (LSWT). Figure taken from Ref. [38].

4.2. Simulation of the spin wave dispersion relation of $Y_3Fe_5O_{12}$
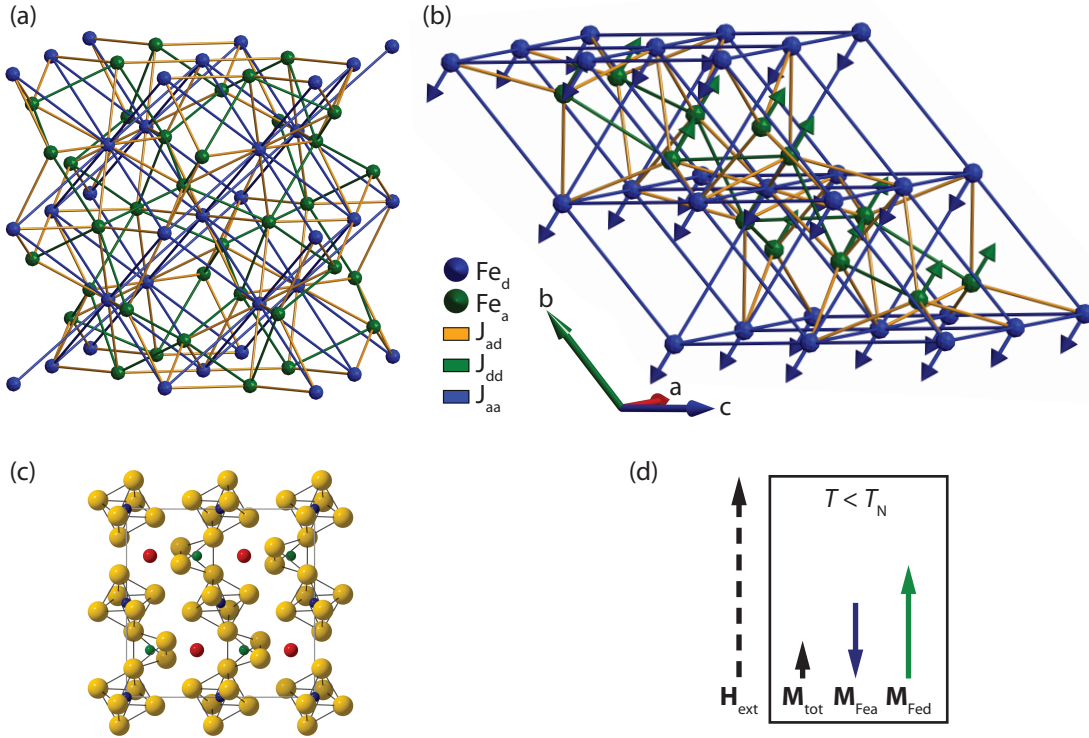
Figure 4.2.1.: (a) Magnetic structure of $Y_3Fe_5O_{12}$ with Fe^{3+} ions on the d-site (Fe_d, blue spheres) and a-site (Fe_a, green spheres) shown in the conventional body centered cubic unit cell with space group Ia3d. The conventional unit cell contains 40 magnetic atoms and has a lattice constant of $a_{bcc,yig} = 12.376$ Å [39]. The exchange interactions between the same iron sites (J_{dd} and J_{aa}) as well as between the two different iron sites (J_{ad}) are marked by green, blue, and orange lines. (b) Magnetic Fe^{3+}-ions shown in the primitive, rhombohedral unit cell of the bcc-lattice ($a_{YIG,rh} = 10.718$ Å, $\alpha_{YIG,rh} = 109.47°$). The rhombohedral, primitive unit cell contains 20 magnetic atoms. The orientation of the magnetic moments of the Fe^{3+}-ions along the cubic $[111]_{bcc}$-direction are marked with blue and green arrows. (c) Center layer of the conventional bcc unit cell of $Y_3Fe_5O_{12}$ with the O^{2-}-polyhedra (yellow spheres) surrounding the Fe^{3+}-ions. The Fe_a^{3+}-ions are octahedrally coordinated with 6 O^{2-}-ions whereas the Fe_d^{3+}-ions are tetrahedrally coordinated with 4 O^{2-}-ions. (d) Schematic drawing of the orientation of the sublattice magnetizations $\mathbf{M}_{Fea}$ and $\mathbf{M}_{Fed}$ as well as the total magnetization $\mathbf{M}_{tot}$ of YIG for $T < T_N$ under a finite external magnetic field $\mathbf{H}_{ext}$.

As a starting point, the more simple compound $Y_3Fe_5O_{12}$ (YIG) is chosen with the aim to reproduce the results of the SpinW-simulation of the spin wave dispersion relation recently published by Princep *et al.* [28].

YIG crystallizes in the body centered cubic Ia3d space group with 4 formula units per lattice point. The conventional bcc unit cell of YIG is shown in Fig. 4.2.1 (a) and (c) with the Fe_d-site and Fe_a-site marked in blue and green, respectively, and the non-magnetic Y_c-site marked in red. The rhombohedral, primitive unit cell of YIG is shown in Fig. 4.2.1 (b). In Fig. 4.2.1 (a) and in the following figures illustrating the crystalline and magnetic structure, the oxygen ions are not shown for better visibility. Additionally, the exchange interactions originating from the antiferromagnetic superexchange via the oxygen ions between the magnetic Fe^{3+}-ions are depicted by orange (J_{ad}), green (J_{dd}), and blue (J_{aa}) lines. The

primitive unit cell with the coordinate system **a-b-c** and the magnetic moments of the 20 Fe^{3+}-ions (blue and green arrows) aligned along the magnetic easy axis parallel to $[111]_{bcc}$ ($[111]_{bcc}||[111]_{prim}$) is shown in Fig. 4.2.1 (b). The ferrimagnetic ordering for $T < T_N \approx 550K$ of the Fe^{3+}-ions is resulting from the dominant antiferromagnetic inter-sublattice exchange interaction J_{ad} (orange lines in Fig. 4.2.1 (b)) between the two magnetic Fe^{3+}-sites. The antiferromagnetic intra-sublattice exchange interactions between the same Fe-sites (J_{aa} and J_{dd}) are weaker, since the respective exchange paths are much longer. The resulting orientation of the sublattice magnetizations $\mathbf{M}_{Fea}$ and $\mathbf{M}_{Fed}$ as well as the total magnetization $\mathbf{M}_{tot}$ of YIG are schematically shown in Fig. 4.2.1 (d) for $T < T_N$ under a finite external magnetic field $\mathbf{H}_{ext}$.

To reproduce the SpinW-simulation reported by Princep *et al.* [28], a SpinW-code is written based on the YIG-structure shown in Fig. 4.2.1 (a). The exchange interactions used by Princep *et al.* are listed in Table 4.2.1. These exchange interactions were determined by refining the simulated magnon dispersion relation to data acquired by a time-of-flight inelastic neutron scattering experiment [28]. Princep *et al.* reported two non-degenerate Fe_a-Fe_a couplings J_{aa1} and J_{aa2} with identical coupling length due to different Fe-O-Fe pathways, which affects the coupling strength of the O^{2-}-superexchange. Furthermore, the authors considered next-nearest neighbour (nnn) interactions resulting in a total of 6 non-degenerate magnetic bond types.

Coupling constant	Coupling energy (meV)
J_{ad}	6.8
J_{dd}	0.52
J_{aa1}	0
J_{aa2}	1.1
$J_{ad,nnn}$	−0.07
$J_{dd,nnn}$	0.47
$J_{aa,nnn}$	−0.009

Table 4.2.1.: Magnetic exchange couplings of YIG reported by Princep *et al.* acquired by refining the simulated spin wave dispersion relation (see Fig. 4.2.2) to data of a time-of-flight inelastic neutron scattering experiment [28]. These values are used as input for the SpinW-simulation shown in Fig. 4.2.2 (b).

With the use of these exchange parameters, the spin wave dispersion relation of YIG reported by Princep *et al.* is reproduced [28] (see Fig. 4.2.2). The difference in the coloring of the reproduced spin wave dispersion relation (see Fig. 4.2.2 (b)) compared to the spin wave dispersion relation reported by Princep *et al.* (see Fig. 4.2.2 (a)) can be traced back on post-processing of the published figure. This demonstrates, that the SpinW-code, which is set up to reproduce these results is valid and yields reasonable results.

The first key feature of the spin wave dispersion relation of YIG is the non-gapped fundamental ferrimagnetic resonance mode up to $25\,\text{meV}$, colored in red due to positive chirality of the spin wave excitation (spin angular momentum of the magnon $\Uparrow \mathbf{M}_{tot,YIG}$, $i \cdot (S^{xy} - S^{yx}) > 0$). Subsequently, the second key feature is the optical mode, colored in blue due to opposite chirality, which is strongly dispersing and gapped at the Γ-point.
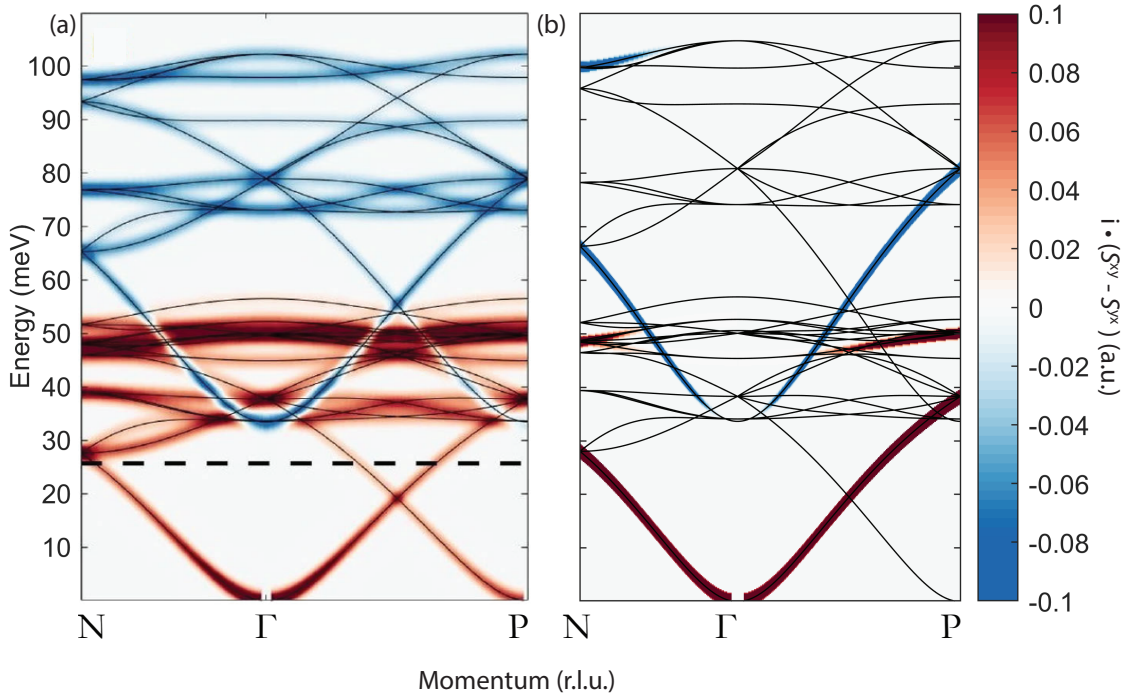
Figure 4.2.2.: (a) SpinW simulation of the spin wave dispersion relation of YIG, which was re-fined to a time-of-flight inelastic neutron scattering data set, reported by Princep *et al.* [28]. (b) SpinW simulation of YIG set up within this work with identical exchange coupling constants as found by Princep and coworkers. The simulation is able to reproduce the spin wave dispersion relation reported by Princep *et al.*. The different contrast in the coloring might be originating from post-processing of figure obtained by SpinW. The two key features are the ferrimagnetic resonance mode (red) and the first optical mode with opposite chirality (blue), which has an energy gap at the Γ-point.

When comparing the spin wave dispersion relations in Fig. 4.2.2 with previously calculated dispersion relations (e.g. Fig. 4.2.3 (a)), one finds that the dispersion relation obtained by using the magnetic structure of YIG reported by Princep *et al.* shows a high number of bands. Especially those bands running from high energy at the N-point to low energy at the P-point or vice versa (e.g. non-gapped red band at the P-point in Fig. 4.2.2 (a)) might be not real due to the missing inversion symmetry in the vicinity of the Γ-point.

The solution to this problem is to implement the primitive, rhombohedral unit cell within the SpinW simulation (see Fig. 4.2.1 (b)). Since SpinW takes the given unit cell as primitive unit cell, it diagonalizes an Hamilton operator of the size $n \times n$ where n is the number of magnetic atoms within the given unit cell. Thus, in a maximum non-degenerate case, SpinW calculates n non-degenerated magnon bands. Therefore, this will result in partially artificial magnon bands in the case of a given non-primitive unit cell.

Figure 4.2.3 (b) shows a spin wave dispersion relation calculated by SpinW, where the input is the primitive, rhombohedral unit cell of YIG. To compare the simulation results, the coupling constants reported by J. Barker and G.E.W. Bauer (see Table 4.2.2) are used for this simulation [15]. The comparison with the magnon dispersion relation in the low temperature regime ($T = 1 \, \text{K}$) obtained by J. Barker and G.E.W. Bauer (see Fig. 4.2.3 (a)) reveals, that the SpinW-simulation which is set up within this work, is able to achieve similar re-

sults. Thus, the solutions obtained by the diagonalization of the Heisenberg Hamiltonian within the linear spin wave theory, using the SpinW-code are valid.

Coupling constant	Coupling energy (meV)
J_{ad}	20.0
J_{dd}	6.7
J_{aa}	1.9

Table 4.2.2.: Exchange coupling constants of YIG used by J. Barker and G.E.W. Bauer to calculate the spin wave dispersion relation of YIG shown in Fig. 4.2.3 (a). The authors used normalized spins for their model. Within this work, these coupling constants are utilized to reproduce the spin wave dispersion relation with SpinW (see Fig. 4.2.3 (b)).
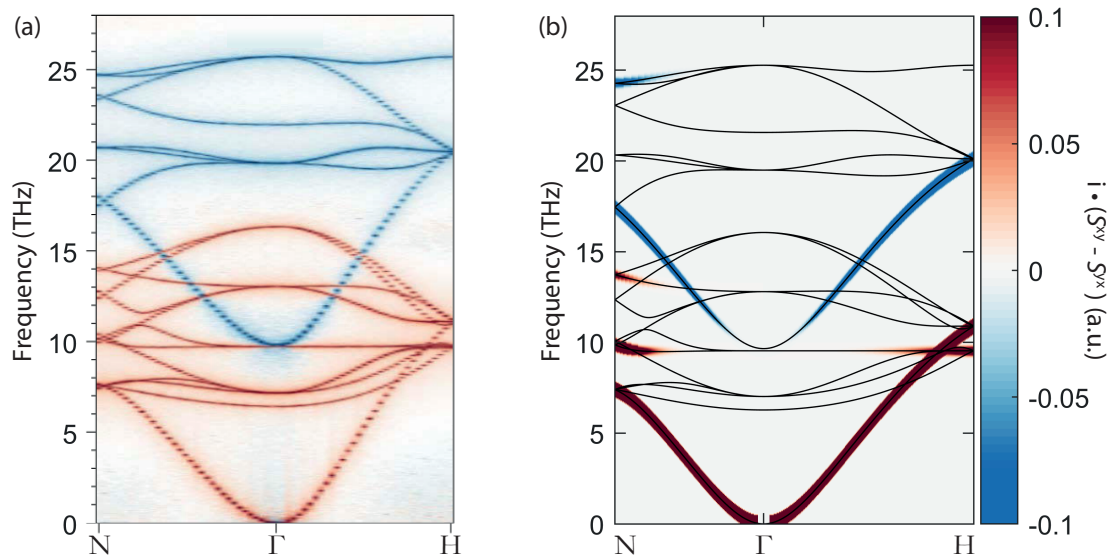
Figure 4.2.3.: (a) Spin wave dispersion relation of YIG for $T = 1\,\mathrm{K}$ calculated by J. Barker and G.E.W. Bauer. The authors calculated the antisymmetric transverse spectral function $\mathrm{i} \cdot (S^{xy}(\mathbf{q}, \omega) - S^{yx}(\mathbf{q}, \omega))$ as a function of frequency and the momentum in relative lattice units by using the local spin dynamics within a Landau-Lifshitz-Gilbert description. Figure taken from Ref. [15]. (b) Spin wave dispersion calculated by a SpinW simulation within this work. The coupling constants are taken from Ref. [15]. The primitive, rhombohedral unit cell of YIG is implemented in the SpinW-simulation to avoid artificial bands.

4.3. Simulation of the spin wave dispersion relation of $Gd_3Fe_5O_{12}$

The next step towards the simulation of magnon properties in $Tb_3Fe_5O_{12}$ is the simulation of the spin wave dispersion relation of $Gd_3Fe_5O_{12}$ (GdIG). GdIG exhibits only spin angular momenta and thus its spin wave dispersion relation can be ideally simulated with SpinW, which considers only spin angular momentum.

GdIG has a third magnetic sublattice, additional to the two magnetic Fe^{3+}-sublattices in YIG. The magnetic Gd^{3+}-ions with spin $S = 7/2$, which form the magnetic sublattice $\mathbf{M}_{Gdc}$ are located on the $24c$ sites within the Ia3d space group (see red atoms in Fig. 4.3.1 (a)). The intra-sublattice coupling of $\mathbf{M}_{Gdc}$ is neglected, since there are no valid reports on mag-

netic ordering of the Gd-sublattice at low temperatures. The inter-sublattice coupling to the two iron sublattices is considerably weak ($J_{\mathrm{dc}}/J_{\mathrm{ad}} = 0.29$; $J_{\mathrm{ac}}/J_{\mathrm{ad}} = 0.07$) [16]. Thus, the Gd^{3+}-moments can be described as 'exchange-enhanced' paramagnetic moments, which are oriented antiparallel to the total Fe-magnetization $\mathbf{M}_{\mathrm{Gdc}} \upuparrows \mathbf{M}_{\mathrm{Fe,tot}} = \mathbf{M}_{\mathrm{Fea}} + \mathbf{M}_{\mathrm{Fed}}$ (see red arrows in Fig. 4.3.1 (a)). A more detailed description of GdIG is given in section 2.4.2.
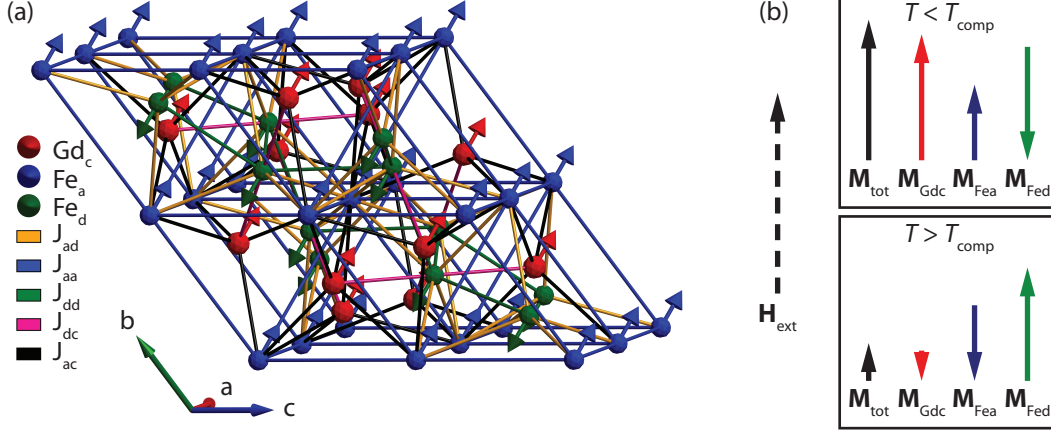
Figure 4.3.1.: (a) Primitive, rhombohedral unit cell of the bcc lattice of GdIG with $a_{\mathrm{GdIG,rh}} = 10.80\,\text{Å}$ and $\alpha_{\mathrm{GdIG,rh}} = 109.47°$ [16], containing 32 magnetic ions resulting in a maximum of 32 bands in the spin wave dispersion relation. The moments in this figure are aligned along the cubic $[111]_{\mathrm{bcc}}$ magnetic easy axis. (b) Schematic drawing of the orientation of the collinear sublattice magnetizations $\mathbf{M}_{\mathrm{Gd}}$, $\mathbf{M}_{\mathrm{Fea}}$, $\mathbf{M}_{\mathrm{Fed}}$ as well as the total magnetization $\mathbf{M}_{\mathrm{tot}}$ in a finite external magnetic field $\mathbf{H}_{\mathrm{ext}}$ in GdIG. In finite external magnetic fields, the sublattice magnetizations invert above the magnetic compensation temperature $T_{\mathrm{comp}} \approx 288\,\text{K}$ [40], where the total remanent magnetization vanishes ($M_{\mathrm{GdIG,tot}}(T_{\mathrm{comp}}) = 0$).

As input for the SpinW simulation, the exchange constants reported by Geprägs *et al.* are used (see Table 4.3.1) [16]. The spin wave dispersion relation calculated within this work using SpinW (see Fig. 4.3.2 (b)) is identical to the spin wave dispersion relation reported by Geprägs *et al.* (see Fig. 4.3.2 (a)) in the low temperature region $T = 40\,\text{K}$. In Ref. [16], the spin wave dispersion relation was calculated by using the local spin dynamics within a Landau-Lifshitz-Gilbert approach. The larger values of the coupling constants in comparison with those listed in Table 4.2.1 is based on the approach with normalized spins in Ref. [16].

Coupling constant	Coupling energy (meV)
J_{ad}	11.48
J_{aa}	2.29
J_{dd}	2.29
J_{dc}	3.41
J_{ac}	0.85

Table 4.3.1.: Coupling constants of GdIG used by Geprägs *et al.* to calculate the spin wave dispersion relation shown in Fig. 4.3.2 (a). For the calculation, the authors used the local spin dynamics within a Landau-Lifshitz-Gilbert description with normalized spins. By using these coupling constants together with normalized spins, an identical spin wave dispersion relation can be obtained by SpinW (see Fig. 4.3.2 (b)).

The key characteristics of the calculated spin wave dispersion relation of GdIG shown in Fig. 4.3.2 are the acoustic, so-called fundamental ferrimagnetic resonance band, which has a parabolic shape in the vicinity of the Γ-point and the two optical parabolic bands, colored in blue and red. The size of the energy gap of the first optical, blue mode, which is $E_{\text{gap}} \approx 6.5\,\text{meV}$ at $40\,\text{K}$, is strongly dependent on the exchange field acting on the total Fe-sublattice magnetization, which overall yields $E_{\text{gap}} \propto |\mathbf{M}_{\text{Gd}}|(J_{\text{dc}}|\mathbf{M}_{\text{Fed}}| - J_{\text{ac}}|\mathbf{M}_{\text{Fea}}|)$. In the lower energy region at $\approx 2.8\,\text{meV}$, on top of the acoustic band, there are furthermore several approximately dispersionless bands originating from the weakly coupled magnetic moments of the Gd^{3+}-ions precessing in the exchange field of the Fe^{3+}-sublattices.

In conclusion, Fig. 4.3.2 reveals that SpinW is a valid simulation tool for calculating the spin wave dispersion relation at low temperatures for complex materials with only spin angular momentum, e.g. GdIG.
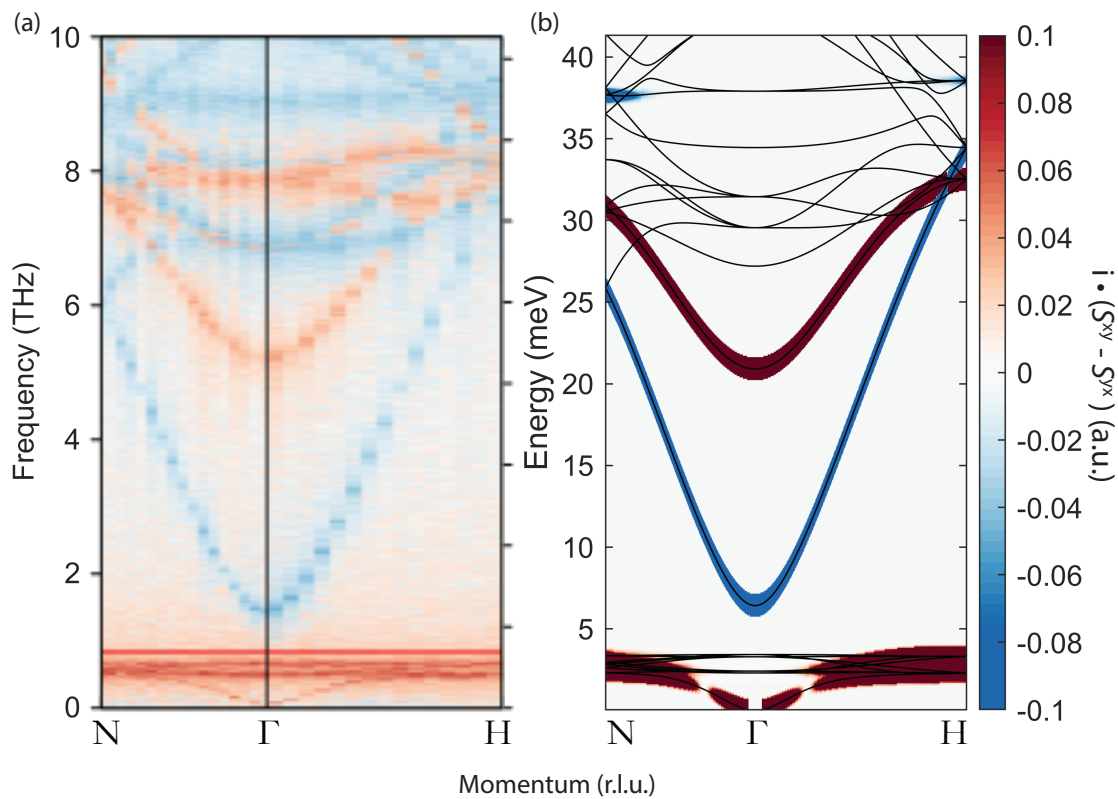
Figure 4.3.2.: (a) Spin wave dispersion relation of GdIG at $T = 40\,\text{K}$ reported by Geprägs and coworkers [16]. The calculation was carried out using local spin dynamics in a Landau-Lifshitz-Gilbert approach. The acoustic band is running up to $2.5\,\text{meV}$, where it is bound by the approximately dispersionless bands originating from the weakly coupled Gd^{3+}-moments. At higher energies around $6.5\,\text{meV}$, GdIG has a gapped, strongly dispersing optical band, which has opposite chirality (blue mode). Figure taken from Ref. [16]. (b) Spin wave dispersion relation calculated using SpinW within this work. With the exchange coupling constants from Geprägs *et al.* [16], the spin wave dispersion relation of figure (a) can be reproduced. This result confirms SpinW as a proper simulation tool for calculating spin wave dispersion relations at low temperatures.

4.4. Simulation of the spin wave dispersion relation of Tb$_3$Fe$_5$O$_{12}$

The next step after the successful simulation of the spin wave dispersion relation of YIG and GdIG is the simulation of the spin wave dispersion relation of Tb$_3$Fe$_5$O$_{12}$ (TbIG). TbIG increases the difficulty in terms of spin wave dynamics due to an additional orbital angular momentum on the $24c$ site within the cubic Ia3d space group. The goal of this section is to find a spin wave dispersion relation with one coupled set of parameters, that can explain the experimentally determined dispersion relation obtained by inelastic neutron scattering on a TbIG single crystal at $10\,\mathrm{K}$, $100\,\mathrm{K}$ and $280\,\mathrm{K}$ (see section 3). For the calculation of the spin wave dispersion relation at $100\,\mathrm{K}$ and $280\,\mathrm{K}$, several assumptions have to be made, since with SpinW only an approximation to magnon properties far away from the $0\,\mathrm{K}$-limit can be provided.
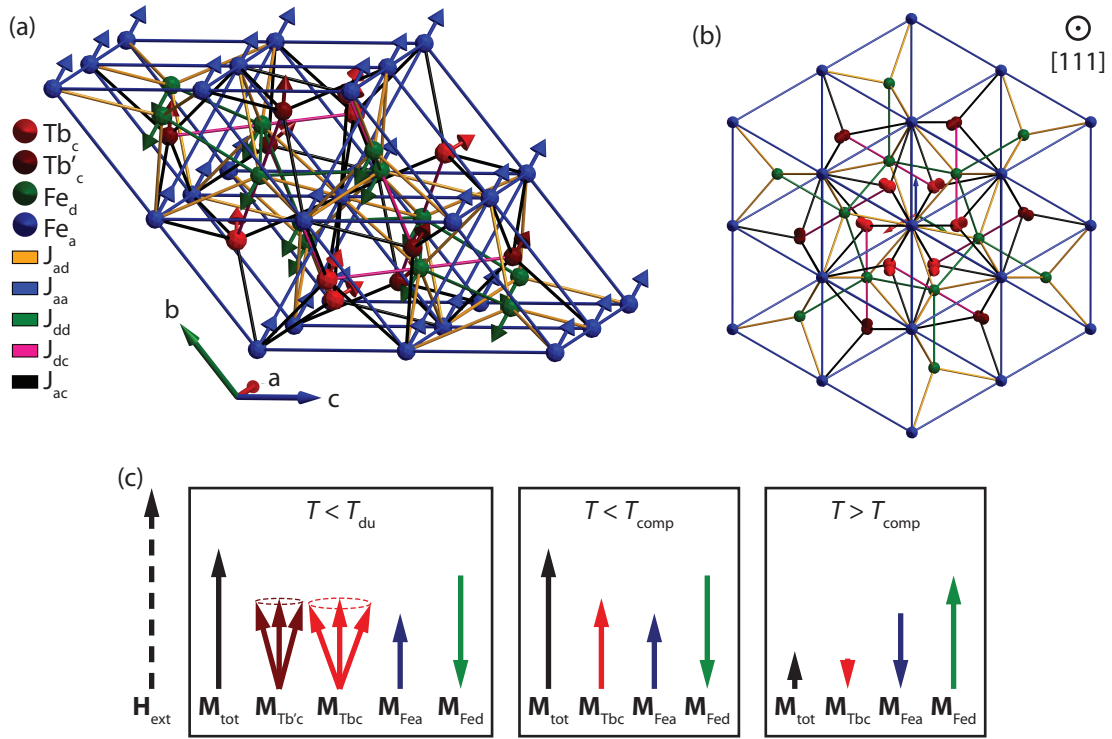
Figure 4.4.1.: (a) Magnetic atoms within the rhombohedrally distorted unit cell of TbIG using the values of the rhombohedral lattice constant $a_{\mathrm{TbIG,rh}}$ and angle $\alpha_{\mathrm{TbIG,rh}}$ as well as the opening angles of the 'double-umbrella' structure θ and θ' at $10\,\mathrm{K}$ (see Figs. 2.4.5 and 2.4.6). The arrows show the directions of the Fe$_d$ (green) and Fe$_a$ (blue) as well as of the non-equal Tb$_c$ (red) and Tb'$_c$ (dark red) magnetic moments. Furthermore, the exchange interaction between different sites (J_{ad}, J_{aa}, J_{dd}, J_{dc}, J_{ac}) are shown by colored lines. (b) Magnetic atoms within the primitive unit cell of TbIG. The crystallographic [111] direction is pointing out of the drawing plane, which makes the 'double-umbrella' structure visible. (c) Schematic drawing of the three different magnetic phases in TbIG. A small external field along the cubic [111]$_{\mathrm{bcc}}$-direction is considered. For $T < T_{\mathrm{du}} \approx 160\,\mathrm{K}$, TbIG is described by the double-umbrella structure which is defined by the two opening angles θ, θ'. Above the magnetic compensation temperature T_{comp}, the directions of the sublattice magnetizations are reversed to maintain a parallel orientation of the total magnetization $\mathbf{M}_{\mathrm{tot}}$ with the external magnetic field $\mathbf{H}_{\mathrm{ext}}$.

For $T > T_{\text{rh}} \approx 190\,\text{K}$, the properties of TbIG are similiar to GdIG [31]. Below $T < T_{\text{rh}}$, TbIG shows a rhombohedral distortion, thus its space group changes to R$\bar{3}$ (see section 2.4.3). The degeneracy of the $24c$-sites within the Ia3d space group is lifted to non-degenerate $6e$- and $6e'$-sites within the R$\bar{3}$ space group and the collinear magnetic structure is replaced by the 'double-umbrella' structure [33] (see Fig. 4.4.1). This structure is defined by the two opening angles θ, θ', which describe the tilting of the magnetic moments of Tb^{3+}-ions and Tb$^{3+'}$-ions on the $6e$- and $6e'$- sites, respectively. Within the double umbrella structure, the magnetic moments of Tb^{3+} and Tb$^{3+'}$ tilt away from the cubic $[111]_{\text{bcc}}$-direction within the three degenerated $[111]_{\text{bcc}} \times [100]_{\text{bcc}}$ planes. A more detailed description of the properties of TbIG is given in section 2.4.3.

Coupling constant	Coupling energy (meV)
J_{ad}	5.51
J_{aa}	1.10
J_{dd}	1.10
J_{dc}	1.17
J_{ac}	0.29

Table 4.4.1.: Coupling constants used for the simulation of the spin wave dispersion relation in GdIG. Due to the transition to unnormalized spins, the coupling constants differ from the coupling constants displayed in Table 4.3.1, such that they yield the same spin wave dispersion relation but with unnormalized spins. These coupling constants are used as a starting point for the simulation of the spin wave dispersion relation of TbIG for $T = 280\,\text{K}$, above the temperature of the structural distortion $T_{\text{rh}} \approx 190\,\text{K}$.

As a starting point for the simulation, the coupling constants found for the simulation of GdIG (see Table 4.4.1) are used. As TbIG exhibits an additional orbital angular momentum, a pseudo-spin angular momentum of the Tb^{3+}-ions is used, which is determined from temperature dependent magnetization measurements $M(T)$, obtained by SQUID-magnetometry (see Fig. 4.4.2 (a)). For this purpose, the $M(T)$-measurement with an external applied magnetic field of $1\,\text{T}$ along the cubic $[111]_{\text{bcc}}$-direction of a YIG single crystal is added (subtracted) to (from) that of a TbIG single crystal below (above) the magnetic compensation temperature $T_{\text{comp}} = 250.5\,\text{K}$ of TbIG. With this method, the magnetization of the Tb^{3+}-ions $\parallel [111]_{\text{bcc}}$ is determined, assuming that the Y^{3+}-ions of YIG are non-magnetic. The magnetization of the Tb^{3+}-ions is corrected by a factor $1/\cos(\theta)$ and $1/\cos(\theta')$ for the $6e$ and $6e'$ sites, respectively, within the 'double-umbrella' phase using the opening angles θ and θ' determined from neutron diffraction by Lahoubi [33]. By the assumption of $g_{\text{Tb}} = 2$, the quasi-spin S_{Tb} of the Tb^{3+}-ions describing the sum of the spin angular momentum and the orbital angular momentum is calculated, which is used as input for the SpinW simulation. This method is needed, since SpinW does not allow an orbital angular momentum and thus the quasi-spin assumption is the only possibility to describe a magnetic ion that possesses an additional orbital angular momentum with SpinW. Due to Tb being a heavy element this assumption is valid since $j = l + s$ is the only good quantum number describing the total angular momentum of the electron in the strong spin-orbit coupling regime. Here, j is used as a quasi-spin where the size of the spin, whose absolute value is extracted from a $M(T)$ measurement, is the main source for

the implementation of the temperature dependence.

For further reduction of the parameter space, only the two Fe-Tb exchange coupling constants J_{dc} and J_{ac} as well as a factor which is multiplied to all Fe-Fe exchange coupling constants J_{ad}, J_{aa}, J_{dd}, which is called 'Fe-factor' in the following, are considered as free parameters. The physical argument behind this assumption is given by the rigidity of the magnetic Fe-subsystems for all rare-earth iron garnets $RE_3Fe_5O_{12}$, which also leads to a similar Néel temperature $T_N \approx 550\,K$ for all known RE^{3+}-ions (see Fig. 2.4.2). Thus, the free parameters for the refinement of the spin wave dispersion relation to get the best possible agreement to the experimental data obtained by inelastic neutron scattering on a TbIG single crystal are the 'Fe-factor' and the two Fe-Tb exchange couplings J_{dc} and J_{ac}.
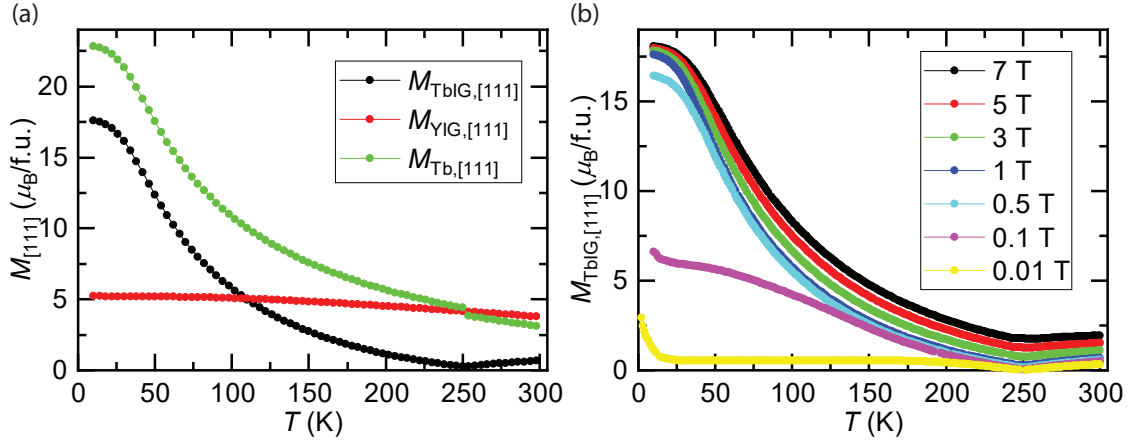
Figure 4.4.2.: Temperature dependent magnetization measurements $M(T)$ obtained by SQUID-magnetometry (see section A.2.2) with an external magnetic field applied parallel to the cubic $[111]_{bcc}$-direction. The magnetization is given in Bohr magnetons per formula unit of $Tb_3Fe_5O_{12}$ (μ_B/f.u.). (a) Magnetizations $M_{YIG,[111]}$ and $M_{TbIG,[111]}$ parallel to the cubic $[111]_{bcc}$-direction of a YIG single crystal and a TbIG single crystal, respectively, in an external magnetic field of $\mu_0 H_{ext} = 1\,T$. For the determination of the Tb^{3+}-sublattice magnetization $M_{Tb,[111]}$ the $M(T)$-measurements for YIG and TbIG are subtracted (added) for temperatures above (below) the magnetic compensation temperature $T_{comp,TbIG} = 250.5\,K$. The discontinuity in $M_{Tb,[111]}(T)$ at T_{comp} can be traced back on a finite $\partial_{H_{ext}} M(T_{comp}, H_{ext})$ and would vanish in the $0\,T$-limit. (b) $M(T)$-measurements of a TbIG single crystal in several external magnetic fields. Below $100\,K$, the magnetization shows a rapid increase up to $17.6\,\mu_B$ per formula unit at $10\,K$ for external magnetic fields larger than $0.5\,T$. As expected, the dependence of the magnetization on the external magnetic field $\partial_{H_{ext}} M(T, H_{ext})$ is increasing with rising temperatures, resulting from the suppression of thermal excitations by an external magnetic field. A spin-canting phase [29] is found for external magnetic fields above $3\,T$ in a small temperature region in the vicinity of T_{comp}.

4.4.1. Spin wave dispersion relation of $Tb_3Fe_5O_{12}$ at 280 K

The discussion of the spin wave dispersion relation of TbIG starts at high temperatures ($T = 280\,K$), where the material properties of TbIG are similar to GdIG. This implies that at $280\,K$ TbIG does not show a rhombohedral distortion and the sublattice magnetizations are aligned collinear. Thus, the SpinW-simulation which was set up for GdIG can be used as a starting point. The quasi-spin for the Tb^{3+}-ion is found as $S_{Tb} = 0.564\,\hbar$ at $280\,K$ (see Fig. 4.4.2 (a)).

In Fig. 4.4.3, the data points obtained by inelastic neutron scattering with polarization analysis on a TbIG single crystal at a sample temperature of $280\,\mathrm{K}$ (see Fig. 3.2.1 (b)) are plotted together with the simulated spin wave dispersion relation (see Fig. 4.4.3). The color of the data points depicts the experimentally determined chirality of the respective magnon mode, i.e. the sign of $\mathrm{i} \cdot (S^{xy} - S^{yx})$.
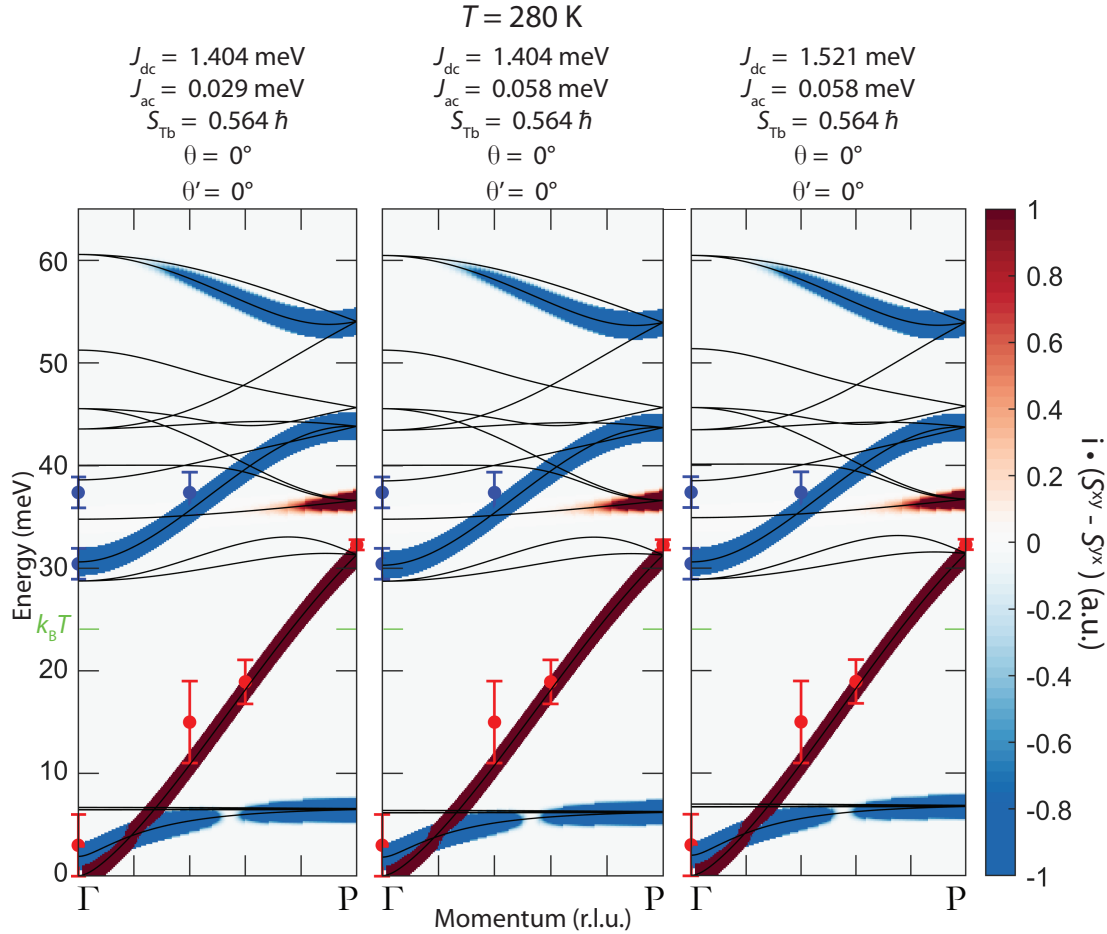
Figure 4.4.3.: Three examples of spin wave dispersion relations of TbIG at $280\,\mathrm{K}$ simulated with SpinW. The simulation parameters are shown on top. The data points plotted together with the simulation are obtained by inelastic neutron scattering with polarization analysis (see Fig. 3.2.1 (b)). The three simulations are able to reproduce the experimental data such that the simulated magnon modes are within the error bars of the extracted energy positions of the magnon modes found by the inelastic neutron scattering experiment. The thermal energy is marked in green. Spin wave modes up to this energy are thermally excited and contributing to thermally activated spin currents in e.g. spin Seebeck effect experiments. Remarkably, the first optical mode at temperatures below $T_{\mathrm{comp}} = 250.5\,\mathrm{K}$ becomes the acoustic mode for temperatures above T_{comp} (red dispersing mode below $30\,\mathrm{meV}$), whereas the previous acoustic mode is found to have an energy gap at the Γ point (blue dispersing mode below $8\,\mathrm{meV}$). This behavior is consistent with simulations of GdIG above T_{comp} reported by Ganzhorn *et al.* [12].

To refine the simulated spin wave dispersion relation, the free parameters are varied until the spin wave dispersion relation matches the experimental data points. It turns out that the Fe^{3+} exchange couplings $J_{\mathrm{ad}}, J_{\mathrm{aa}}, J_{\mathrm{dd}}$ remain unchanged and thus are equal to the Fe^{3+} exchange couplings found for GdIG. This is true for the whole temperature region inves-

tigated in this work. The three best matching results with respect to the remaining free parameters which are the exchange couplings between the Tb^{3+}-moments and the Fe^{3+}-moments, i.e. the J_{dc} and J_{ac} exchange constant, are shown in Fig. 4.4.3. From these simulations, the parameters with their respective uncertainties are determined (see Table 4.4.2).

Simulation parameter	Fitted values	Simulation parameter	Fixed value
J_{ac}	$(0.039 \pm 0.015)\,\text{meV}$	S_{Tb}	$0.564\,\hbar$
J_{dc}	$(1.52 \pm 0.12)\,\text{meV}$	θ	$0°$
J_{ad}	$(5.51 \pm 0.11)\,\text{meV}$	θ'	$0°$
J_{aa}	$(1.10 \pm 0.02)\,\text{meV}$	a_{rh}	$10.767\,\text{Å}$
J_{dd}	$(1.10 \pm 0.02)\,\text{meV}$	α_{rh}	$109.47°$

Table 4.4.2.: Simulation parameters obtained by refining the spin wave dispersion relation simulated by SpinW to experimental data obtained by inelastic neutron scattering with polarization analysis at a sample temperature of $280\,\text{K}$ (see Fig. 4.4.3). The error is calculated form the entity of spin wave dispersion relations which match the experimental data within the error bars. The fixed simulation parameters on the right are obtained from SQUID-magnetometry measurements (S_{Tb}) and from Ref. [23] (a_{rh}, α_{rh}) and Ref. [33] (θ, θ'), respectively. For the simulation, the primitive, rhombohedral unit cell of the bcc symmetry with the respective rhombohedral lattice constant a_{rh} and angle α_{rh} is used.

For the discussion of the SpinW-simulation for TbIG shown in Fig. 4.4.3, it is compared to the spin wave dispersion relation of GdIG at $T = 40\,\text{K}$ (see Fig. 4.3.2). This is a valid comparison, since the macroscopic material properties of TbIG at $280\,\text{K}$ and GdIG are similar with an identical crystal structure and space-group.

For the simulation of TbIG at $280\,\text{K}$, i.e. above the magnetic compensation temperature T_{comp}, the chirality (depicted by the coloring) of all bands is inverted relatively to the spin wave dispersion relation of GdIG at $40\,\text{K}$, i.e. below T_{comp}. When crossing the magnetic compensation temperature T_{comp} in finite magnetic fields, the total magnetization remains aligned parallel to the external magnetic field ($\mathbf{M}_{tot} \upuparrows \mathbf{H}_{ext} \upuparrows +\hat{\mathbf{z}}$), whereas the orientation of the sublattice magnetizations is inverted (see Fig. 4.4.1 (c)). Since the chirality of a spin wave is depending on the orientation of the magnetic moments, the inversion of all sublattices causes an inversion of the chirality.

The most remarkable property of the spin wave dispersion relation of TbIG at $280\,\text{K}$ is the acoustic, red mode below $30\,\text{meV}$, which is related to the first optical, blue mode of GdIG at $40\,\text{K}$ shown in Fig. 4.3.2. Furthermore, the first optical, blue mode below $6.5\,\text{meV}$ is related to the acoustic mode of GdIG at $40\,\text{K}$. Physically, this interchange of the acoustic and the first optical mode is related to the acoustic mode describing the precession of the local moments from all sublattices in phase, leading to a magnetic moment of the magnon antiparallel to the total magnetization, which is equal to $i \cdot (S^{xy} - S^{yx}) > 0$ (red) in the wave picture. To satisfy this constraint, the acoustic mode and the first optical mode switch roles while crossing T_{comp}. This was also found for the spin wave dispersion relation in GdIG by Ganzhorn *et al.* [12]. Additionally, Ganzhorn *et al.* found that the temperature and field dependence of the band position in GdIG are strongly linked to the acoustic and optical character of the band. This results in an interchange of the susceptibility of the two bands on temperature and field changes, which might also be true for TbIG due to the resem-

blance to GdIG at $T > T_{rh} \approx 190\,\mathrm{K}$. Further intuitive interpretation of the bands in the spin wave dispersion relation of TbIG is similar to GdIG, which is given in section 4.3.

4.4.2. Spin wave dispersion relation of Tb$_3$Fe$_5$O$_{12}$ at 100 K

After the successful simulation of the spin wave dispersion relation of TbIG at $280\,\mathrm{K}$, where the material properties are comparable to the well known GdIG, the next step is the simulation of the spin wave dispersion relation of TbIG at $100\,\mathrm{K}$. Below $T_{rh} \approx 190\,\mathrm{K}$, TbIG exhibits a structural distortion resulting in the rhombohedral R$\bar{3}$ structure. Despite the small rhombohedral distortion, pointed out by the small difference of $0.03°$ of the rhombohedral angle relative to that of the non-distorted primitive rhombohedral unit cell of the bcc-lattice, a 'double-umbrella' structure on the non-equal $6e$- and $6e'$-sites within the R$\bar{3}$ structure is present for $T < T_{du}$ (see section 2.4.3). For the quasi-spin, a value of $S_{Tb} = 1.86\,\hbar$ is obtained by $M(T)$-SQUID-magnetometry measurements (see Fig. 4.4.2). This is taken into account by using a non-collinear magnetic structure as input of the SpinW-simulation (see Fig. 4.4.1 (b)). As mentioned earlier, the opening angles θ and θ' of the double umbrella structure found by neutron diffraction experiments reported by Lahoubi [33] are used as fixed simulation parameters.

Analogously to the simulation of the spin wave dispersion relation for $280\,\mathrm{K}$, the data points obtained by inelastic neutron scattering with polarization analysis at a sample temperature of $100\,\mathrm{K}$ (see Fig. 3.3.1) are plotted together with the simulation results in Fig. 4.4.4. The simulation is refined to the neutron scattering data by optimizing the exchange interactions J_{ac}, J_{dc} and the 'Fe-factor' defined in section 4.4, which is adjusting the Fe-Fe interactions. As an example, three SpinW-simulations, which agree with the results of the inelastic neutron scattering experiment within the error range, are shown in Fig. 4.4.4. From all the exchange interactions, which result in spin wave dispersion relations reproducing the experimental data of the inelastic neutron scattering within the error range, the final material parameters as well as the corresponding uncertainties are calculated (see Table 4.4.3).

The spin wave dispersion relation of TbIG at $100\,\mathrm{K}$ mimics the spin wave dispersion relation of GdIG at $40\,\mathrm{K}$ (see Fig. 4.3.2). Due to the higher temperature and thus lower Tb-sublattice magnetization, the energy gap at the Γ-point of the first optical, blue mode $E_{gap} = 4.5\,\mathrm{meV}$ is smaller than in GdIG at $40\,\mathrm{K}$.

Compared to the spin wave dispersion relation of TbIG at $280\,\mathrm{K}$ (see Fig. 4.4.3), the first optical mode (here in blue) and the acoustic mode (here in red) have swapped their key properties, which in the first place results in the acoustic mode being a non-gapped mode at the Γ-point in the absence of an external magnetic field. Additionally, the colors of all magnon modes, i.e. $i \cdot (S^{xy} - S^{yx})$, are inverted compared to the spin wave dispersion relation of TbIG at $280\,\mathrm{K}$. Both findings can be explained by the crossing of the magnetic compensation temperature $T_{comp} = 250.5\,\mathrm{K}$ where the sublattice magnetizations invert within a finite external magnetic field.

The splitting of the first optical, blue mode found by inelastic neutron scattering (c.f. two blue data points at $4.6\,\mathrm{meV}$ and $6.8\,\mathrm{meV}$ at the Γ-point) is attributed to the coupling of the magnon to ligand field excitations resulting in two gapped hybrid modes and thus can-

not be simulated with SpinW (see Fig. 2.4.7) [34]. Most remarkable is the small, blue area within the acoustic band in close vicinity of the Γ-point at $E \approx 0\,\text{meV}$, which is indicating a mixed chirality of the acoustic band. This can be traced back to the opening of the 'double-umbrella' structure within TbIG below $T_{\text{du}} \approx 160\,\text{K}$.
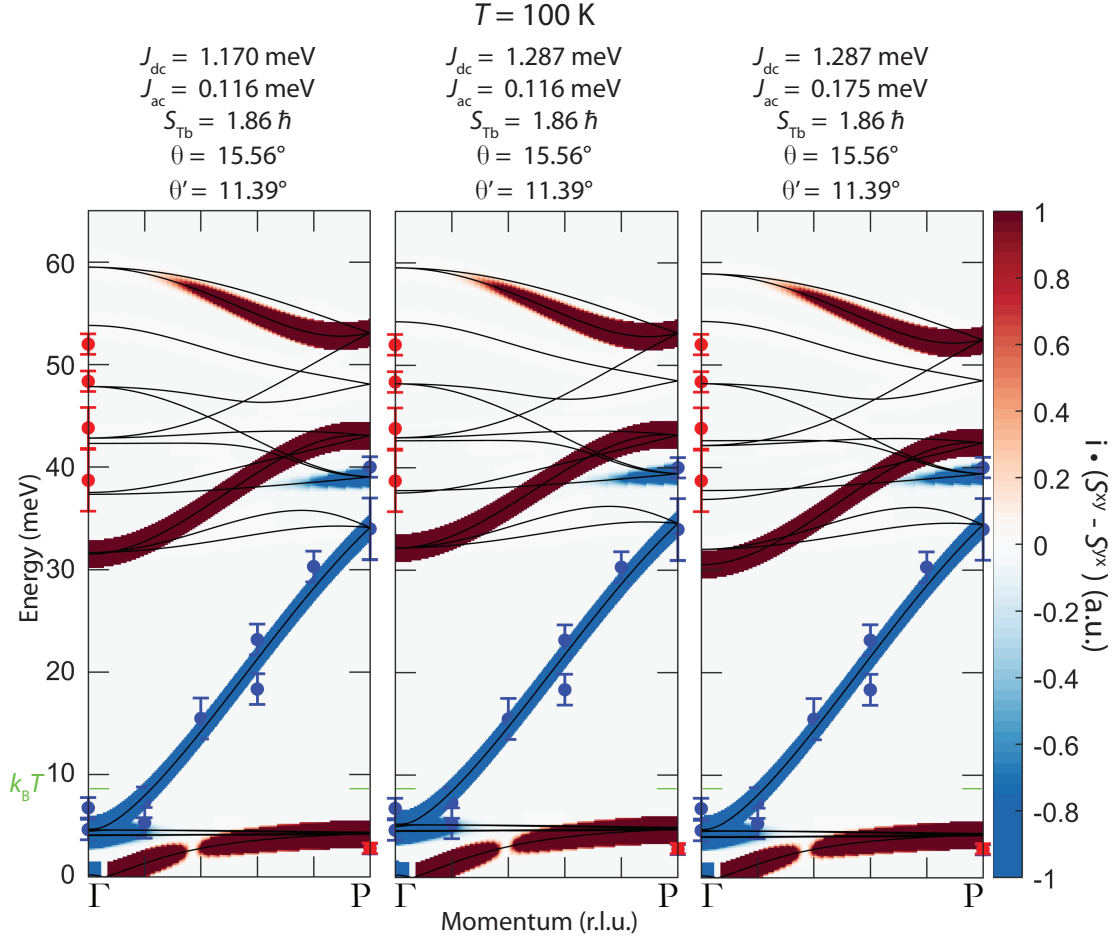
Figure 4.4.4.: Three examples of spin wave dispersion relations of TbIG at $100\,\text{K}$. The spin wave dispersion relations are obtained by adjusting the interaction between the Tb^{3+}- and the Fe^{3+}-ions as well as the Fe-Fe interactions, such that the simulated spin wave dispersion relation matches the data of inelastic neutron scattering with polarization analysis within the error range (red and blue data points). Spin wave modes are excited up to the thermal energy, marked in green, leading to contributions of all modes up to thermal energy to thermally driven spin currents under the constraints of the Bose-Einstein distribution. All of the three simulation results can fit the experimental data leading to an error range of the fitted parameters listed in Table 4.4.3.

Simulation parameter	Fitted values	Simulation parameter	Fixed value
J_{ac}	$(0.12 \pm 0.04)\,\text{meV}$	S_{Tb}	$1.86\,\hbar$
J_{dc}	$(1.17 \pm 0.13)\,\text{meV}$	θ	$15.56°$
J_{ad}	$(5.51 \pm 0.11)\,\text{meV}$	θ'	$11.39°$
J_{aa}	$(1.10 \pm 0.02)\,\text{meV}$	a_{rh}	$10.753\,\text{Å}$
J_{dd}	$(1.10 \pm 0.02)\,\text{meV}$	α_{rh}	$109.44°$

Table 4.4.3.: Simulation parameters obtained by refining the spin wave dispersion relation simulated by SpinW to experimental data obtained by inelastic neutron scattering with polarization analysis at a sample temperature of $100\,\text{K}$ (see Fig. 4.4.4). The error is calculated form the entity of spin wave dispersion relations which match the experimental data within the error bars. The fixed simulation parameters on the right are obtained from SQUID-magnetometry measurements (S_{Tb}) and from Ref. [23] (a_{rh}, α_{rh}) and Ref. [33] (θ, θ'), respectively.

4.4.3. Spin wave dispersion relation of Tb$_3$Fe$_5$O$_{12}$ at 10 K

The last step towards the full simulation of the spin wave dispersion relation of TbIG is the investigation of the low temperature regime, which is covered by the simulation of the spin wave dispersion relation at $T = 10\,\text{K}$ within this work. At very low temperatures, the rhombohedral distortion is still small $\Delta\alpha_{rh,280K-10K} = 0.06°$, where $\alpha_{rh,280K} = 109.47°$ is the rhombohedral angle of the non-distorted primitive bcc unit cell. On the other hand, the opening angles of the double umbrella structure with $\theta = 31.37°$ and $\theta' = 26.46°$ [33] are large, leading to drastic changes in the spin wave dispersion relation. Also the quasi-spin of the Tb-moments is considerably large ($S_{Tb} = 4.35\,\hbar$) which results in a high total magnetization $|\mathbf{M}_{tot}| = 17.6\,\mu_B/\text{f.u.}$ of TbIG (see Fig. 4.4.2).

The procedure of refining the simulated spin wave dispersion relation to the data of inelastic neutron scattering with polarization analysis at a sample temperature of $10\,\text{K}$ remains identical to that previously described. The results of the SpinW-simulation of the spin wave dispersion relation of TbIG at $10\,\text{K}$ for three different sets of input parameters are shown in Fig. 4.4.5 together with the experimental data obtained by inelastic neutron scattering. The final simulation parameters and the corresponding uncertainties (see Table 4.4.4) are obtained by evaluating the entity of simulated spin wave dispersion relations matching the experimental data of the inelastic neutron scattering within the error range.

The spin wave dispersion relation of TbIG at $10\,\text{K}$ shows, as expected, a larger energy gap at the Γ-point of the first optical, blue mode of $E_{gap} = 9.1\,\text{meV}$ compared to that at $100\,\text{K}$. This is related to the large Tb-sublattice magnetization $|\mathbf{M}_{Tb}|(10\,\text{K}) = 22.8\,\mu_B/\text{f.u.}$ (see Fig. 4.4.2 (a)). Same as for the spin wave dispersion relation at $100\,\text{K}$, the splitting of the first optical, blue mode at the Γ-point found by inelastic neutron scattering is related to the coupling of the magnons to ligand field excitations leading to two hybrid modes at the Γ-point [34] (see two blue data points at $9.7\,\text{meV}$ and $12.7\,\text{meV}$ in Fig. 4.4.5).

Due to the even larger opening of the 'double-umbrella' at $10\,\text{K}$ than at $100\,\text{K}$, the blue area in the vicinity of the Γ-point increased its size which means that the acoustic band shows a pronounced mixed chirality, same as the flat bands above the acoustic band. These flat bands are related to the Tb-moments precessing in the exchange field of the two Fe-sublattices which is supporting the theory that the mixed chirality is originating from the canted Tb^{3+}-moments of the magnetic double umbrella structure. The most remarkable

feature is that all bands of the spin wave dispersion relation are gapped at the Γ-point. At $q \approx 0.2 \cdot$P, the acoustic band goes towards $E = 0\,\mathrm{meV}$. This behavior is also linked to the canting of the Tb-moments within the pronounced magnetic 'double-umbrella' structure of TbIG at low temperatures. Furthermore, there are two flat, chiral bands at around $12\,\mathrm{meV}$ and at $30\,\mathrm{meV}$ which were found by inelastic neutron scattering with polarization analysis but could not be reproduced by a SpinW simulation. The physical origin of these bands is still unclear but is supposed to be linked with the 'double-umbrella' structure or by a possible ordering of the Tb-moments at low temperature. However, this should be subject to further investigation. Since these flat bands were only found at $10\,\mathrm{K}$ within this work, their temperature evolution should be tracked within future inelastic neutron scattering experiments on TbIG, which could give new approaches to their physical origin.
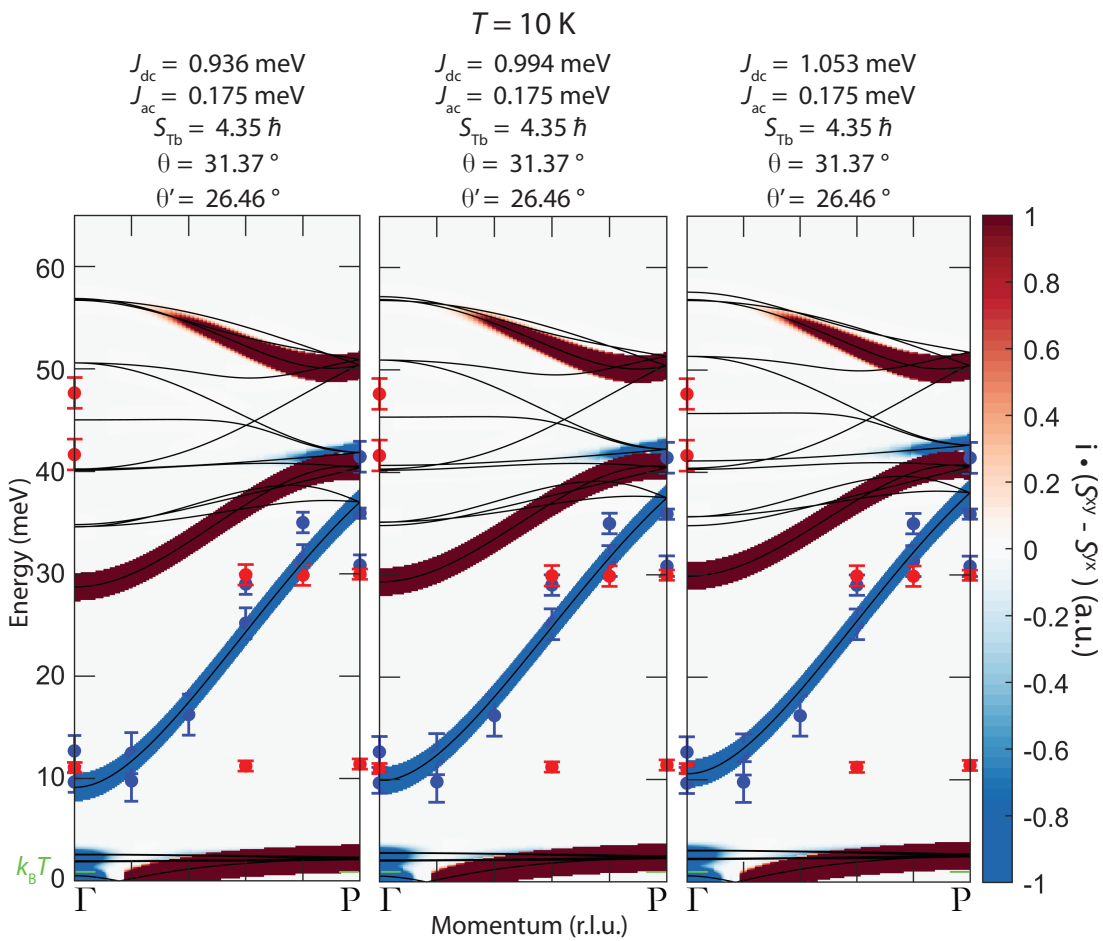
Figure 4.4.5.: Three examples of spin wave dispersion relations of TbIG at $10\,\mathrm{K}$ obtained by refining the dispersion relation to experimental data of inelastic neutron scattering with polarization analysis (red and blue data points). The flat bands at $12\,\mathrm{meV}$ and $30\,\mathrm{meV}$ found by inelastic neutron scattering cannot be reproduced by a SpinW simulation but are presumably originating from the pronounced double-umbrella structure or might be caused by an ordering of the Tb-sublattice moments, which is not implemented in this simulation. At $10\,\mathrm{K}$, the thermal energy (marked in green) is located within the acoustic band of the spin wave dispersion relation. This results in only the acoustic spin wave excitations (i.e. magnons) contributing to thermally activated spin currents in the low temperature regime.

Simulation parameter	Fitted values	Simulation parameter	Fixed value
J_{ac}	$(0.17 \pm 0.02)\,\text{meV}$	S_{Tb}	$4.35\,\hbar$
J_{dc}	$(0.99 \pm 0.06)\,\text{meV}$	θ	$31.37°$
J_{ad}	$(5.51 \pm 0.11)\,\text{meV}$	θ'	$26.46°$
J_{aa}	$(1.10 \pm 0.02)\,\text{meV}$	a_{rh}	$10.744\,\text{Å}$
J_{dd}	$(1.10 \pm 0.02)\,\text{meV}$	α_{rh}	$109.41°$

Table 4.4.4.: Simulation parameters obtained by refining the spin wave dispersion relation simulated by SpinW to experimental data obtained by inelastic neutron scattering with polarization analysis at a sample temperature of $10\,\text{K}$ (see Fig. 4.4.5). The error is calculated form the entity of spin wave dispersion relations which match the experimental data within the error bars. The fixed simulation parameters on the right are obtained from SQUID-magnetometry measurements (S_{Tb}) and from Ref. [23] (a_{rh}, α_{rh}) and Ref. [33] (θ, θ'), respectively.

4.4.4. Magnon properties in $Tb_3Fe_5O_{12}$ between 10 K and 100 K

Another interesting property, which can be extracted from the SpinW simulations of TbIG is the temperature T_{cross}, where the thermal energy (green line) crosses the first optical, blue mode at the Γ-point ($E_{gap}(T_{cross}) = k_B T_{cross}$). Slightly above this temperature the first optical, blue mode is populated according to Bose-Einstein statistics leading to a second thermal spin current channel when a temperature gradient is applied (see section 2.3.2). Since the chirality of the optical mode is opposite to the chirality of the already populated acoustic mode, the spin current channel originating from the optical mode cancels out the spin angular momentum which is transported by the channel originating from the acoustic mode, when a temperature gradient is applied. In total, this leads to a vanishing thermally activated spin current parallel to the temperature gradient. Within the spin Seebeck effect, this leads to a sign change in the total amplitude which is expected in the vicinity of the crossing temperature T_{cross}.

There are two attributes contributing to the value of T_{cross}. One is the position of the temperature itself. The other one is the size of the energy gap $E_{gap} \propto |\mathbf{M}_{Tb}|(J_{dc}|\mathbf{M}_{Fed}| - J_{ac}|\mathbf{M}_{Fea}|)$ at the Γ-point of the first optical mode, which is mainly influenced by the strong temperature dependence of Tb-sublattice magnetization $\mathbf{M}_{Tb}$. Since $\mathbf{M}_{Tb}$ is rapidly decreasing for $25\,\text{K} < T < 100\,\text{K}$ and E_{gap} is dependent on multiple parameters, the crossing temperature T_{cross} can only be extracted from a simulation in close vicinity of T_{cross}.

The spin wave dispersion relations for temperatures between $10\,\text{K}$ and $100\,\text{K}$ are shown in Fig. 4.4.6. As a first order approximation, the values of the magnetic exchange coupling constants are linearly interpolated between $10\,\text{K}$ and $100\,\text{K}$. The temperature dependent quasi-spin value for the magnetic moments of the Tb^{3+}-ions has been extracted from temperature dependent SQUID-magnetometry measurements on TbIG (see Fig. 4.4.2 (a)) and the opening angle is taken from the values found by Lahoubi (see Fig. 2.4.6)[33]. This is leading to $T_{cross} = 70\,\text{K}$, where also a sign change in the amplitude of the spin Seebeck effect is expected.
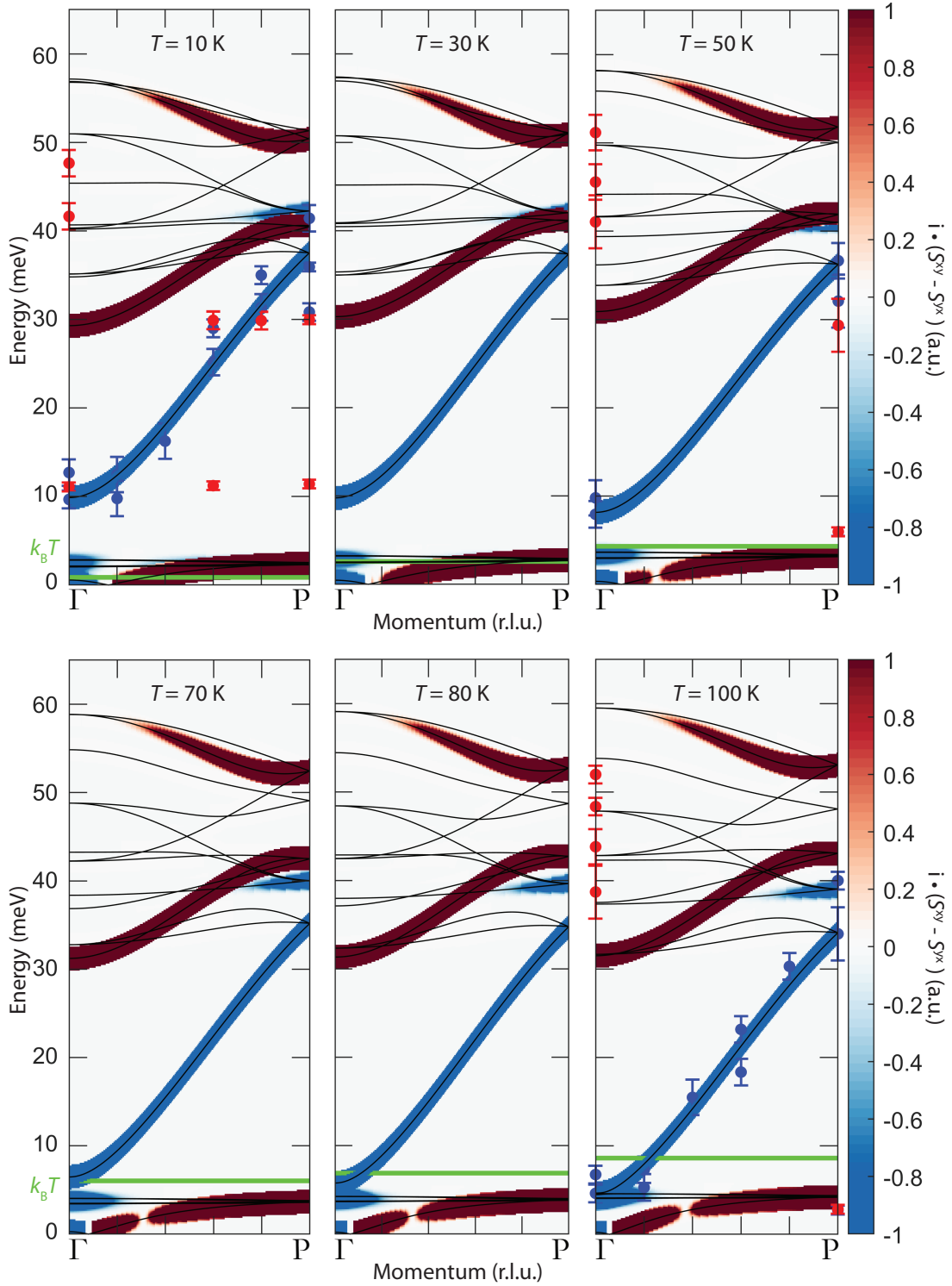
Figure 4.4.6.: Spin wave dispersion relations for $10\,\text{K} < T < 100\,\text{K}$ obtained by SpinW-simulations. For the simulation of the temperature evolution, the exchange coupling constants are linearly interpolated between $10\,\text{K}$ and $100\,\text{K}$. All recorded data points obtained by inelastic neutron scattering are plotted together with the results of SpinW-simulations. At the temperature $T_{\text{cross}} = 70\,\text{K}$, the thermal energy (green horizontal line) crosses the first optical, blue mode at the Γ-point.

4.5. Summary - Simulation of the spin wave dispersion relation of $Tb_3Fe_5O_{12}$ with SpinW

This chapter discussed the SpinW-simulations of the spin wave dispersion relation of YIG, GdIG and TbIG. The comparison of the simulated spin wave dispersion relations of YIG and GdIG with literature data demonstrates the validity of SpinW for the simulation of spin wave dispersion relations of complex rare-earth iron garnet materials.

The SpinW-simulations of TbIG for $10\,\text{K}$, $100\,\text{K}$ and $280\,\text{K}$ match the data obtained by inelastic neutron scattering with polarization analysis. The choice of temperatures covers all structural and magnetic phases of TbIG and leads to simulations which are able to outline the magnon properties (i.e. spin wave dispersion relations) in the magnetically ordered phases of TbIG. The obtained spin wave dispersion relations are set in context with the temperature profile of the spin Seebeck effect in the next chapter.

The second important result is a full set of exchange interaction constants, which is listed in Table 4.5.1. Furthermore, the temperature where the thermal energy crosses the first optical mode at the Γ-point is determined as $T_{\text{cross}} = 70\,\text{K}$. This temperature is connected to the low temperature sign change of the spin Seebeck effect amplitude within the next chapter.

Simulation parameter	Fitted values ($10\,\text{K}$)	Fitted values ($100\,\text{K}$)	Fitted values ($280\,\text{K}$)
J_{ac}	$(0.17 \pm 0.02)\,\text{meV}$	$(0.12 \pm 0.04)\,\text{meV}$	$(0.039 \pm 0.015)\,\text{meV}$
J_{dc}	$(0.99 \pm 0.06)\,\text{meV}$	$(1.17 \pm 0.13)\,\text{meV}$	$(1.52 \pm 0.12)\,\text{meV}$
J_{ad}	$(5.51 \pm 0.11)\,\text{meV}$	$(5.51 \pm 0.11)\,\text{meV}$	$(5.51 \pm 0.11)\,\text{meV}$
J_{aa}	$(1.10 \pm 0.02)\,\text{meV}$	$(1.10 \pm 0.02)\,\text{meV}$	$(1.10 \pm 0.02)\,\text{meV}$
J_{dd}	$(1.10 \pm 0.02)\,\text{meV}$	$(1.10 \pm 0.02)\,\text{meV}$	$(1.10 \pm 0.02)\,\text{meV}$

Table 4.5.1.: Parameters resulting from refining the spin wave dispersion relation to experimental data obtained by inelastic neutron scattering. Together with the data plotted in Figs. 2.4.5, 2.4.6 and 4.4.2 this gives a full set of parameters describing the magnetic interaction in TbIG. Remarkably, the Fe-Fe exchanges (J_{ad}, J_{aa}, J_{dd}) are constant within the considered temperature region, which is typical for the rare-earth iron garnet material class.

5. Spin Seebeck effect in $Tb_3Fe_5O_{12}|Pt$ heterostructures

This chapter discusses the spin Seebeck effect experiments with $Tb_3Fe_5O_{12}$ | Pt heterostructures. The first part of this chapter describes the experimental setup and the data analysis for the extraction of the spin Seebeck signal. The main part then focuses on the spin Seebeck effect in the $Tb_3Fe_5O_{12}$ single crystal | Pt heterostructures and its connection to the spin wave dispersion relation of $Tb_3Fe_5O_{12}$ discussed in the previous chapter. Subsequently, the third section discusses the spin Seebeck effect in $Tb_3Fe_5O_{12}$ thin film | Pt heterostructures and highlights the differences to $Tb_3Fe_5O_{12}$ single crystal | Pt heterostructures. These differences are then addressed by several experimental attempts, which aim to reveal the origin of the different signatures of the spin Seebeck effect observed in $Tb_3Fe_5O_{12}$ single crystals and $Tb_3Fe_5O_{12}$ thin films.

5.1. Experimental procedure and data analysis for spin Seebeck effect experiments

For the investigation of the spin Seebeck effect in $Tb_3Fe_5O_{12}$ (TbIG) | Pt heterostructures, the samples are patterned into a Hall-bar mesa-structure using optical lithography and Ar-ion milling. The mesa-structure is then wire-bonded to a chip-carrier, which enables the recording of the longitudinal V_{long} and the transverse voltage drop V_{trans} within a four point measurement setup while a DC-current I_d along the Hall-bar is applied (see Fig. 5.1.1). Within this work, the Hall-bar is aligned with the current direction parallel to the magnetically easy cubic $[111]_{bcc}$-direction of TbIG. To establish a good thermal contact with the sample holder, the sample is mounted on the copper block of a chip-carrier with GE Varnish. The chip-carrier is then mounted on a dipstick which is inserted into a magnet cryostat. Due to good thermal contact between the bottom side of the sample and the dipstick, the assumption that the dipstick temperature equals the temperature at the bottom side of the sample is valid. The sample is oriented such that the magnetic field, parametrized by the angle α and magnitude H, can only be varied within the sample plane (see Fig. 5.1.1). The magnet cryostats at the Walther-Meißner-Institute which are used in this work allow to control the temperature of the dipstick T_{dip} from $5\,K$ to $300\,K$ and the magnetic field up to $\mu_0 H = 15\,T$. To establish a thermal gradient in out-of-plane direction, which is the driving force of the spin Seebeck effect, a current of $I_d = 5\,mA$ is applied for resistively heating the Pt-layer. At each point of the measurement, the DC-current direction is inverted 6 times allowing a separation of thermal and resistive voltage signals. For the determination of the established Pt-temperature T_{Pt} due to resistive heating, the longitudinal voltage V_{long} as a function of

temperature is recorded while a current of $I_d = 100\,\mu A$ is applied. With the calculated resistance $R(T_{Pt})$ of the Pt-layer as a function of temperature, the Pt-temperature can be estimated while resistively heating the Pt-layer with a current of $I_d = 5\,mA$. Therefore, first, any resistive heating of the Pt-layer for a current of $I_d = 100\,\mu A$ is neglected, such that the dipstick temperature is assumed to be equal to the Pt-temperature and, second, Ohm's law is also applicable in the case of $I_d = 5\,mA$, where an additional quadratic voltage-dependence is expected due to resistive heating of the Pt-layer.

Within this work, only field-dependent spin Seebeck effect experiments (FD-SSE) are conducted due to the large magnetic anisotropy of TbIG along the cubic $[111]_{bcc}$-directions, in particular at low temperatures (for a more detailed description see section 2.3.4). Thus, the external magnetic field $\mathbf{H}$ as well as the current direction I_d are aligned parallel to the cubic $[111]_{bcc}$-direction which is equal to $\alpha = 0°$. The FD-SSE experiments are conducted at constant temperatures T_{dip} between $5\,K$ and $300\,K$. To cover the full hysteresis loop, the magnitude of the external magnetic field $\mathbf{H}$ is swept from $+H_{max} \to -H_{max} \to +H_{max}$ with $H_{max} = 7\,T$ or $H_{max} = 15\,T$ depending on the used experimental setup. For measuring the voltage drops V_{long} and V_{trans}, Keithley K2182 Nanovoltmeters are used as voltmeters together with a Keithley K2400 Source Meter as current source.

To analyze the data, the thermal V_{therm} and the resistive V_{res} voltage signals have to be separated by usage of the so-called delta-method. This method utilizes, that resistive effects yield point symmetric $V - I$ dependencies, whereas thermal effects yield mirror symmetric $V - I$ dependencies. This leads to following identities:

$$V_{therm}(I) = V_{therm}(-I) \tag{5.1}$$

$$V_{res}(I) = -V_{res}(-I) \tag{5.2}$$

$$V_{therm} = \frac{V(+I) + V(-I)}{2} \tag{5.3}$$

$$V_{res} = \frac{V(+I) - V(-I)}{2}. \tag{5.4}$$

Here, $V(+I)$ and $V(-I)$ are the raw voltage signals with the current density $\mathbf{J} \upuparrows \mathbf{x}$ and $\mathbf{J} \updownarrows \mathbf{x}$, respectively. The size of current density is defined by $|\mathbf{J}| = I_d/(d_{Pt} \cdot w_{HB})$, where d_{Pt} is the thickness of the Pt-layer and w_{HB} is the width of the current path of the Hall-bar mesa-structure. The expected voltage signals originating from the spin Seebeck effect are schematically shown and explained in section 2.3.4 and in Fig. 2.3.3. Since the external magnetic field is aligned at $\alpha = 0°$ and the spin Seebeck effect is a thermally driven effect, the voltage signals originating from the spin Seebeck effect are expected in the thermal component of the transverse voltage drop $V_{therm,trans}$.
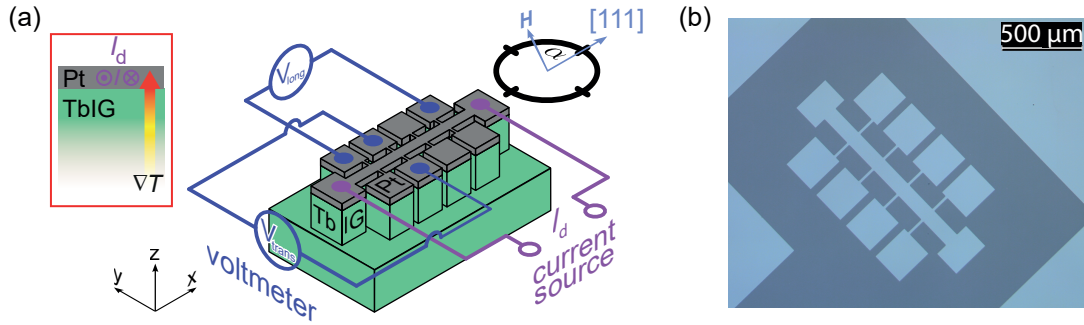
Figure 5.1.1.: (a) Schematic drawing of a Hall-bar mesa-structure after patterning and wire-bonding which is enabling a four point measurement of the transverse V_{trans} and longitudinal V_{long} voltage drop. The sample is mounted inside a magnet cryostat such that the magnetic field can be varied in the sample plane (**x-y**-plane). Due to application of a DC-heating current $I_{\text{d}} = 5\,\text{mA}$ with alternating directions a thermal gradient is established in out-of-plane (**z**) direction. (b) Photograph of a TbIG | Pt heterostructure after optical lithography and Ar-ion milling.

5.2. Spin Seebeck effect in Tb$_3$Fe$_5$O$_{12}$ single crystal|Pt heterostructures

5.2.1. Sample preparation

The spin Seebeck effect experiments with the Tb$_3$Fe$_5$O$_{12}$ (TbIG) single crystal | Pt heterostructure are conducted with a single crystal, which has the cubic [110]-direction oriented parallel to the out-of-plane direction. To flatten the sample surface, the crystal is polished in the first step. Subsequently, the crystal is dipped into Piranha-acid for two minutes. For the Piranha-acid, a mixture of H$_2$SO$_4$ and 35% H$_2$O$_2$ in aqueous solution at a ratio of $3 : 1$ is used. After dipping the crystal in Piranha-acid, it is stored in a container filled with distilled water to prevent contamination of the surface. The third step is annealing the TbIG single crystal in the PLD-chamber of the UHV-cluster (see section A.1.3). For this procedure, the sample is mounted on a Kanthal sample holder, which is heated from the backside by an infrared Laser up to a temperature of $450\,^\circ\text{C}$ with an on- and off-ramp of $25\,^\circ\text{C/min}$. To avoid oxygen vacancies, the whole annealing process is performed inside an oxygen atmosphere with a pressure of $10\,\mu\text{bar}$. Since the amplitude of the spin Seebeck effect is directly proportional to the spin-mixing conductance $g^{\uparrow\downarrow}$, which mainly relies on a high interface quality, a clean interface between the Pt-layer and the TbIG single crystal is mandatory (see section 2.3.1). Therefore, the sample is transferred in-situ, without breaking the vacuum, into the EVAP-chamber of the UHV-cluster, where a Pt-thin film with a thickness of $(4.0 \pm 0.1)\,\text{nm}$ is deposited via electron beam evaporation (see section A.1.4). To pre-characterize the sample, X-ray diffraction experiments are performed. The two main X-ray diffraction measurements are shown in Fig. 5.2.1. From the reflectometry (see Fig. 5.2.1 (a)), the Pt-thickness $d_{\text{Pt}} = (4.0 \pm 0.1)\,\text{nm}$, the interface roughness $R_{\text{RMS,interface}} = (0.2 \pm 0.1)\,\text{nm}$ and the surface roughness $R_{\text{RMS,surface}} = (0.55 \pm 0.10)\,\text{nm}$ are extracted by refining a LEPTOS-simulation to the raw data. The single peak structure of the rocking curve (see Fig. 5.2.1 (b)) around the (880) Bragg-reflection of TbIG with a full width at half maximum (FWHM) of only $(0.0160 \pm 0.0001)^\circ$ reveals a single crystalline

TbIG sample with a small mosaicity and no secondary crystallites. As a final step of preparation, the sample is patterned and wire-bonded as described in section 5.1.
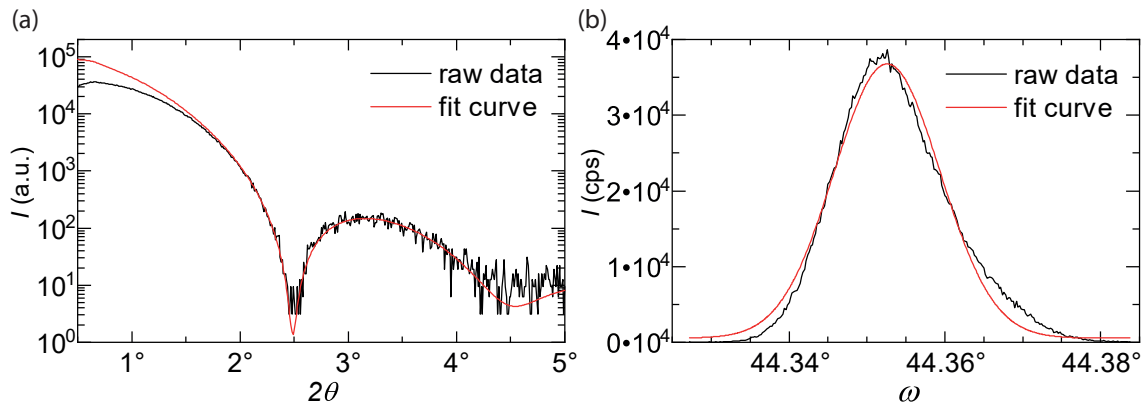

Figure 5.2.1.: X-ray diffraction measurements on the TbIG single crystal | Pt heterostructure, which is used for spin Seebeck effect experiments within this work. (a) Reflectometry measurement (black curve) plotted together with the LEPTOS-simulation (red curve). The determined simulation parameters are $d_{Pt} = (4.0 \pm 0.1)\,nm$, $R_{RMS,interface} = (0.2 \pm 0.1)\,nm$ and $R_{RMS,surface} = (0.55 \pm 0.10)\,nm$. (b) Rocking curve around the (880) Bragg-reflection of the TbIG single crystal. The fit of a Gaussian function to the data (red curve) reveals a small mosaicity and a very high crystalline quality resulting in a full width at half maximum (FWHM) of only $(0.0160 \pm 0.0001)°$.

5.2.2. Results of field-dependent spin Seebeck experiments

The key part of the experimental data of FD-SSE experiments with the $Tb_3Fe_5O_{12}$ single crystal | Pt heterostructure after the application of the delta method to the transverse V_{trans} (upper panels) and longitudinal V_{long} (lower panels) is plotted in Fig. 5.2.2. The plotted data is the average of three subsequent measurements at each point of the hysteresis loop. Starting at low temperatures $T_{Pt} = (33 \pm 1)\,K$ (see Fig. 5.2.2 (a)), the hysteresis loop of the transverse thermal voltage signal $V_{therm,trans}$ is running from negative voltages at negative fields to positive voltages at positive fields resulting in a positive amplitude of the spin Seebeck effect (SSE) ($V_{SSE}(T_{Pt}) > 0$). When the temperature is increased to $T_{Pt} = 53\,K$ (see Fig. 5.2.2 (b)), the hysteresis of the transverse thermal voltage drop $V_{therm,trans}$ and thus the amplitude of the SSE V_{SSE} is inverted. As the temperature is further increased, also the absolute value of the SEE-amplitude increases (see Fig. 5.2.2 (c), (d),(e)), whereas no signature which can be attributed to the rhombohedral-to-cubic structural phase transition of TbIG at $T_{rh} \approx 190\,K$ [31] is found. As the temperature crosses the magnetic compensation temperature $T_{comp} = 250.5\,K$, the hysteresis loop of the transverse thermal voltage is inverted a second time, leading to a positive SSE-amplitude. Therefore, TbIG exhibits similar to GdIG two sign changes of the SSE-amplitude: At low temperatures, between $T_{Pt} = 33\,K$ and $T_{Pt} = 53\,K$, a first sign change at T_{sign1} occurs and a second sign change takes place around the magnetic compensation temperature at T_{sign2}.

The longitudinal thermal voltage $V_{therm,long}$ shows as expected no signature of the SSE due to the vanishing longitudinal component resulting from the cross-product $V_{therm,long} \propto (\mathbf{J}_S \times \mathbf{s}) \cdot \hat{\mathbf{x}} = 0$ which parametrizes the inverse spin Hall effect (see Eq. (2.5)).

The longitudinal and transverse resistive voltage signals $V_{\mathrm{res,long}}$ and $V_{\mathrm{res,trans}}$ are caused by the spin Hall magnetoresistance, which will be discussed in the following subsection in more detail. This leads to peaks (dips) of the recorded transverse (longitudinal) resistive voltage signal at the coercive fields and is in good agreement to magnetic hysteresis measurements by SQUID-magnetometry (see Fig. B.0.2), which e.g. at $10\,\mathrm{K} \Leftrightarrow T_{\mathrm{Pt}} = 33\,\mathrm{K}$ show a small coercive field of $H_{\mathrm{C}} = 40\,\mathrm{mT}$ and a remanent magnetisation of $M_{\mathrm{r}}/M_{\mathrm{s}} = 0.15$ where M_{s} is the saturated magnetization along the $[111]_{\mathrm{bcc}}$-direction. This accordance of the resistive voltage signals and SQUID-magnetometry measurements is valid for all investigated temperatures. In the vicinity of $T_{\mathrm{sign,2}}$ and therefore T_{comp} (see Fig. 5.2.2 (e),(f)), the transverse resistive voltage $V_{\mathrm{res,trans}}$ shows an upturn at high fields which is not found further away from $T_{\mathrm{sign,2}}$. Thus, this behavior is related to a canting of the sublattice magnetizations which occurs in high fields around T_{comp} and is well known for the similar material system GdIG [29]. The longitudinal resistive voltage signal $V_{\mathrm{res,long}}$ shown in Figs. 5.2.2 (d),(e),(f) is attributed to temperature drifts during the measurements.
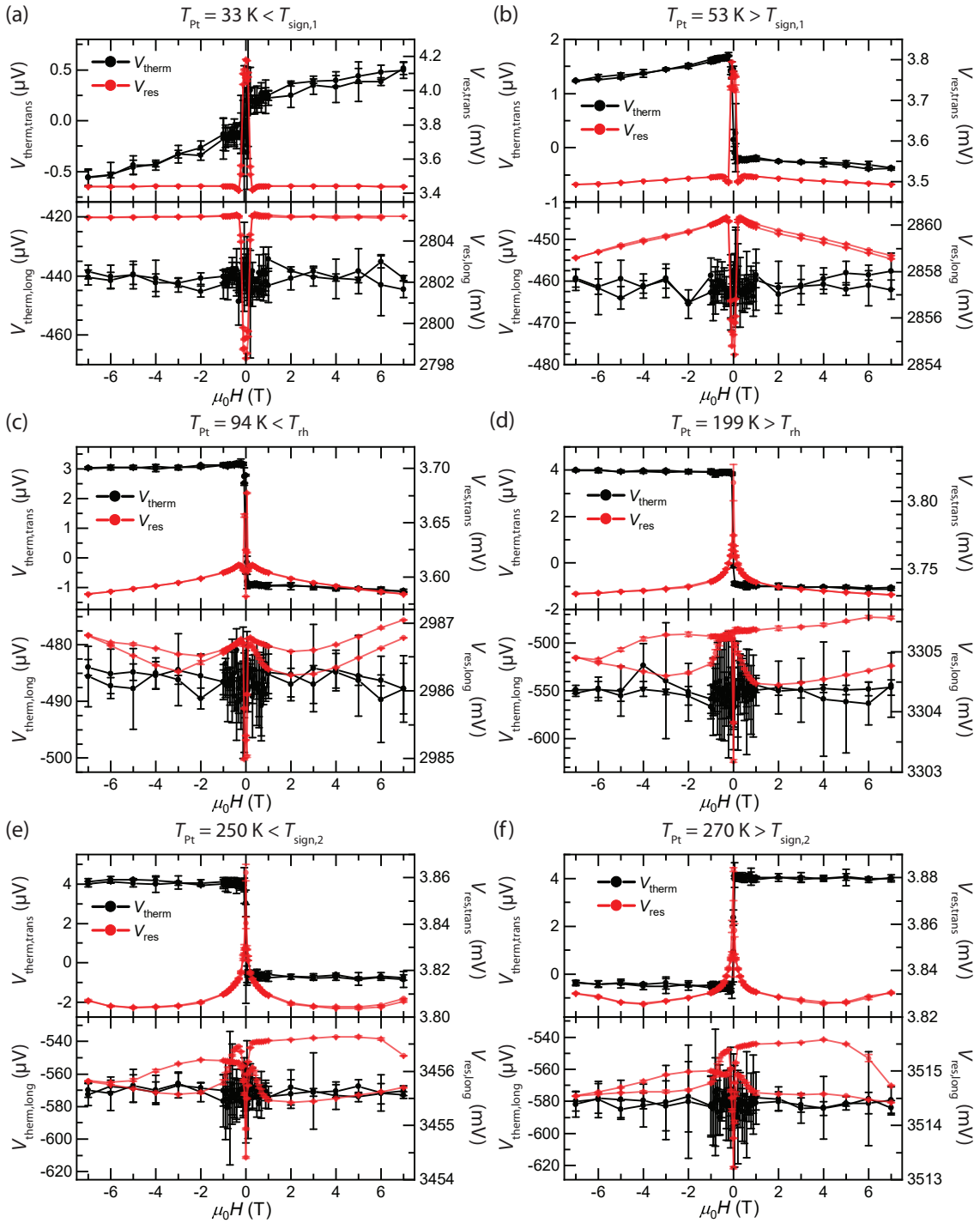
Figure 5.2.2.: Thermal (black) and resistive (red) voltage signals measured transverse (upper panels) and longitudinal (lower panels) to the current direction in field-dependent SSE (FD-SSE) experiments on a TbIG single crystal | Pt heterostructure. The data shown here is measured around the critical temperatures of TbIG. (a),(b) Inversion of the hysteresis loop of the thermal transverse voltage $V_{\text{therm,trans}}$ signal at $T_{\text{sign,1}}$. (c),(d) No signature related to the rhombohedral-to-cubic phase transition of TbIG at $T_{\text{rh}} \approx 190\,\text{K}$. The absolute value of the SSE-amplitude V_{SSE} increases with increasing temperatures. (e),(f) Inversion of the hysteresis loop of the transverse thermal voltage signal $V_{\text{therm,trans}}$ in the vicinity of the magnetic compensation temperature T_{comp} at $T_{\text{sign,2}}$. The upturn of the transverse resistive $V_{\text{res,trans}}$ voltage signal in high fields is related to a canting of the sublattice magnetizations around T_{comp}. Overall, the resistive voltage signals show the signature which is expected for the spin Hall magnetoresistance.

Spin Hall magnetoresistance extracted from field-dependenent spin Seebeck effect experiments

This chapter briefly outlines the expected resistive longitudinal and transverse voltage signal due to the spin Hall magnetoresistance according to Althammer *et al.* [41]. The spin Hall magnetoresistance describes the absorption of a spin accumulation at a ferrimagnetic insulator (FMI) | heavy metal (HM) interface by the magnetic sublattices of the FMI. The spin accumulation at the interface is generated by the inverse spin Hall effect when a charge current with current density $J = |\mathbf{J}| = I_d/(d_{Pt} \cdot w_{HB})$ is flowing through a heavy metal with strong spin-orbit coupling, e.g. Platinum. If the sublattice magnetization of the ferrimagnetic insulator is not parallel or antiparallel to the spin accumulation, the accumulated spins exert a torque on the magnetization and thus get absorbed. This is opening an additional dissipation channel depending on the angle between the spin accumulation and the magnetization of the FMI. In total, the longitudinal and transverse voltage drop due to the spin Hall magnetoresistance is parametrized as

$$V_{long} = J \cdot (\rho_0 + \rho_1[\hat{\mathbf{m}} \cdot \hat{\mathbf{y}}]^2) \tag{5.5}$$

$$= J \cdot (\rho_0 + \rho_1 \cos^2(\alpha)) \tag{5.6}$$

$$V_{trans} = J \cdot (\rho_2[\hat{\mathbf{m}} \cdot \hat{\mathbf{z}}] + \rho_3[\hat{\mathbf{m}} \cdot \hat{\mathbf{x}}][\hat{\mathbf{m}} \cdot \hat{\mathbf{y}}]) \tag{5.7}$$

$$= J\rho_3(-\frac{1}{2} + \cos^2(\alpha - 45°)) \tag{5.8}$$

with the normalized magnetization vector $\hat{\mathbf{m}} = \mathbf{M}/M$.

Within this work, TbIG is used as the FMI and Pt as the HM layer. TbIG exhibits a strong cubic magnetic anisotropy with magnetically easy axes along the cubic $[111]_{bcc}$-directions. SQUID-magnetometry measurements reveal a small remanent magnetization and low coercive field H_c between $10\,K$ and $300\,K$ (e.g. $M_r(10\,K)/M_s(10\,K) = 0.15$ and $H_c(10\,K) < 10\,mT$, see Fig. B.0.2). Thus, the assumption that the magnetic structure of the (110)-oriented TbIG single crystal for $H = H_c$ consists of four different, equally distributed magnetic domains with magnetizations parallel to the four degenerated cubic $[111]_{bcc}$-directions in the sample plane is valid (see Fig. 5.2.3). Due to the not symmetric distribution of the $[111]_{bcc}$-directions with respect to $\alpha = 0°$ this is leading to the following expected longitudinal voltage drop at $H = H_c$.

$$V_{long}(H = H_c) = \frac{1}{4}\big(V_{long}(\hat{\mathbf{m}} \parallel [111]) + V_{long}(\hat{\mathbf{m}} \parallel [\bar{1}\bar{1}\bar{1}])$$
$$+ V_{long}(\hat{\mathbf{m}} \parallel [11\bar{1}]) + V_{long}(\hat{\mathbf{m}} \parallel [\bar{1}\bar{1}1])\big) \tag{5.9}$$

$$= \frac{1}{2}\big(V_{long}(\hat{\mathbf{m}} \parallel [111]) + V_{long}(\hat{\mathbf{m}} \parallel [11\bar{1}])\big) \tag{5.10}$$

$$= \frac{1}{2}\big(V_{long}(\alpha = 0°) + V_{long}(\alpha = -54.73°)\big) \tag{5.11}$$

$$= J \cdot \left(\rho_0 + \rho_1\frac{1 + \cos^2(-54.73°)}{2}\right) < V_{long}(\alpha = 0°) \tag{5.12}$$

In Eq. (5.10), the 180°-symmetry of the spin Hall magnetoresistance is exploited. For $|\mu_0 H| > 0.3\,T \gg H_c$, the magnetization is saturated along the cubic $[111]_{bcc}$-direction

($\alpha = 0°$) and thus $V_{\text{long}}(|\mu_0 H| > 0.3\,\text{T}) = V_{\text{long}}(\alpha = 0°)$. This is leading to the observed dip in the longitudinal resistive voltage signal $V_{\text{res,long}}$ at the coercive field H_{c}, which matches the spin Hall magnetoresistance effect. Analogously,

$$V_{\text{trans}}(H = H_{\text{c}}) = \frac{1}{2}\left(V_{\text{trans}}(\alpha = 0°) + V_{\text{trans}}(\alpha = -54.73°)\right) \tag{5.13}$$

$$= J\rho_3\left(-\frac{1}{2} + \frac{1}{2}(\cos^2(-45°) + \cos^2(-99.73°))\right) < V_{\text{trans}}(\alpha = 0°) \tag{5.14}$$

where $\rho_3 = -\rho_1$ according to Ref. [41]. Thus, a peak in the transverse resistive voltage signal $V_{\text{res,trans}}$ at $H = H_{\text{c}}$ is expected.

In total, the parametrization of the spin Hall magnetoresistance together with the cubic magnetic anisotropy of TbIG explains the resistive voltage signals extracted from the FD-SSE experiments with a TbIG single crystal | Pt heterostructure.
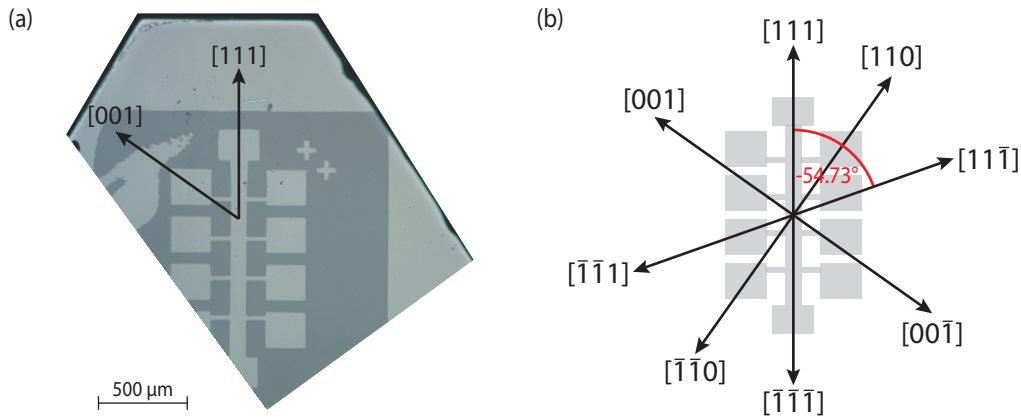
Figure 5.2.3.: (a) Photograph under a microscope of the (110)-oriented TbIG single crystal | Pt heterostructure with the patterned Hall-bar aligned along the cubic $[111]_{\text{bcc}}$-direction. (b) Crystallographic directions within the cubic (110)-plane. Due to the strong cubic magnetic anisotropy with the magnetically easy axes along the cubic $[111]_{\text{bcc}}$-directions, the magnetic structure in the absence of an external magnetic field consists of four different, equally distributed domains with magnetizations parallel to the four degenerated $[111]_{\text{bcc}}$-directions within the (110)-plane. The angle between the $[111]_{\text{bcc}}$-directions, which is used in the calculation above, is highlighted in red. This is resulting in a small remanent magnetization M_{r} and low coercive field H_{c} as well as the peak (dip) structure in the transverse (longitudinal) resistive voltage signal due to the spin Hall magnetoresistance.

5.2.3. Magnon driven spin Seebeck effect in $Tb_3Fe_5O_{12}$ single crystal|Pt heterostructures

To obtain the main result of the FD-SSE experiment, the SSE-amplitude V_{SSE} as a function of the Pt-layer temperature T_{Pt} is calculated for magnetic fields between $0.5\,\text{T}$ and $7\,\text{T}$ using Eq. (2.37) (see Fig. 5.2.4 (d)). In the following, the temperature evolution of V_{SSE} with respect to the chirality dependent spin wave dispersion relation, which is determined by inelastic neutron scattering and subsequent simulation with SpinW at $T = 10\,\text{K}$, $T = 100\,\text{K}$ and $T = 280\,\text{K}$ (see Fig. 5.2.4 (a),(b),(c)) is presented.

At low temperatures ($T = 10\,\text{K}$, see Fig. 5.2.4 (a)), the spin wave dynamics are mainly governed by the fundamental ferrimagnetic resonance mode, which describes the precession

of the local magnetic moments of all sublattices in phase. This ferromagnetic resonance mode is the red mode up to $2.3\,\mathrm{meV}$, which additionally shows a mixed chirality in the vicinity of the Γ-Point due to the opening of the magnetic double-umbrella structure at low temperatures. In total, the spin Seebeck effect is mainly driven by spin waves with positive, red chirality leading overall to a positive SSE-amplitude V_{SSE}.

With increasing temperatures, the optical modes shift downwards in energy, which is leading to the crossing of the thermal energy and the energy gap of the first optical mode with negative chirality ($\mathrm{i}\cdot(S^{xy}-S^{yx})<0$ (blue)) at $T_{\mathrm{cross}}=70\,\mathrm{K}$ (see section 4.4.4). Due to gradual population of the first optical mode in this temperature regime, a gradual sign change of the SSE-amplitude V_{SSE} is expected in this temperature region. In a simple two channel model at $T_{\mathrm{sign,1}}$ both channels transport the same amount of spin angular momentum across the interface, leading in total to a vanishing spin current across the interface due to opposite chirality of both channels. Experimentally, the temperature of the first sign change is found at $T_{\mathrm{sign,1}}=(36\pm3)\,\mathrm{K}$, which is well below T_{cross}. The reason for this observation is most likely originating form the mixed chirality of the acoustic mode and flat band structure due to the presence of the magnetic 'double-umbrella' structure. This is supported by the higher temperature of the first sign change $T_{\mathrm{sign,1,GdIG}}=77\,\mathrm{K}$ in the similar material system GdIG, which exhibits a collinear magnetic structure at low temperatures far away from the magnetic compensation temperature [42]. Since so far there are no experimental data points in the low energy region of the spin wave dispersion relation, this should be subject to further experimental investigation.

At $100\,\mathrm{K}$ (see Fig. 5.2.4 (b)), the thermal energy is already within the first optical, strongly dispersing mode with negative chirality ($\mathrm{i}\cdot(S^{xy}-S^{yx})<0$ (blue)) due to the increasing thermal energy and downwards shift in energy of the first optical mode. Thus, the spin Seebeck effect with its amplitude V_{SSE} is mainly driven by this mode leading to a further decreasing negative SSE-amplitude up to $150\,\mathrm{K}$.

When the magnetic compensation temperature $T_{\mathrm{comp}}=250.5\,\mathrm{K}$ is crossed, all magnetic sublattices and thus the spin wave chiralities invert, leading to a second, abrupt sign change in the temperature profile of the SSE-amplitude. Here, the temperature of the second sign change $T_{\mathrm{sign,2}}=(255\pm5)\,\mathrm{K}$ matches the magnetic compensation temperature determined by SQUID-magnetometry $T_{\mathrm{comp}}=250.5\,\mathrm{K}$ within the uncertainty range. The chirality inversion of the spin wave excitations is also found in the spin wave dispersion relation at $280\,\mathrm{K}$ (see Fig. 5.2.4 (c)). Additionally, above $T_{\mathrm{sign,2}}$ the simulations show an exchange of the acoustic mode by the previous optical mode. This was also observed in simulations by Ganzhorn *et al.* for GdIG [12]. Physically, this observation can be explained by the constraint that the fundamental magnetic excitation requires its magnetic moment to be antiparallel to the magnetization, which is equal to $\mathrm{i}\cdot(S^{xy}-S^{yx})>0$ (red).

In summary, the experimentally determined spin wave dispersion relation (see section 3), which was successfully simulated with SpinW (see section 4), is able to explain the temperature profile of the spin Seebeck effect. This was also predicted by theory (see sections 2.3.1 and 2.3.3) and is confirmed within this work. Thus, the spin Seebeck effect provides an experimental setup to probe the fundamentals of spin wave dispersion relations in magnetically ordered insulators.
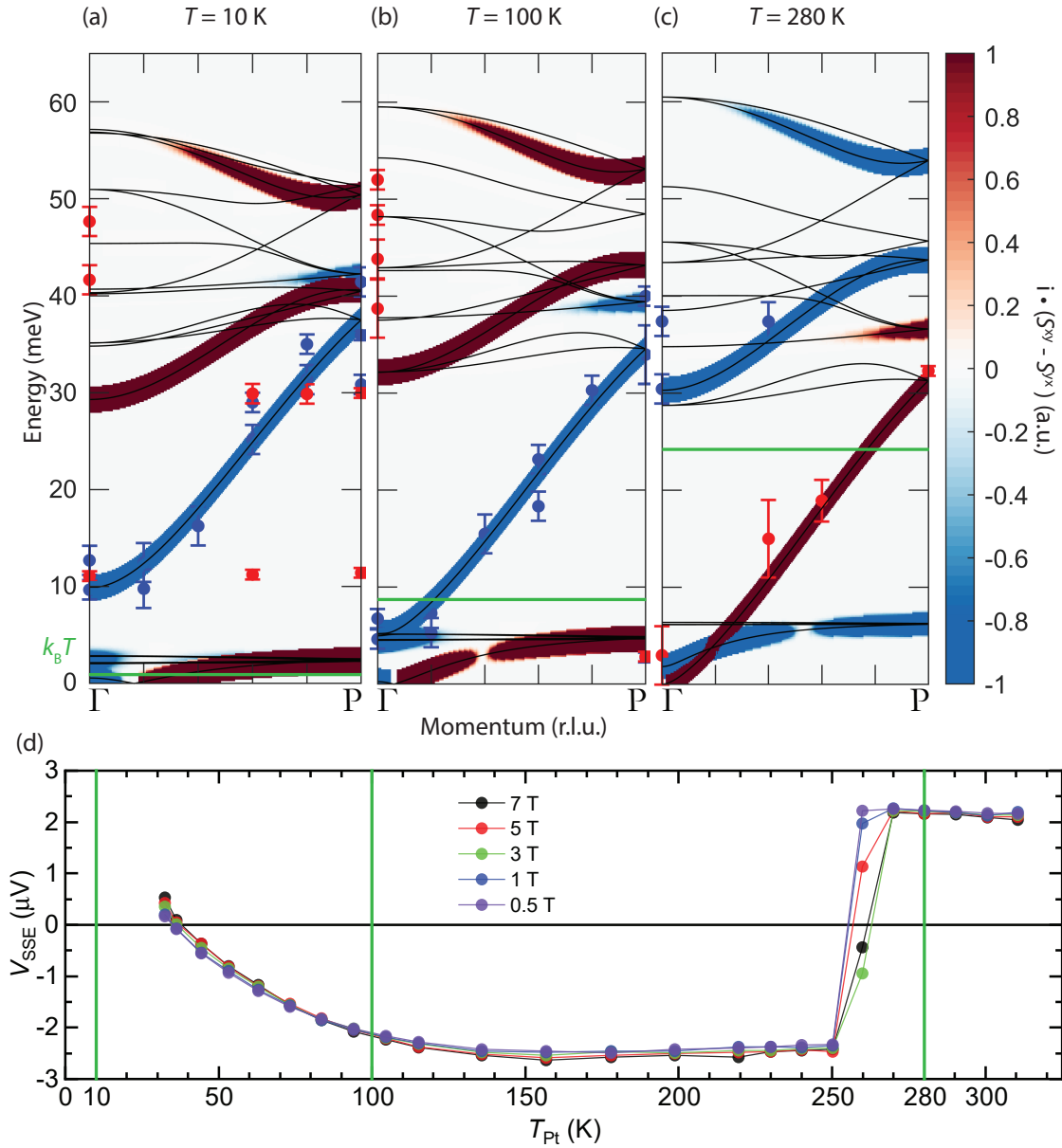
Figure 5.2.4.: (a),(b),(c) Experimentally verified chirality dependent spin wave relations in TbIG at 10 K, 100 K and 280 K. The data points are extracted from inelastic neutron scattering with polarization analysis on a TbIG single crystal and plotted together with the results of the SpinW-simulation. The thermal energy level is marked as a green line. (d) SSE-amplitude as a function of temperature $V_{SSE}(T_{Pt})$ extracted from the data shown in Fig. 5.2.2 at external magnetic fields between 0.5 T and 7 T. The temperatures of the spin wave dispersion relations shown in (a)-(c) are marked by vertical green lines. The temperature profile matches the spin wave dispersion relations found in this work. This proves that the spin Seebeck effect provides an easy experimental setup to probe the fundamentals of spin wave dispersion relations in magnetically ordered insulators.

5.3. Spin Seebeck effect in Tb$_3$Fe$_5$O$_{12}$ thin film|Pt heterostructures

In addition to the investigation of the spin Seebeck effect in TbIG single crystal | Pt heterostructures, the spin Seebeck effect in TbIG thin film | Pt heterostructures is investigated within this work. The usage of TbIG thin films offers a further simplification in the sample production for spin Seebeck effect experiments and is an important step towards spintronic devices.

The first part of this section focuses on the sample preparation followed by the discussion of the results of field-dependent spin Seebeck experiments. Subsequently, the differences of the spin Seebeck effect in TbIG single crystal | Pt and TbIG thin film | Pt heterostructures are highlighted and various attempts to overcome these differences are presented.

5.3.1. Sample preparation

For the fabrication of TbIG thin film | Pt heterostructures (in the following TbIG | Pt heterostructures), Gd$_3$Ga$_5$O$_{12}$ (GGG) substrates, which are comercially fabricated by Crys-Tec GmbH, are used. This choice of substrate is based on the small lattice mismatch $\epsilon_{\mathrm{GGG}} = \frac{a_{\mathrm{GGG}} - a_{\mathrm{TbIG}}}{a_{\mathrm{TbIG}}} = -0.5\%$ between TbIG and GGG and the identical cubic space group at the growth temperature. The GGG-substrates are one-side-polished and have a size of $5\,\mathrm{mm} \times 5\,\mathrm{mm}$ with the crystallographic $[110]_{\mathrm{bcc}}$-direction pointing out-of-plane. Prior to the growth of the TbIG thin film, a Pt-layer with a thickness of $\approx 180\,\mathrm{nm}$ is deposited on the unpolished back side of the substrate with a high vacuum sputtering device. This Pt-layer is needed to increase the absorption of the infrared heating laser and therefore to ensure a high homogeneity of the substrate temperature. Subsequently, the sample is cleaned with isopropanol and acetone and mounted inside the load-lock of the UHV-cluster (see section A.1.2)

The TbIG thin film is deposited by pulsed laser deposition (PLD) (see section A.1.3). During the deposition process, the substrate is heated from the back side by an infrared-laser, which is controlled by a feedback-loop of a pyrometer measuring the sample temperature. This ensures a constant substrate temperature T_{S}, which is needed since only the right temperature allows the adsorbed atoms from the plasma to form a crystalline thin film. The whole process is carried out inside an oxygen atmosphere with pressure p_{O2}. With the right pressure p_{O2}, oxygen vacancies are suppressed and an ideal crystalline thin film without parasitic phases (e.g. TbFeO$_3$) is fabricated. For the deposition, the pulsed UV-excimer laser hits a stoichiometric polycrystalline target with an energy density of $\rho_{\mathrm{L}} = 2\,\mathrm{J/cm^2}$ at frequency of $10\,\mathrm{Hz}$ and creates a plasma, which propagates towards the substrate. The total number of 25000 pulses is divided into packs of 250 pulses with a relaxation time of $t_{\mathrm{R}} = 10\,\mathrm{s}$ between the pulses to assure a low surface roughness and a high quality crystalline growth of the TbIG thin film.

After the PLD-process, the sample is transferred in-situ, without breaking the vacuum into the electron beam evaporation (EVAP) chamber (see section A.1.4), where a Pt-thin film is deposited on top of the TbIG thin film. Since EVAP is a soft deposition process with thermal energies of the evaporated particles and the sample is kept in ultra high vacuum,

interdiffusion between the layers is suppressed and an ideal interface between the Pt and the TbIG layer is established. Finally, the TbIG | Pt heterostructure is patterned and wire-bonded as described in section 5.1.

To find the ideal process parameters for the fabrication of high-crystalline TbIG thin films, the results from previously conducted growth optimization at the Walther-Meißner-Institut are used as a starting point. To obtain TbIG thin films with good structural and magnetic properties, TbIG thin films with different oxygen pressures p_{O2} at a constant substrate temperature of $T_S = 450\,°C$ during the deposition covered with Pt are fabricated and investigated in terms of crystalline quality and spin Seebeck effect.

5.3.2. Results of field-dependent spin Seebeck experiments

The structural properties of the TbIG | Pt heterostructures with different oxygen growth-pressures p_{O2} of the TbIG layer are shown in Fig. 5.3.1 (a) - (c). Additionally, also re-flectometry measurements are carried out, of which the thicknesses of the TbIG | Pt het-erostructures are extracted (see Fig. B.0.3). The thickness of the thin films together with the main process parameters are shown on top of the corresponding experimental data in Fig. 5.3.1. For all samples, field-dependent spin Seebeck effect (FD-SSE) experiments are conducted leading to the $V_{SSE}(T)$-diagrams shown in Fig. 5.3.1 (d) - (f).

The 2θ-ω scans reveal that with decreasing oxygen pressure (see Fig. 5.3.1 (a)-(c)) the (880) TbIG thin film reflection shifts towards larger 2θ angles, corresponding to an increase of the out-of-plane lattice spacing. The 2θ-angle of the (880) reflection for bulk TbIG is $2\theta_{TbIG,bulk} = 88.87°$, which would correspond to a fully relaxed TbIG lattice of the TbIG thin film. For the sample which is fabricated under an oxygen pressure of $p_{O2} = 50\,\mu bar$ (see Fig. 5.3.1 (a)), the thin film peak is far away from the expected bulk value and is match-ing the parasitic, perovskite phase $TbFeO_3$. With decreasing oxygen pressure the lattice constant is approaching the bulk value. The TbIG thin film with best structural properties, which is fabricated under an oxygen pressure of $p_{O2} = 10\,\mu bar$ (see Fig. 5.3.1 (a)), shows a high intensity thin film reflection in the vicinity of the bulk value as well as pronounced Laue-oscillations. Overall, this is attributed to a high quality crystalline epitaxial growth of the TbIG thin film on a (110)-oriented GGG substrate.

The temperature profile of the SSE-amplitude $V_{SSE}(T)$ for the samples fabricated under an non-ideal oxygen pressure of $p_{O2} = 50\,\mu bar$ and $p_{O2} = 25\,\mu bar$ (see Fig. 5.3.1 (d),(e)) shows additionally a very strong field dependency as well as overall a small SSE-amplitude V_{SSE}. Additionally, the temperature of the second, abrupt sign change $T_{sign,2}$ is far below $T_{sign2,bulk} = (255 \pm 5)\,K$ for these samples, which as an indication for a non-stoichiometric composition. In contrast, the sample produced under an oxygen pressure of $p_{O2} = 10\,\mu bar$ shows the second sign change at $T_{sign,2} = (260 \pm 10)\,K$ and is indicating an overall high sample quality. In conclusion, the TbIG | Pt heterostructure with the TbIG thin film fabri-cated at an oxygen pressure of $p_{O2} = 10\,\mu bar$ exhibits the best structural and spin Seebeck effect properties. The latter properties of this heterostructure will be discussed in more detail in the following.
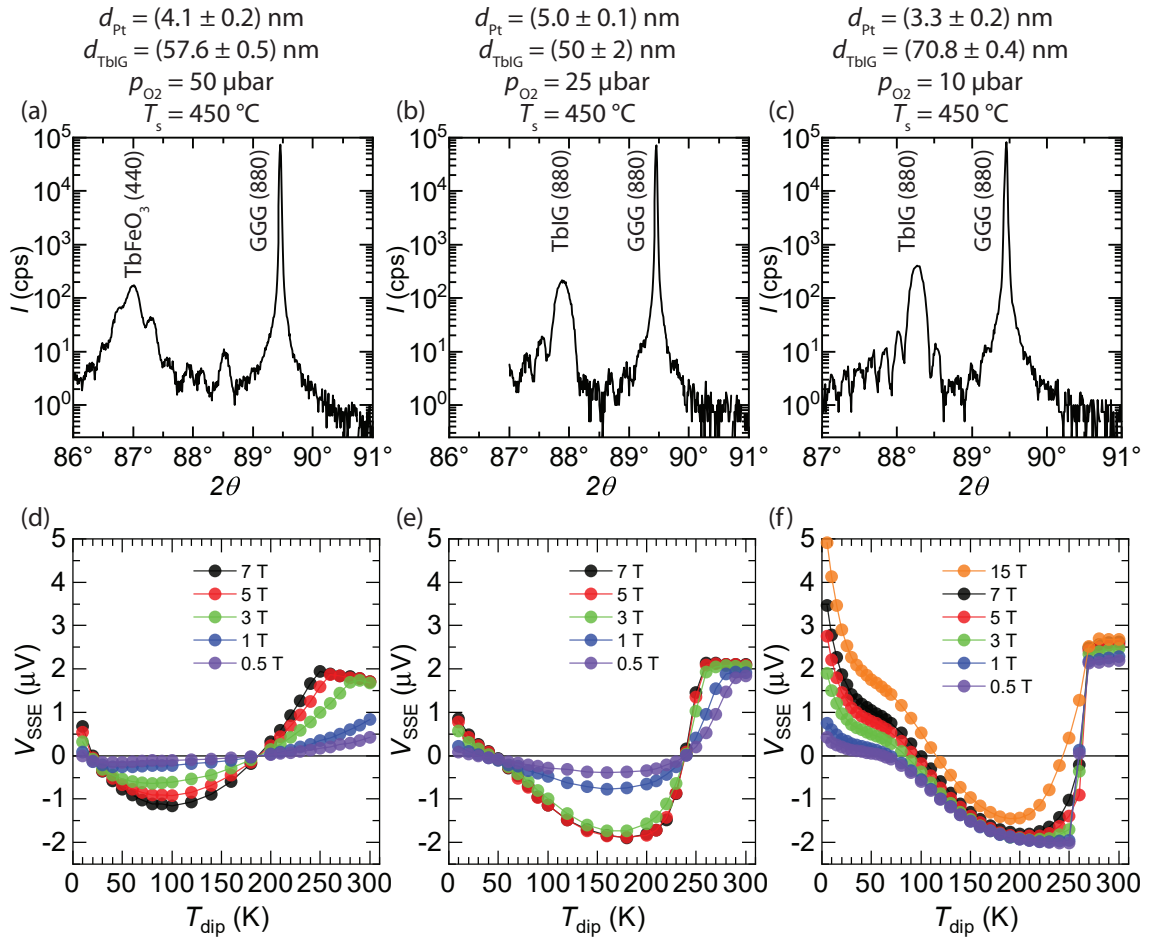
Figure 5.3.1.: Structural and spin Seebeck properties of three TbIG thin film | Pt heterostructures fabricated under different oxygen pressures $50\,\mu$bar $> p_{O2} > 10\,\mu$bar at a constant substrate temperature of $T_S = 450\,°$C. The growth parameters of the TbIG thin films (p_{O2}, T_S) as well as the thickness of the TbIG (d_{TbIG}) thin film and the Pt (d_{Pt}) layer extracted from reflectometry measurements (see Fig. B.0.3) are indicated on top of the panels. (a)-(c) The 2θ-ω scans reveal that the sample fabricated with $p_{O2} = 50\,\mu$bar consists of the parasitic phase TbFeO$_3$. In contrary, the (880) TbIG reflection of the sample fabricated with $p_{O2} = 10\,\mu$bar is close to the TbIG-bulk reflection ($2\theta_{TbIG,bulk} = 88.87°$). Furthermore, pronounced Laue-oscillations, indicating a high crystalline quality are visible. (d),(e) Spin Seebeck amplitude as a function of the dipstick temperature $V_{SSE}(T_{dip})$ extracted from field-dependent SSE experiments (see Figs. B.0.5 and B.0.6) for different applied magnetic fields. For the two TbIG thin film | Pt heterostructures with non-ideal TbIG thin films, the spin Seebeck amplitude as a function of the dip-stick temperature $V_{SSE}(T_{dip})$ shows a smaller SSE-amplitude in all temperature regions together with a strong field dependence compared to $V_{SSE}(T_{dip})$ of the TbIG | Pt heterostructure with a high crystalline TbIG layer grown under an oxygen pressure of $p_{O2} = 10\,\mu$bar. This is underlined by the lower temperature of the second abrupt sign change close to the magnetic compensation temperature, which is an indicator for a non-stoichometric composition of the TbIG thin film. (f) $V_{SSE}(T)$-diagram extracted from field-dependent SSE experiments (see Fig. 5.3.2) for the structurally ideal sample, which is discussed in the following.

The experimental data of spin Seebeck effect experiments using the ideal TbIG (70.8 nm) | Pt (3.3 nm) heterostructure fabricated under an oxygen pressure of $p_{O2} = 10\,\mu$bar is plotted in Fig. 5.3.2. To obtain the data, the delta method is applied to the transverse (upper panels) and longitudinal (lower panels) voltage drops to separate

thermal (black) and resistive (red) voltage signals (see section 5.1).

For the TbIG | Pt heterostructure, the transverse thermal voltage drop $V_{\text{therm,trans}}$ shows a large linear component at low temperatures, which is not saturating in external magnetic fields $\leq 15\,\text{T}$ (see Fig. 5.3.2 (a)-(c)). Due to the large linear component with positive slope, a low temperature sign change $T_{\text{sign,1}}(\mu_0 H)$, which is thus strongly field dependent, is observed despite no inversion of the low-field SSE hysteresis is resolved. This low temperature hysteresis inversion is visible below $T_{\text{sign,1,bulk}} = (36 \pm 3)\,\text{K}$ for the TbIG single crystal | Pt heterostructure (see Fig. 5.2.2 (a),(b)) and is matching the spin wave dispersion relation in TbIG. The linear component present in $V_{\text{therm,trans}}$ in the TbIG thin film | Pt heterostructuresis found for $T_{\text{Pt}} < 278\,\text{K}$ and increases with decreasing temperatures, whereas the size of the hysteresis decreases with decreasing temperatures illustrated by the remanent SSE amplitudes $V_{\text{r}}(137\,\text{K}) = 1.3\,\mu\text{V}$, $V_{\text{r}}(94\,\text{K}) = 0.5\,\mu\text{V}$, $V_{\text{r}}(74\,\text{K}) = 0.2\,\mu\text{V}$. For $T_{\text{Pt}} < 50\,\text{K}$, no SSE-hysteresis could be resolved (see Fig. 5.3.2 (b)-(d)). At $105\,\text{K}$, the size of the linear component of $V_{\text{therm,trans}}$ at $15\,\text{T}$ exceeds the size of the remanent SSE amplitude V_{r} causing a sign change not because of an inversion of the low-field SSE-hysteresis, but because of the linear component (see Fig. 5.3.1 (f)). Therefore, the low temperature sign change visible in Fig. 5.3.1 (f) is caused by the additional nearly linear dependence of the $V_{\text{therm,trans}}$ as a function of magnetic field magnitude. The second, abrupt sign change of $V_{\text{SSE}}(T_{\text{Pt}})$ is observed together with the expected inversion of the hysteresis at $T_{\text{sign,2}} = (260 \pm 10)\,\text{K}$, which is in agreement with the observed second sign change of $V_{\text{SSE}}(T_{\text{Pt}})$ in the TbIG single crystal | Pt heterostructure at $T_{\text{sign2,bulk}} = (255 \pm 5)\,\text{K}$ near the magnetic compensation temperature and thus indicating a stoichiometric composition of the epitaxially grown TbIG thin film.

Following the theoretical predictions, the longitudinal thermal voltage signal $V_{\text{therm,long}}$ is expected to not show any signal which is attributed to the spin Seebeck effect due to the geometric requirements of the inverse spin Hall effect ($V_{\text{therm,long}} \propto (\mathbf{J}_{\text{S}} \times \mathbf{s}) \cdot \hat{\mathbf{x}} = 0$). However, the TbIG thin film | Pt heterostructure shows a hysteretic thermal voltage signal above the noise level for $T_{\text{Pt}} > 105\,\text{K}$, which is attributed to the spin Seebeck effect (see black symbols in Fig. 5.3.2 (d)-(f)). In line with $V_{\text{trans,therm}}$ the hysteresis is inverted at $T_{\text{sign,2}}$ (see Fig. 5.3.2 (e),(f)). The most remarkable property of $V_{\text{therm,long}}$ is the size of the hysteresis, which is rapidly increasing from being non-resolvable for $T_{\text{Pt}} < 105\,\text{K}$ to $V_{\text{SSE,long}} \approx 15\,\mu\text{V}$ for $T_{\text{Pt}} > 180\,\text{K}$. Thus, for $T_{\text{Pt}} > 180\,\text{K}$, $V_{\text{SSE,long}}$ is multiple times larger than the transverse SSE-amplitude V_{SSE}, which is geometrically only possible if the polarization of the spin current across the TbIG | Pt interface has its major component perpendicular to the current direction $\mathbf{J} \parallel \hat{\mathbf{x}}$. This requires the magnetization of an ordered subsystem of TbIG to be not aligned with the external magnetic field $\parallel \hat{\mathbf{x}}$ up to an external magnetic field of $\mu_0 H = 15\,\text{T}$. Overall, none of this is observed within the TbIG single crystal | Pt heterostructure (see Fig. 5.2.2).

The longitudinal and transverse resistive voltage signals are connected to the spin Hall magnetoresistance in vicinity of $\mu_0 H = 0\,\text{T}$, where the separated peak-dip structure indicates the coercive fields, where the magnetization switches its orientation. This was also not observed in the TbIG single crystal | Pt heterostructure, where the remanent magnetization and coercive field are small. The behavior observed here is known for epitaxially

grown thin films due to pinning of magnetic moments at the interface together with a high geometrical anisotropy, which is leading to the hysteretic behavior resulting in the double peak structure observed here [43] (see also Fig. B.0.4). Additionally, there is a magnetoresistive effect which is scaling with the external magnetic field. This is not known for magnon driven effects such as e.g. the spin Seebeck effect or the spin Hall magnetoresistance in ordered magnetic systems.

In total, the resistive and thermal voltage signals observed in field-dependent spin Seebeck experiments using the TbIG thin film | Pt heterostructure differ fundamentally from the signals observed in the TbIG single crystal | Pt heterostructure. To further investigate these differences, the structural properties (see section 5.3.3) and the influence of the substrate (see section 5.3.4) are further discussed in the following sections.
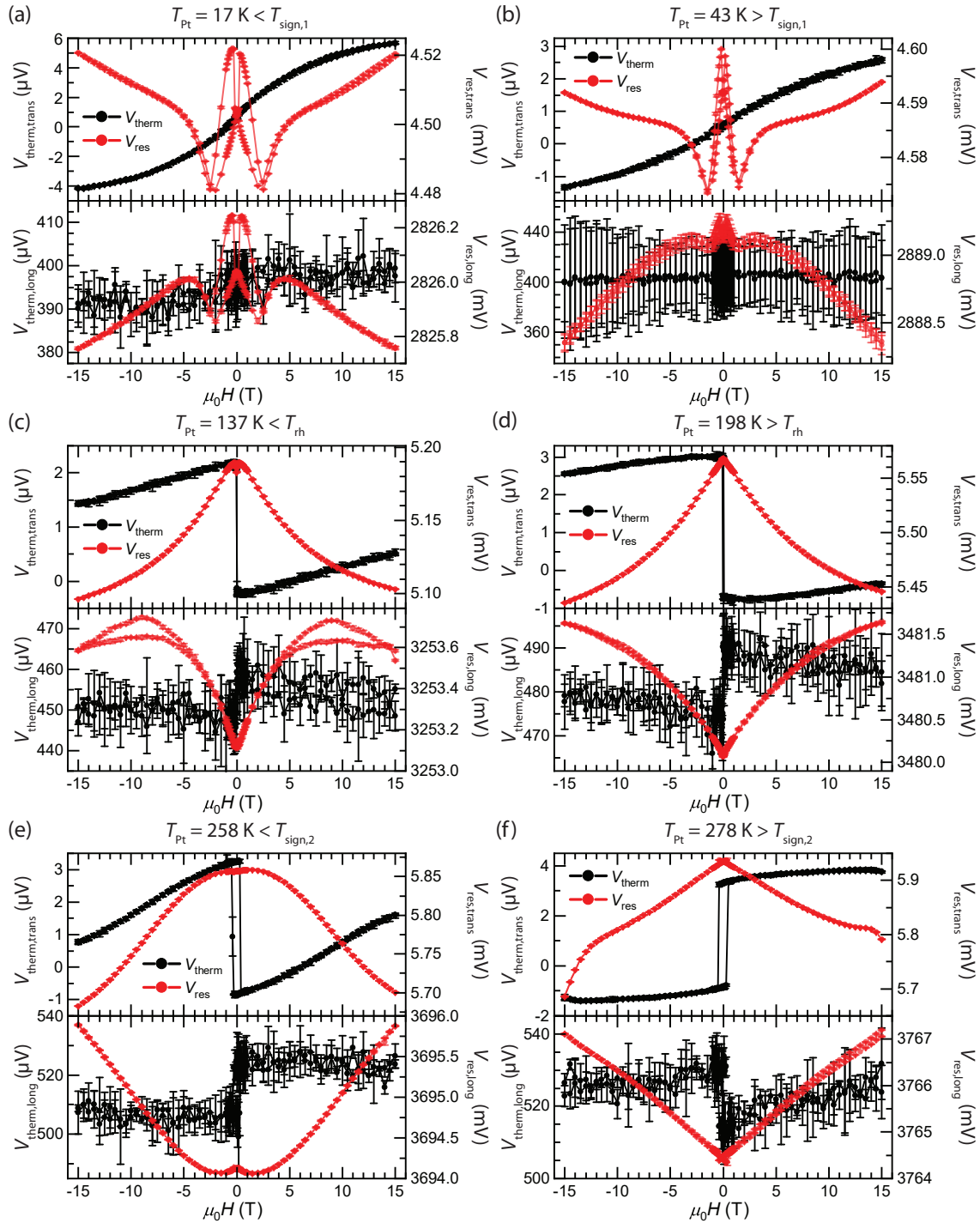
Figure 5.3.2.: Thermal (black) and resistive (red) voltage signals measured transverse (upper panels) and longitudinal (lower panels) to the current direction in field-dependent spin Seebeck effect (FD-SSE) experiments using the TbIG $(70.8\,\mathrm{nm})$ | Pt $(3.3\,\mathrm{nm})$ heterostructure fabricated on a (110)-oriented GGG substrate with the TbIG thin film grown at optimum conditions. The data shown here is measured around the critical temperatures of bulk TbIG $(T_{\mathrm{sign,1,bulk}} = (36 \pm 3)\,\mathrm{K}$, $T_{\mathrm{rh}} \approx 190\,\mathrm{K}$, $T_{\mathrm{sign,2,bulk}} = (255 \pm 5)\,\mathrm{K})$. (a),(b) Large linear component $(\propto H)$ at low temperatures dominating the transverse thermal voltage signal $V_{\mathrm{therm,trans}}$. For $T_{\mathrm{Pt}} < 50\,\mathrm{K}$ a hysteresis is not resolvable. (c),(d) Linear component in $V_{\mathrm{therm,trans}}$ is smaller than the SSE-hysteresis. Typical SSE signal is also observed in $V_{\mathrm{therm,long}}$ which should be suppressed by the measurement geometry. (e),(f) Inversion of the hysteresis in $V_{\mathrm{therm,trans}}$ and $V_{\mathrm{therm,long}}$ at $T_{\mathrm{sign,2}} = (260 \pm 10)\,\mathrm{K}$ indicating a stoichiometric composition of the TbIG thin film.

Despite all the differences between the TbIG thin film | Pt (see Fig. 5.3.3) and the TbIG single crystal | Pt heterostructure (see Fig. 5.2.4 (d)) observed in FD-SSE experiments, the SSE-amplitude $V_{SSE}(T_{Pt})$ shows qualitatively the same behavior. However, the first, low temperature, gradual sign change $T_{sign,1}$ is induced by the linear component ($\propto H$) found in the transverse thermal FD-SSE voltage $V_{therm,trans}$ at low temperatures in the TbIG thin film | Pt heterostructure. Furthermore, in this heterostructure an inversion of the SSE-hysteresis, which is expected at $T_{sign,1}$ is not observed in the low temperature regime. This results in the strong field dependence of $T_{sign,1}$ and a large SSE-amplitude V_{SSE} for $T_{Pt} < 40\,K$ and $\mu_0 H > 5\,T$. The second sign change found at $T_{sign,2} = (260 \pm 10)\,K$ matches the second sign change in the $V_{SSE}(T_{Pt})$-diagram of the TbIG single crystal | Pt heterostructure $T_{sign,2,bulk}$ and therefore the bulk magnetic compensation temperature. This indicates a stoichiometric composition of the TbIG thin film. Experiments to address the differences between the TbIG thin film | Pt heterostructure and the TbIG single crystal | Pt heterostructure observed in FD-SSE experiments are discussed in the following sections.
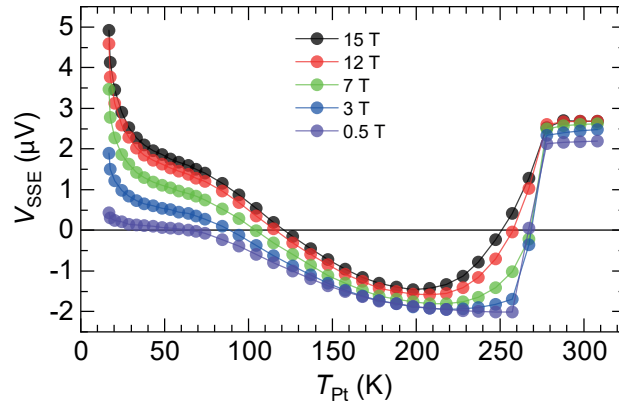
Figure 5.3.3.: $V_{SSE}(T_{Pt})$-diagram for the TbIG thin film | Pt heterostructure with the TbIG thin film fabricated under an oxygen atmosphere of $p_{O2} = 10\,\mu bar$. Qualitatively, this diagram matches the $V_{SSE}(T_{Pt})$-diagram for the TbIG single crystal | Pt heterostructure (see Fig. 5.2.4 (d)). However, the raw data reveals unexpected differences between the two samples resulting in a strong field dependence at low temperatures and thus in a strong field dependence of $T_{sign,1}$ between $70\,K$ and $120\,K$. $T_{sign,2} = (260 \pm 10)\,K$ matches the temperature of the second, abrupt sign change in the TbIG single crystal | Pt heterostructure $T_{sign,2,bulk} = (255 \pm 5)\,K$ within the error range.

5.3.3. Resonant elastic X-ray scattering on TbIG thin films

Resonant elastic X-ray scattering (REXS) experiments on a $93.6\,nm$ thick TbIG thin film grown on a (100)-oriented GGG substrate and a TbIG single crystal reveal major structural differences at low temperatures [1]. The rocking curves around the (008) Bragg-reflection of TbIG, which are detected during the REXS experiment, are shown in Fig. 5.3.4. At high temperatures ($T = 230\,K$, see Fig. 5.3.4 (a)), the TbIG single crystal is described by its non-distorted bcc-latice with space group Ia3d. At lower temperatures ($T = 52\,K < T_{rh}$, see Fig. 5.3.4 (b)), the TbIG lattice is subject to a rhobohedral distortion resulting in the description by the lower symmetry R$\bar{3}$ spacegroup [23]. This rhombohedral distortion results in

---

[1] The REXS experiments are performed by Dan Mannix at the beamline I16 of the Diamond Light Source (for details, see Ref. [44]).

the splitting of the (008) Bragg-reflection of the TbIG single crystal due to different structural domains, which is clearly observed at $52\,K$.

In contrary, the TbIG thin film sample with a TbIG layer thickness of $d_{TbIG} = 93.6\,nm$ (see Fig. 5.3.4 (c)) does not show an indication of a splitting of the (008) Bragg reflection. Thus, either the sample is in a rhombohedral monodomain state or the cubic-to-rhombohedral structural phase transition is absent in the TbIG thin film due to the elastic clamping of the thin film to the GGG substrate. Overall, this is a clear indication for fundamental structural differences between the TbIG thin film and the TbIG single crystal.

Since these structural differences observed by REXS can not be directly connected to the differences observed in spin Seebeck effect experiments, the influence of the substrate material on the SSE will be discussed in the following subsection.
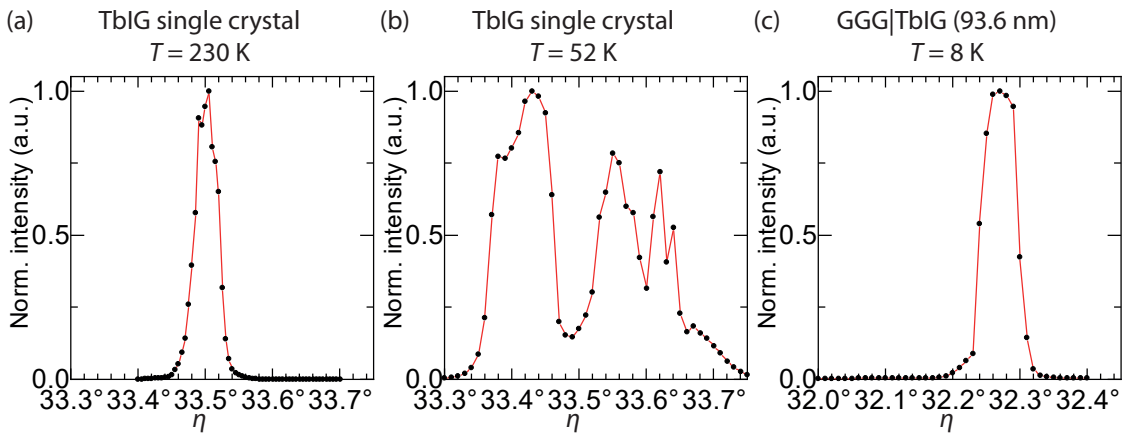
Figure 5.3.4.: Rocking curves around the (008) Bragg-reflection of TbIG measured during an REXS experiment at Diamond Light Source. (a) Single peak structure indicating a TbIG single crystal with no structural distortionl at $T = 230\,K$. (b) Splitting of the (008) Bragg-reflection due to different rhombohedral domains in TbIG at $T = 52\,K$. (c) Single peak structure of the (008) Bragg-reflection of a TbIG thin film grown on a (100)-oriented GGG substrate at $T = 8\,K$ indicating the absence of the cubic-to-rhombohedral structural phase transition.

5.3.4. Influence of the substrate material on the spin Seebeck effect in $Tb_3Fe_5O_{12}$ thin film|Pt heterostructures

To further investigate the differences between the magnetic field-dependent spin Seebeck effect in the TbIG thin film | Pt heterostructure and the TbIG single crystal | Pt heterostructure, TbIG thin film | Pt heterostructures on a (100)-oriented $Y_3Al_5O_{12}$(YAG) substrate are fabricated and investigated. To this end, the ideal parameters ($p_{O2} = 10\,\mu bar$, $T_S = 450\,°$) found for the deposition of TbIG thin films on GGG substrates are used for the PLD-deposition process of the TbIG thin film. For this sample the Hall-bar mesa-structure is patterned with the current path parallel to the $[110]_{bcc}$-direction, since (110)-oriented YAG substrates are not available. One of the two main reasons for the choice of YAG as a substrate material is the identical crystal structure of TbIG and YAG. Furthermore, in contrast to the strong quasi-paramagnetic behavior of GGG, YAG is diamagnetic and therefore is not expected to interfere the spin Seebeck effect of the TbIG thin film | Pt heterostructures. On the other hand, there is a larger lattice mismatch between TbIG and YAG of $\epsilon_{YAG} = \frac{a_{YAG} - a_{TbIG}}{a_{TbIG}} = -3.5\%$.

The pre-charecterization of the TbIG (72.8 nm) | Pt (4.1 nm) heterostructure on a YAG substrate using X-ray diffraction (see Fig. B.0.7) reveals a very high crystalline quality of the TbIG thin film despite of the large lattice mismatch. Furthermore, an almost fully relaxed growth is detected with the TbIG thin film reflection close to the bulk reflection of TbIG. Subsequently, the sample is used for FD-SSE experiments with the main results around the critical temperatures shown in Fig. 5.3.5.

The transverse thermal voltage signal $V_{\mathrm{therm,trans}}$ shows the expected hysteresis curve of the spin Seebeck effect at high temperatures (see Fig. 5.3.5 (d)-(f)) with the inversion of the hysteresis at $T_{\mathrm{sign,2}} = (256 \pm 5)\,\mathrm{K}$ close to $T_{\mathrm{comp}} = 250.5\,\mathrm{K}$. At lower temperatures ($T_{\mathrm{Pt}} < 154\,\mathrm{K}$), this sample shows a strong linear component ($V_{\mathrm{therm,trans}} \propto H$) analogously to the previously discussed TbIG thin film | Pt heterostructure, which is fabricated on a GGG substrate. Also the remanent SSE amplitude decreases whereas the slope of the linear component increases with decreasing temperatures such that for $T_{\mathrm{Pt}} < 48\,\mathrm{K}$ the hysteresis in $V_{\mathrm{therm,trans}}$ is not resolvable (see Fig. 5.3.5 (a)-(c)). Overall, these effects are identical for the two different TbIG thin film | Pt heterostructures grown on the two different substrates (GGG, YAG) in this work, which suggests that the origin of this behavior is originating from the TbIG thin film | Pt heterostructures itself.

The longitudinal thermal voltage signal $V_{\mathrm{therm,long}}$ shows no signal above the noise level at all temperatures. This matches the expectation since the signal of the spin Seebeck effect is suppressed by geometry ($V_{\mathrm{therm,long}} \propto (\mathbf{J}_{\mathrm{S}} \times \mathbf{s}) \cdot \hat{\mathbf{x}} = 0$). In contrast to this experiment, the experiment conducted with the TbIG thin film | Pt heterostructure on the GGG substrate reveals a large SSE-signal in $V_{\mathrm{therm,long}}$ (see Fig. 5.3.2 (c)-(f)). The main geometrical difference between the two samples is the orientation of the Hall-bar mesa-structure ($\mathbf{J} \parallel [110]$ for TbIG | Pt on YAG, $\mathbf{J} \parallel [111]$ for TbIG | Pt on GGG) which could be the reason for this observation. To clarify this behavior, further FD-SSE experiments of TbIG | Pt heterostructures on GGG with $\mathbf{J} \parallel [110]$ have to be conducted. These experiments could point to different magnetic anisotropies in TbIG thin films compared to bulk TbIG.

The transverse resistive voltage $V_{\mathrm{res,trans}}$ shows a hysteretic behavior up to $\mu_0 H = 7\,\mathrm{T}$ at low temperatures (see red symbols in Fig. 5.3.5 (a),(b)). The well separated double dip structure indicates a large coercive field and large remanent magnetization, which is also found for the previously discussed TbIG thin film | Pt heterostructure on GGG (see also Fig. B.0.4). Overall, the signature observed in $V_{\mathrm{res,trans}}$ at low temperatures differs from the TbIG | Pt heterostructure on GGG, whereas it matches for $T_{\mathrm{Pt}} > 105\,\mathrm{K}$. A possible reason for the difference only at low temperatures might be the different crystallographic orientation of the Hall-bar mesa-structure, since the strength of the anisotropy in TbIG increases strongly at low temperatures [45]. The origin of the magnetoresistive effect, scaling with the external magnetic field H cannot be found within this experiment. For further investigation of this property, an FD-SSE experiment using a TbIG thin film | Pt heterostructure on a (110)-oriented YAG substrate with $\mathbf{J} \parallel [111]$ has to be conducted. The resistive longitudinal voltage signal $V_{\mathrm{res,long}}$ shows no proper signals which can be used for a detailed analysis. The reason for this is the large susceptibility of $V_{\mathrm{res,long}}$ to small temperature changes which occurred during the performed measurements. Thus, only the transverse resistive voltage signal $V_{\mathrm{res,trans}}$, which is less susceptible to temperature changes could be analyzed.
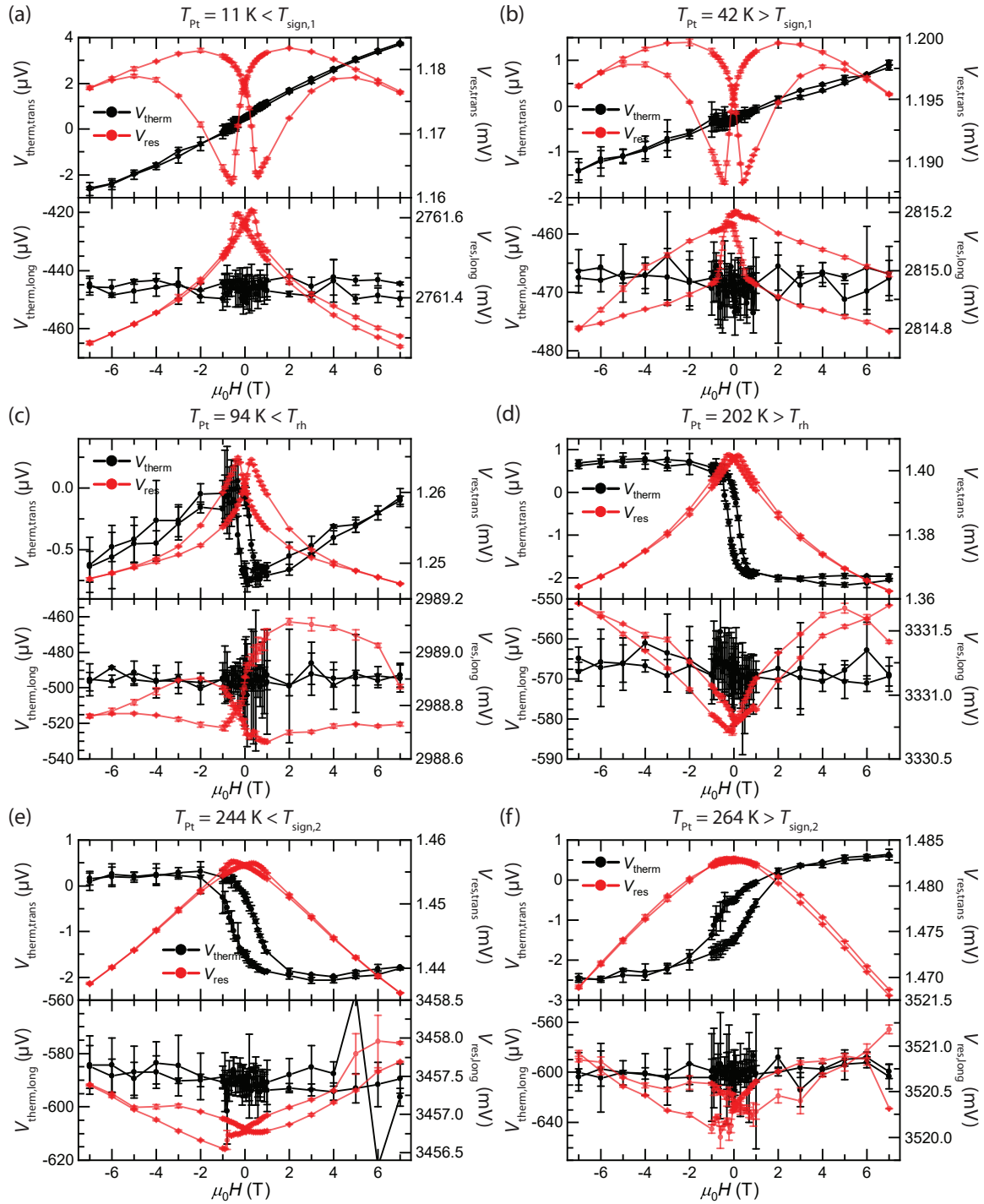
Figure 5.3.5.: Thermal (black) and resistive (red) voltage signals measured transverse (upper panels) and longitudinal (lower panels) to the current direction within the FD-SSE experiment using a TbIG $(72.8\,\text{nm})$ | Pt $(4.1\,\text{nm})$ heterostructure fabricated on a (100)-oriented YAG substrate. The data shown here is measured around the critical temperatures of bulk TbIG $(T_{\text{sign},1,\text{bulk}} = (36 \pm 3)\,\text{K}, T_{\text{rh}} \approx 190\,\text{K}, T_{\text{sign},2,\text{bulk}} = (255 \pm 5)\,\text{K})$. (a),(b) Large linear component in the transverse thermal voltage $V_{\text{therm,trans}} \propto H$ dominating the signal. Additionally, the hysteresis can not be resolved for $T_{\text{Pt}} < 48\,\text{K}$ such that the temperature of the first sign change $T_{\text{sign},1}$ is strongly field-dependent. (c),(d) The slope of the linear component decreases whereas remanent SSE amplitude of $V_{\text{therm,trans}}$ increases with increasing temperatures. For $T_{\text{Pt}} > 105\,\text{K}$, the field-dependence of $V_{\text{res,trans}}$ is similar to that of the TbIG thin film | Pt heterstructure fabricated on a GGG substrate. (e),(f) Inversion of the hysteresis in $V_{\text{therm,trans}}$ at $T_{\text{sign},2}$ due to reorientation of the sublattice magnetizations above the magnetic compensation temperature.

From the FD-SSE experiment, the SSE-amplitude $V_{\mathrm{SSE}}(T_{\mathrm{Pt}})$ is extracted and shown in Fig. 5.3.6. The resulting $V_{\mathrm{SSE}}(T_{\mathrm{Pt}})$-diagram for the TbIG thin film (72.8 nm) | Pt (4.1 nm) heterostructure fabricated on a (100)-oriented YAG substrate shows similar properties than the $V_{\mathrm{SSE}}(T_{\mathrm{Pt}})$-diagram for the TbIG thin film | Pt heterostructure fabricated on the (110)-oriented GGG substrate (see Fig. 5.3.3). Analogously, the temperature of the first gradual low temperature sign change $T_{\mathrm{sign,1}}$ is strongly field-dependent. The observed low temperature sign change is mainly influenced by the linear component $V_{\mathrm{SSE}} \propto H$. The second, abrupt sign change $T_{\mathrm{sign,2}} = (256 \pm 5)$ K matches the second sign change in $V_{\mathrm{SSE}}(T_{\mathrm{Pt}})$ of the TbIG single crystal | Pt heterostructure $T_{\mathrm{sign,2,bulk}} = (255 \pm 5)$ K within the error range. In total, the FD-SSE experiment using the TbIG thin film | Pt heterostructure grown on a (100)-oriented YAG substrate reveals a similar behavior compared to the FD-SSE experiment using a TbIG | Pt heterostructure on (110)-oriented GGG substrate. Therefore, the different FD-SSE signatures of TbIG thin film | Pt heterostructures compared to TbIG single crystal | Pt heterostructures is not related to the substrate material and is caused by the TbIG thin film | Pt heterostructure itself.
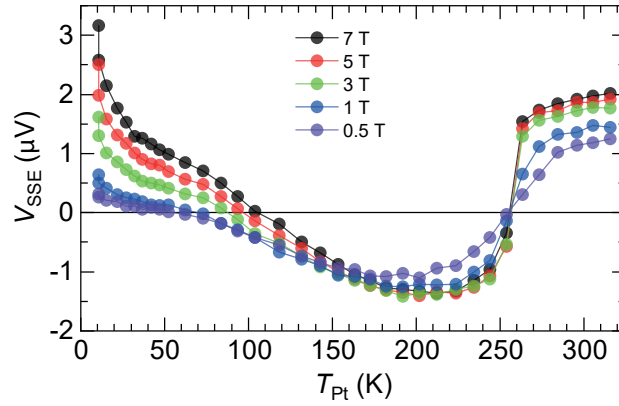
Figure 5.3.6.: $V_{\mathrm{SSE}}(T_{\mathrm{Pt}})$-diagram for the TbIG (72.8 nm) | Pt (4.1 nm) heterostructure fabricated on a (100)-oriented YAG substrate. Qualitatively, the temperature and field-dependence of the SSE amplitude is in agreement with that of the TbIG thin film | Pt heterostructure fabricated on a (110)-oriented GGG substrate (see Fig. 5.3.3). This demonstrates that the different FD-SSE in TbIG thin film | Pt heterostructures compared to TbIG single crystal | Pt heterostructures is not related to the substrate.

5.4. Summary - Spin Seebeck effect in $Tb_3Fe_5O_{12}$|Pt heterostructures

This chapter discussed the results of field-dependent spin Seebeck experiments using $Tb_3Fe_5O_{12}$ | Pt heterostructures. In the first part, the resistive and thermal voltage signals extracted from these FD-SSE experiments using a (110)-oriented $Tb_3Fe_5O_{12}$ single crystal | Pt heterostructure are discussed. From these measurements, the SSE-amplitude $V_{\mathrm{SSE}}(T_{\mathrm{Pt}})$ as a function of temperature and magnetic field is determined and correlated to the experimentally verified spin wave dispersion relation of TbIG. This successfully demonstrates that the spin Seebeck effect provides a powerful investigation technique for fundamental magnon properties.

The second part of this chapter discussed the spin Seebeck effect in $Tb_3Fe_5O_{12}$ thin film | Pt heterostructures, which exhibit major differences in particular at low temperatures ($T_{Pt} < 120\,K$). In this temperature range, the FD-SSE experiments reveal a component of $V_{therm,trans}$ linearly depending on the magnetic field. Furthermore, for $T_{Pt} < 50\,K$, the SSE-hysteresis could not be resolved. To address those differences several experimental attempts are conducted, which so far could not reveal the origin for those findings. However, these experiments reveal that TbIG thin films might not exhibit a rhombohedral phase transition. Furthermore, the origin of the differing results of FD-SSE esperiments originates from the $Tb_3Fe_5O_{12}$ | Pt heterostructure itself and is not related to the substrate material.

5.5. Outlook - Investigation of interface alloying in $Tb_3Fe_5O_{12}$ thin film|Pt heterostructures

Vasili *et al.* studied the effects of interface alloying on the spin Hall magnetoresistance in $CoFe_2O_4$ | Pt heterostructures by comparing the longitudinal magnetoresistance in samples with and without artificially induced interface alloying [46]. For a measurement geometry identical to the measurement geometry of $V_{res,long}$ within this work, the authors report a resistive longitudinal signal which is proportional to the applied magnetic field magnitude H of the alloyed sample. Furthermore, the total size of the magnetoresistive effect of the alloyed sample and exceeds the magnetoresistive effect of the sample without artificial interface alloying (see Fig. 5.5.1). The authors argue that in the special case of Pt, alloying at the interface can induce magnetic ordering within the alloyed interlayer due to the proximity of Pt to fulfilling the Stoner-criterion. This is supported by the observed anomalous hall effect in the sample with artificial alloying.

Since the field-dependent longitudinal resistive voltage $V_{res,long}$ of the TbIG thin film | Pt heterostructures investigated within this work shows a strong dependence on the applied magnetic field magnitude H at all investigated temperatures (see Figs. 5.3.2 and 5.3.5), an investigation of potential interface alloying might reveal the origin of the fundamental changes observed in TbIG thin film | Pt heterostructures compared to TbIG single crystal | Pt heterostructures. For further investigation of this property, X-ray absorption and magnetic circular dichroism (XMCD) experiments together with supporting transport experiments with M_{TbIG} in out-of-plane direction on $Tb_3Fe_5O_{12}$ thin film | Pt heterostructures are a possible approach to this problem.
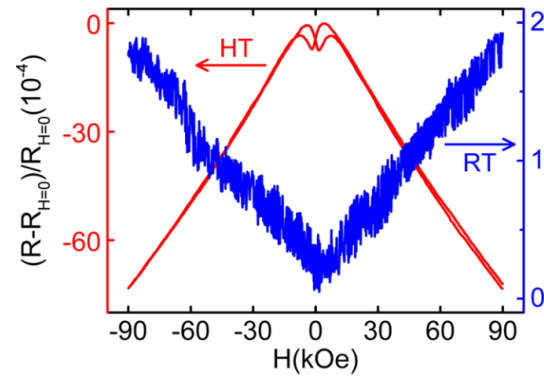
Figure 5.5.1.: Longitudinal magnetoresistance of a $CoFe_2O_4$ | Pt heterostructure with artificial alloying at the interface (HT) and without alloying at the interface (RT). A comparable behavior is observed within this work for the resistive longitudinal voltage $V_{res,long}$ in field-dependent experiments with TbIG thin film | Pt heterostructures. Figure taken from Ref. [46].

6. Summary and outlook

In the framework of this thesis, the relation between the spin Seebeck effect and the spin wave dispersion relation is investigated. The verification of this correlation would consequently propose the spin Seebeck effect as a probe for the spin wave dispersion relation in magnetically ordered insulators. Accordingly, this would allow to measure the key properties of spin wave dispersion relations of a wide range of material systems and nanostructures by simple electric transport experiments. To reveal the relation between the spin Seebeck effect and the spin wave dispersion relation, inelastic neutron scattering with polarization analysis at temperatures between $10\,\mathrm{K}$ and $280\,\mathrm{K}$ is carried out. Subsequently, the spin wave dispersion relation is refined to the experimental data using the software package SpinW. Finally, the thus obtained spin wave dispersion relation is connected to the temperature profile of the amplitude of the spin Seebeck effect. To this end, the compensated ferrimagnetic insulator $Tb_3Fe_5O_{12}$ (TbIG) is used as a showcase material system. In the remainder of this section, the fundamental properties of TbIG are recapped to subsequently highlight the key experimental results which are achieved within this work. In conclusion, an outlook on future investigations in context with the spin Seebeck effect and its connection to the spin wave dispersion relation is given.

TbIG is a compensated ferrimagnetic insulator consisting of three antiferromagnetically coupled magnetic sublattices $\mathbf{M}_{\mathrm{Tbc}}$, $\mathbf{M}_{\mathrm{Fea}}$ and $\mathbf{M}_{\mathrm{Fed}}$ with a Néel temperature of $T_{\mathrm{N}} \approx 550\,\mathrm{K}$ [25]. Below $T_{\mathrm{rh}} \approx 190\,\mathrm{K}$, the unit cell of TbIG distorts from a cubic bcc-lattice to a rhombohedral crystal structure [23]. Additionally, the collinear ferrimagnetic structure gradually transforms into the 'double-umbrella' magnetic structure below $T_{\mathrm{du}} \approx 160\,\mathrm{K}$ by tilting the magnetic moments of the Tb-sublattice $\mathbf{M}_{\mathrm{Tbc}}$ away from the magnetically easy $[111]_{\mathrm{bcc}}$-direction while the orientation of the total Tb-sublattice magnetization remains unchanged ($\mathbf{M}_{\mathrm{Tbc}} \parallel [111]_{\mathrm{bcc}}$) [33]. The cubic magnetic anisotropy of TbIG with the magnetic easy axes along the $[111]_{\mathrm{bcc}}$-directions becomes extraordinarily large at temperatures below T_{rh} [45]. Furthermore, the coupling of the magnetic Tb-sublattice $\mathbf{M}_{\mathrm{Tbc}}$ to the two Fe-sublattices $\mathbf{M}_{\mathrm{Fea}}$ and $\mathbf{M}_{\mathrm{Fed}}$ is considerably weak, which results in a strong temperature dependence of the remanent Tb-sublattice magnetization $\mathbf{M}_{\mathrm{Tbc}}$. Due to the configuration of the sublattice magnetizations, this leads to magnetic compensation where the total remanent magnetization of TbIG vanishes at the magnetic compensation temperature $T_{\mathrm{comp}} = 250.5\,\mathrm{K}$. When the compensation temperature is crossed in finite external magnetic fields, an inversion of all remanent sublattice magnetizations occurs.

6.1. Inelastic neutron scattering with polarization analysis on a Tb$_3$Fe$_5$O$_{12}$ single crystal

The inelastic neutron scattering experiment with polarization analysis on a TbIG single crystal is able to track the first optical and second optical mode of the spin wave dispersion relation of TbIG at $10\,$K, $100\,$K and $280\,$K. Both optical modes are fully chiral with opposite chiralities and shift downwards in energy with increasing temperatures due to the strong temperature dependence of the Tb-sublattice magnetization $\mathbf{M}_{\mathrm{Tbc}}$. Furthermore, the chirality of both optical modes is inverted at $280\,$K compared to $100\,$K and $10\,$K because of the crossing of the magnetic compensation temperature $T_{\mathrm{comp}} = 250.5\,$K. The obtained experimental spin wave dispersion relations are the basis of the simulation of spin wave dispersion relations of TbIG with SpinW in the following step.

6.2. Simulation of the spin wave dispersion relation of Tb$_3$Fe$_5$O$_{12}$ with SpinW

After the successful verification of SpinW as a simulation tool for spin wave dispersion relations in complex compensated ferrimagnetic insulators by reproducing the spin wave dispersion relations of Y$_3$Fe$_5$O$_{12}$ and Gd$_3$Fe$_5$O$_{12}$ from literature, the spin wave dispersion relation of TbIG is successfully simulated. In particular, the simulated spin wave dispersion relations of TbIG at $280\,$K, $100\,$K and $10\,$K are refined in such a way that a good agreement to the experimentally determined spin wave dispersion relations by inelastic neutron scattering with polarization analysis at respective temperatures is obtained. With this, a full set of parameters is gained to describe the magnetic structure of TbIG in the temperature range from $10\,$K to $280\,$K. Furthermore, the simulated spin wave dispersion relations reveal that with increasing opening angles θ and θ' of the magnetic 'double-umbrella' structure describing the Tb-moments, the acoustic mode transforms from a state with single chirality to a state with mixed chirality around the Γ-point. Especially at $10\,$K, where the opening angles θ and θ' reach their maximum, all modes of the spin wave dispersion relation have an energy gap at the Γ-point which is related to the pronounced magnetic double-umbrella structure. Additionally, the investigation of the temperature dependent spin wave dispersion relation of TbIG reveals that at $T_{\mathrm{cross}} = 70\,$K, the thermal energy is equal to the energy gap of the first optical mode E_{gap} at the Γ-point ($E_{\mathrm{gap}}(T_{\mathrm{cross}}) = k_{\mathrm{B}}T_{\mathrm{cross}}$). After the successful simulation of the spin wave dispersion relation of TbIG, the next step towards the verification of the relation to the temperature profile of the spin Seebeck effect is the investigation of the spin Seebeck effect in TbIG|Pt heterostructures.

6.3. Spin Seebeck effect in Tb$_3$Fe$_5$O$_{12}$|Pt heterostructures

In a first step, field-dependent spin Seebeck effect (FD-SSE) experiments using a (110)-oriented TbIG single crystal|Pt heterostructure are carried out. The extracted temperature dependent spin Seebeck effect amplitude $V_{\mathrm{SSE}}(T_{\mathrm{Pt}})$ shows two characteristic sign changes at $T_{\mathrm{sign,1}} = (36 \pm 3)\,$K and $T_{\mathrm{sign,2}} = (255 \pm 5)\,$K. The first, gradual sign change at

$T_{\mathrm{sign},1} = (36 \pm 3)\,\mathrm{K}$ is related to the population of the first optical mode with negative chirality opposite to the acoustic mode. Compared to the predicted temperature $T_{\mathrm{cross}} = 70\,\mathrm{K}$, the first sign change is found at lower temperatures which is most likely originating from the mixed chirality of the acoustic mode below $T_{\mathrm{du}} \approx 160\,\mathrm{K}$. The second sign change $T_{\mathrm{sign},2} = (255 \pm 5)\,\mathrm{K}$ is related to the magnetic compensation temperature $T_{\mathrm{comp}} = 250.5\,\mathrm{K}$, where all magnetic sublattices and thus all spin wave chiralities invert in a finite external magnetic field. In total, the experimentally verified spin wave dispersion relations at $280\,\mathrm{K}$, $100\,\mathrm{K}$ and $10\,\mathrm{K}$ are conclusively connected to the temperature profile of the spin Seebeck effect amplitude $V_{\mathrm{SSE}}(T_{\mathrm{Pt}})$ of TbIG single crystal | Pt heterostructures. This strong relation proposes the spin Seebeck effect as a powerful investigation technique for magnon properties.

Additionally, the spin Seebeck effect in TbIG thin film | Pt heterostructures is investigated. TbIG thin films offer a further simplification of the sample fabrication and are an important step towards spintronic devices. However, the spin Seebeck effect in TbIG thin film | Pt heterostructures reveals major differences compared to that of TbIG single crystal | Pt heterostructures. In particular at low temperatures $T_{\mathrm{Pt}} < 120\,\mathrm{K}$, the spin Seebeck effect amplitude exhibits a component linearly depending on the applied magnetic field whereas the hysteresis of the spin Seebeck effect can not be resolved for $T_{\mathrm{Pt}} < 50\,\mathrm{K}$. To investigate the origin of those differences, resonant elastic X-ray scattering experiments are conducted. These experiments reveal that the TbIG thin films might not exhibit a rhombohedral distortion at low temperatures. Furthermore, the spin Seebeck effect in TbIG thin film | Pt heterostructures on different substrates is investigated. From these experiments, no correlation of the spin Seebeck effect with the substrate materials is found.

6.4. Outlook

Despite the various experiments carried out during this thesis, some issues remain unsolved. Since so far the acoustic modes and the flat bands at $E < 5\,\mathrm{meV}$ in the spin wave dispersion relation of TbIG are not confirmed by inelastic neutron scattering with polarization analysis, the experimental verification of those bands should be subject to future inelastic neutron scattering experiments. In particular, the verification of the mixed chirality in vicinity of the Γ-point at low energies is an important objective.

Additionally, the inelastic neutron scattering experiment revealed two flat bands at $10\,\mathrm{K}$ which are not observed at $100\,\mathrm{K}$ and $280\,\mathrm{K}$. These bands are of unknown origin and could not be simulated with SpinW. Investigating the temperature dependence of those bands could probably reveal their origin. Kang *et al.* reported for the similar material system $\mathrm{Dy_3Fe_5O_{12}}$ indications of magnetic ordering of the magnetic Dy-sublattice below $16\,\mathrm{K}$ [47]. This motivates further investigations of the inter-sublattice magnetic ordering of the Tb-moments in TbIG by e.g. AC-magnetometry measurements. In $\mathrm{Dy_3Fe_5O_{12}}$, the magnetic ordering of the Dy-sublattice leads to many additional bands for $T < 16\,\mathrm{K}$. Analogously, a possible ordering of the Tb-sublattice might be a reason for the flat bands observed by inelastic neutron scattering on TbIG at $10\,\mathrm{K}$.

The field-dependent spin Seebeck experiments using TbIG thin film | Pt heterostructures revealed major differences to TbIG single crystal | Pt heterostructures which could not be explained so far. The resistive longitudinal voltage $V_{\text{res,long}}$ of the TbIG thin film | Pt heterostructures exhibits a strong field-dependence which might be originating from alloying at the TbIG | Pt interface. Therefore, investigations on possible alloying at the TbIG | Pt interface by X-ray absorption and magnetic circular dichroism (XMCD) experiments could reveal the origin of the observed deviations in TbIG thin film | Pt heterostructures.

Overall, this work successfully verified the relation between the spin wave dispersion relation and the temperature dependent spin Seebeck effect amplitude. Thus, the development of a simulation tool for calculating a refinement of the temperature dependent spin Seebeck effect amplitude, analogouysly to e.g. Rietveld refinement in X-ray or neutron powder diffraction, could establish the spin Seebeck effect as investigation technique for spin wave dispersion relations in magnetically ordered insulators in the future.

A. Appendix - Experimental methods

The first part of this chapter focuses on the fabrication of the $Tb_3Fe_5O_{12} \,|\, Pt$ thin film heterostructures and the used experimental techniques. The samples are fabricated by pulsed laser deposition (PLD) and subsequent electron beam evaporation (EVAP). In the second part of this chapter, the used investigation techniques, X-ray diffraction (XRD) and SQUID-magnetometry, are outlined. These techniques are used to characterize the magnetic and structural properties of the fabricated samples.

A.1. Fabrication of $Tb_3Fe_5O_{12}$ thin film|Pt heterostructures

A.1.1. Substrate preparation

The first step in the fabrication of a $Tb_3Fe_5O_{12}$ thin film | Pt (TbIG | Pt) heterostructure is the deposition of a Pt thin film ($d \approx 180\,\mathrm{nm}$) on the backside of the substrate. For this purpose, the substrate is inserted inside a high vacuum sputtering device, where the Pt thin film is sputtered on the backside of the substrate. The Pt thin film on the backside is mandatory for a high and homogeneous absorption of infrared laser light, which is used to heat the substrate during the pulsed laser deposition process.

A.1.2. Ultra high vacuum cluster

After the substrate preparation, the substrate is inserted into the load-lock of the ultra-high vacuum (UHV) deposition cluster (see Fig. A.1.1). The UHV cluster consists of five chambers: load-lock, transfer chamber, PLD chamber, EVAP chamber and sputtering chamber. The pressure of the UHV cluster is in the low $10^{-9}\,\mathrm{mbar}$ region, which enables the fabrication of high purity epitaxially grown thin film heterostructures with high quality interfaces. Due to the connection of all chambers to the transfer chamber, multiple processes can be conducted without breaking the vacuum ('in-situ') by transferring the sample with a transfer arm. During deposition, the chambers are separated by a plate valve which minimizes contamination of the UHV cluster. Within this work the sputtering chamber is not used.
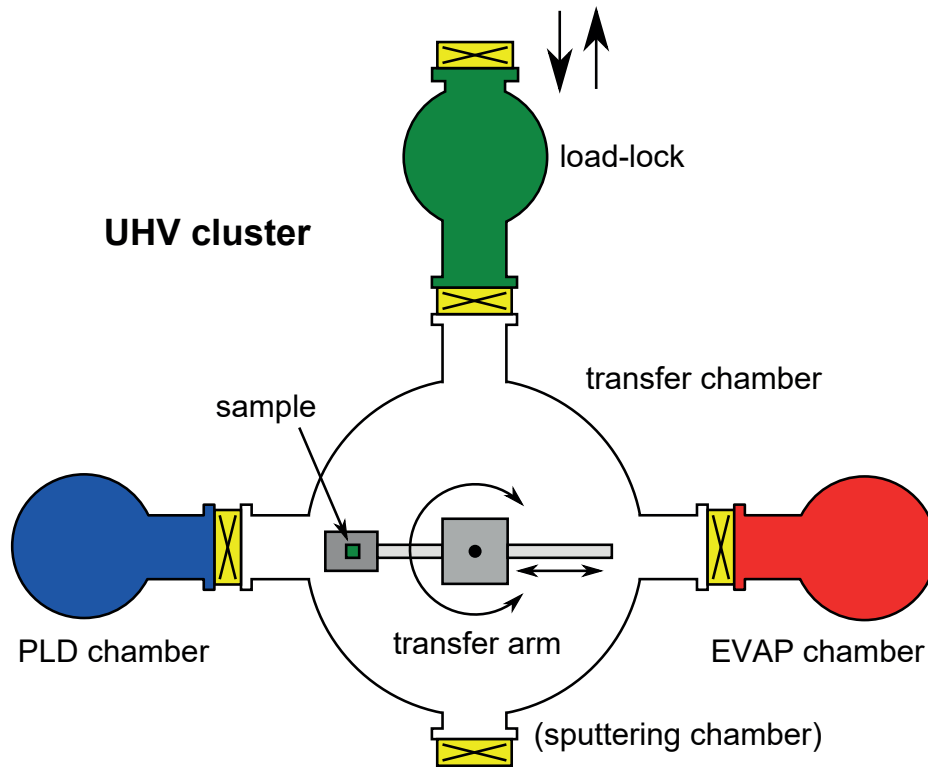
Figure A.1.1.: Schematic drawing of the ultra-high vacuum (UHV) cluster, which is used for epitaxial thin film fabrication. The samples are inserted into the load-lock and can be transferred into the pulsed laser deposition (PLD) chamber, the electron beam evaporation (EVAP) chamber and the sputtering chamber with a transfer arm. This allows an overall 'in-situ' fabrication of thin film heterostructures which is mandatory for high quality samples. The sputtering chamber is not used within this work. Figure taken from Ref. [48].
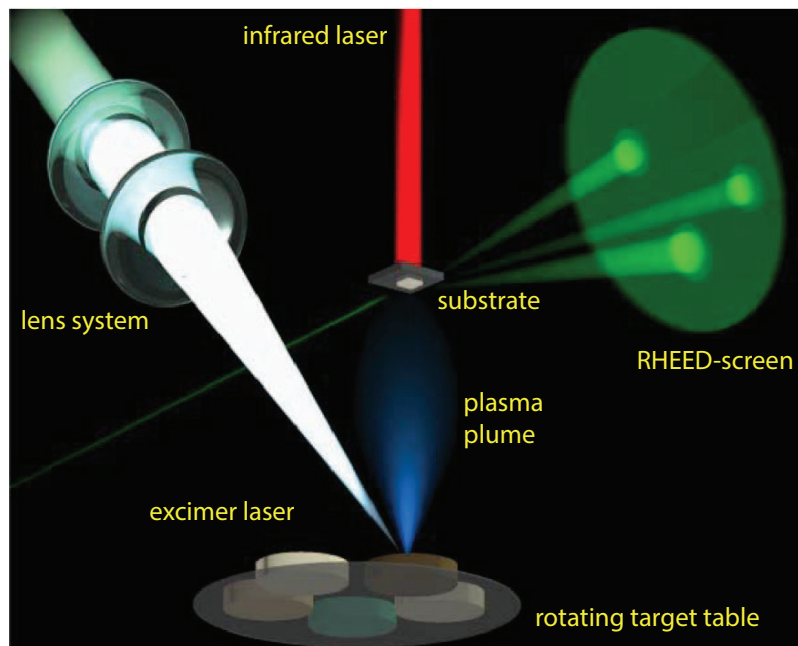
A.1.3. Pulsed laser deposition (PLD)

Within this work, the crystalline epitaxially grown $Tb_3Fe_5O_{12}$ thin films are fabricated by pulsed laser deposition (PLD). The PLD process is conducted inside the PLD-chamber of the UHV-cluster allowing the production of a high quality $Tb_3Fe_5O_{12}$ thin film. A schematic drawing of the PLD-process is shown in Fig. A.1.2.

The pulsed laser deposition is a fabrication technique for high quality mono-crystalline thin films, which are epitaxially grown on mono-crystalline substrates. For the fabrication of a thin film, the pulsed UV-excimer-laser (KrF, $248\,nm$) hits a target material, which ionizes into a plasma plume. The target material is a poly-crystalline pellet with an atomic composition equal to the stoichiometry of the fabricated thin film. Within the plasma plume, the ionized atoms and molecules diffuse towards the substrate where they get adsorbed. Due to the automatic lens system, the energy density per pulse at the target surface ρ_L can be adjusted. Within this work, the energy density per pulse is kept constant at $\rho_L = 2\,J/cm^2$. During the deposition process, the substrate is heated at a constant temperature T_S by an infrared laser. The infrared laser is heating the substrate from the backside, where the temperature is monitored by a pyrometer. To ensure a constant substrate temperature the pyrometer adjusts the power of the infrared laser via a feedback-loop. A properly adjusted constant substrate temperature T_S is mandatory to provide the surface activation energy

for high quality two-dimensional crystalline thin film growth. The PLD-process is conducted within a gas atmosphere with pressure p_x. For the adjustment of the pressure p_x, the inward gas flow is set. The system subsequently adjusts the position of the plate valve in front of the turbomolecular pump, which controls the outward gas flow, to establish the gas atmosphere at constant pressure p_x. The gas atmosphere reduces the kinetic energy of the ionized particles by scattering prior to adsorption by the substrate. Within this work oxygen with a pressure p_{O2} is used to avoid oxygen vacancies within the $Tb_3Fe_5O_{12}$ thin film.

Additionally, the PLD-system is equipped with a RHEED-setup (reflection high-energy electron diffraction). The RHEED allows growth monitoring during the process by analyzation of a scattering scheme. The scattering scheme is produced by an electron beam, which is scattered at the sample surface and visualized on a scintillating RHEED-screen. By analysis of the intensity of the scattered electron beam with a camera, the type of growth and the number of adsorbed mono-layers is observable during the deposition process. The RHEED-setup is not used within this work.

Figure A.1.2.: Schematic drawing of the pulsed laser deposition. During the deposition process an UV-excimer-laser hits a stoichiometric target, which produces a plasma plume consisting of ionized atoms. The ionized atoms are adsorbed by the substrate material. To provide the surface activation energy for a two-dimensional crystalline growth, the substrate is heated from the backside by an infrared laser. The RHEED-setup allows to in-situ monitor the deposition process. Figure taken from Ref. [48].

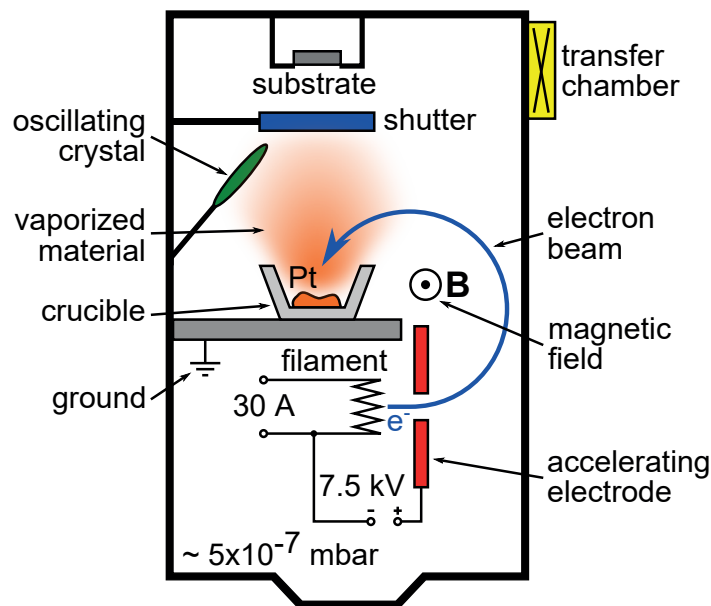## A.1.4. Electron beam evaporation (EVAP)

The electron beam evaporation (EVAP) is a fabrication technique for most metallic thin films by vapor deposition, which is used within this work. A schematic drawing of the EVAP-chamber during the deposition process is shown in Fig. A.1.3.

The material, which is deposited during the process, is placed under the sample within a

crucible. Subsequently, the material is targeted by an electron beam and being heated up to its evaporation temperature. The electrons for the electron beam are originating from a filament by thermionic emission, which therefore is heated with a filament current of $30\,A$. After the thermionic emission, the electrons are accelerated by an acceleration voltage of $7.5\,kV$ and deflected by a magnetic field, such that the electron beam hits the material within the crucible.

For the determination of the deposition rate a piezoelectric oscillating quartz crystal is installed below the shutter. Due to deposition of the quartz crystal, the resonance frequency decreases which allows to determine the deposition rate at the substrate position taking geometrical factors into account. When the set deposition rate is reached and stabilized, the shutter is opened until the set thin film thickness is deposited onto the substrate. Nevertheless, the quartz crystal provides only an estimation of the deposited layer thickness. Thus, for proper measurement of the thickness of the metallic layer, a reflectometry measurement using X-ray diffractometry (see section A.2.1) has to be conducted.

Within this work, the EVAP-chamber is used to fabricate 'in-situ' Pt-thin films on top of $Tb_3Fe_5O_{12}$. Due to the soft deposition process, compared to e.g. sputtering, interdiffusion at the $Tb_3Fe_5O_{12}\,|\,Pt$ heterostructures is suppressed.


Figure A.1.3.: Schematic drawing of the electron beam evaporation chamber (EVAP), which is used to fabricate metallic thin films. The electron beam, which is generated by thermionic emission from the filament and subsequent acceleration by the acceleration voltage is deflected by a magnetic field to hit the material, which is deposited. Due to exposure to the electron beam, the material is vaporized. The vapor is then adsorbed by the substrate, when the set and stable deposition rate is reached and the shutter is opened. The oscillating quartz crystal allows to determine the deposition rate and therefore the thickness of the fabricated metallic thin film. Figure taken from Ref. [48].

A.2. Investigation techniques

The next step, after the fabrication of the samples is the structural investigation by X-ray diffractometry, which is discussed in the first part of this section. The second part focuses on SQUID-magnetometry, which is an important tool for the investigation of the magnetic properties of the sample.

A.2.1. X-ray diffraction

For the investigation of structural properties of the sample, X-ray diffraction is used within this work. The measurements are conducted with a Bruker AXS D8 Discover 4-axis diffractometer, which uses the monochromatic Cu-$K_{\alpha 1}$ X-ray with a wavelength of $\lambda = 1.5406\,\text{Å}$. The two axis used for the measurement (2θ, ω) are shown schematically in Fig. A.2.1 (a), whereas the other two axis are only used for alignment within this work. X-ray diffractometers allow to analyze an X-ray beam, which is scattered at the sample under an incident angle ω and analyzed under the total deflection angle 2θ. In the following, the fundamentals of X-ray diffraction are briefly summarized. Subsequently, the performed types of measurements are described.
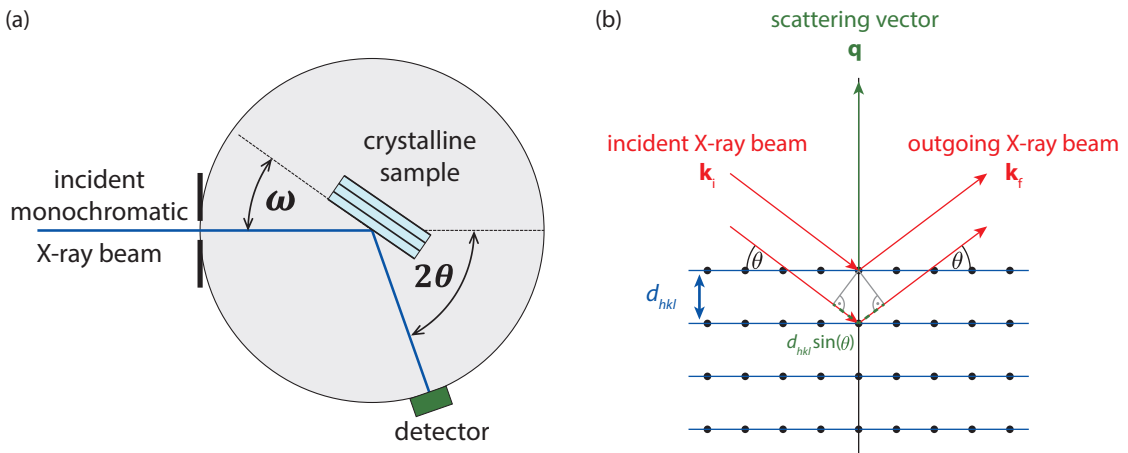
Figure A.2.1.: (a) Schematic drawing of a two axis X-ray-diffractometer with the two axis ω and 2θ. Here, the angle ω describes the angle which is drawn by the lattice planes and the monochromatic incident X-ray beam and the total deflection angle 2θ describes the position of the probed, outgoing X-ray beam. Figure taken from Ref. [43]. (b) Schematic drawing of elastic X-ray scattering, where the incident X-ray beam with wavevector $\mathbf{k}_i$ is scattered elastically at the lattice planes resulting in an outgoing X-ray beam with wavevector $\mathbf{k}_f$, where $|\mathbf{k}_i| = |\mathbf{k}_f|$. The total scattering process is described by the scattering vector $\mathbf{q} = \mathbf{k}_f - \mathbf{k}_i$. Bragg's law is fulfilled when $2d_{hkl}\sin(\theta) = \lambda$ (see Eq. (A.1)). Figure adapted from Ref. [49].

Since the wavelength of X-rays is in the range of atomic distances within crystals ($\approx$ Å), the atomic structure of the crystal acts as diffraction gating, which is leading to destructive and constructive interferences under distinct angles ω and 2θ. Thus, when the intensity of the scattered X-ray beam is measured as a function of the angles ω and 2θ, X-ray diffraction represents a powerful tool to obtain information about structural properties of the crystal

under investigation. Bragg's law provides the necessary measurement geometry for finding constructive interferences:

$$2d_{hkl}\sin(\theta) = \lambda\,. \tag{A.1}$$

Here, d_{hkl} is the distance of atomic layers in direction $[hkl]$, which is described by the Miller's indices h, k, l. Furthermore, θ, the half of the total deflection angle 2θ, is the angle between the incident beam and the atomic layer (see Fig. A.2.1 (b)). For crystals with cubic symmetry, as most of the rare-earth iron garnets, d_{hkl} is related to the cubic lattice constant a by the following relation:

$$d_{hkl} = \frac{a}{\sqrt{h^2 + k^2 + l^2}}\,. \tag{A.2}$$

Due to the structure factor of the rare-earth iron garnets, not all combinations (hkl) lead to constructive interferences. The first constructive interference in rare-earth iron garnets is found for the reflection, described by the Miller's indices (400). In the following, the conducted scan types together with their purpose are described:

- **2θ-ω-scan:** With the 2θ-ω-scan the intensity of the scattered X-rays along a fixed $\mathbf{q}$-direction with $\mathbf{q} \parallel (hkl)$ is measured. Therefore, the incident beam is penetrating the sample under the angle $\omega = \theta$, where the angle θ is drawn by the lattice planes (hkl) and the incident beam. The detector is aligned such that $2\theta = 2\omega$ during the scan. By keeping this constraint during the measurement and scanning the angle ω, an intensity scan along a fixed $\mathbf{q}$-direction is obtained (see Fig. A.2.1 (b)). Within this work, the scattering vector $\mathbf{q}$ is aligned parallel to the crystallographic direction pointing out of the sample plane.

  With this scan type, a characteristic peak structure is obtained, when Bragg's law for the crystalline substrate and the crystalline thin film is fulfilled. Thus, this measurement provides insight into the present crystalline phases within the sample together with the respective out-of-plane lattice constant.

  Due to the finite thickness of the multilayer structure, reflections at the surface and the interface of the sample lead to an additional scattering pattern in the vicinity of the Bragg-peaks, which is called Laue-oscillations. These Laue-oscillations or finite thickness fringes are similar to the optical Fraunhofer diffraction pattern caused by diffraction of a slit and indicate a coherent growth of the epitaxial thin films.

- **Reflectometry:** The reflectometry is a scan mode equal to the 2θ-ω-scan at small angles $2\theta < 5°$. Therefore, the sample is aligned such that the angle ω is drawn by the incident X-ray beam and the sample surface. During the measurement, the constraint $2\theta = 2\omega$ is fulfilled. With this procedure, a characteristic scattering pattern due to inference of the reflections at the surface and the interfaces of the heterostructure is obtained. Subsequently, the program Leptos is used to simulate the scattering pattern for a reflectometry measurement of an equal sample. The simulated reflectometry measurement is then refined to the data by adjusting the layer thicknesses and the roughness of the interfaces and the surface.

- **Rocking-curve:** For the rocking curve, ω and 2θ are aligned, such that Bragg's law is fulfilled for a set of Miller's indices (hkl). Then, ω is scanned, while 2θ remains at a

fixed value, which results in a peak structure. The shape of this peak together with the full width at half maximum are figures of merit for the mosaicity and therefore the crystalline quality of the sample.

Additional information on X-ray diffraction is given in Ref. [49].

A.2.2. SQUID-magnetometry

The magnetization measurements for the investigation of magnetic sample properties within this work are conducted with a SQUID-magnetometer by Quantum Design. The used SQUID-magnetometer, which is a vibrating sample magnetometer, allows the precise measurement of the total magnetization of the sample in external magnetic fields up to $\pm 7\,\text{T}$ at sample temperatures between $1.2\,\text{K}$ and $390\,\text{K}$. To this end, the magnetization is measured by an axial second order gradiometer as shown in Fig. A.2.2.
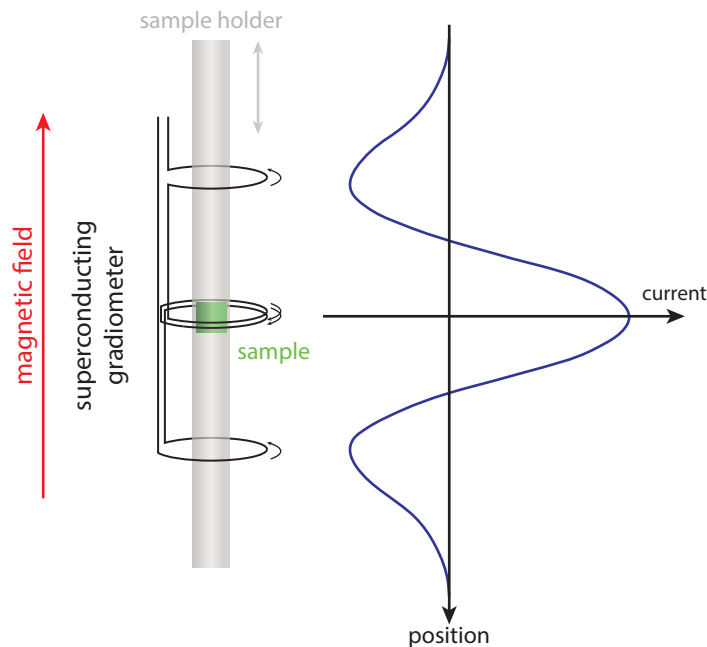

Figure A.2.2.: Schematic drawing of the gradiometer inside the SQUID-magnetometer. When the sample is moved through the gradiometer at a constant velocity, a superconducting current is induced within the gradiometer, which is according to Faraday's law proportional to the magnetization. A SQUID then transforms the current into a voltage signal. By measuring the voltage signal and subsequently fitting the obtained curve, the magnetization along the axis of the gradiometer is precisely determined. The magnetization can be measured under external magnetic fields of up to $\pm 7\,\text{T}$ and at sample temperatures between $1.2\,\text{K}$ and $390\,\text{K}$ with the used setup from Quantum Design. Figure adapted from Ref. [48].

For a precise measurement, the gradiometer consists of three superconducting coils, which are connected in series. The number of windings for the outer coils is (-1), whereas the number of windings of the middle coil is $(+2)$. Thus, when the sample is moved through the gradiometer at a constant velocity, a superconducting current is induced which is, according to Faraday's law, proportional to the change of the magnetic flux along the axis of the gradiometer (see Fig. A.2.2). Here, the axis of the gradiometer is equal to the direction of the external magnetic field. For the detection of the superconducting current,

it is transformed to a voltage by a RF-SQUID. Due to the serial connection of three superconducting coils, a fit to the raw data allows the precise determination of the samples magnetic moment. The voltage curve is automatically fitted by the software of the SQUID-magnetometer provided by Quantum Design, such that overall precise temperature dependent and field dependent magnetization measurements can be performed. Further information of the working principles of SQUID-magnetometers are provided in Ref. [50].
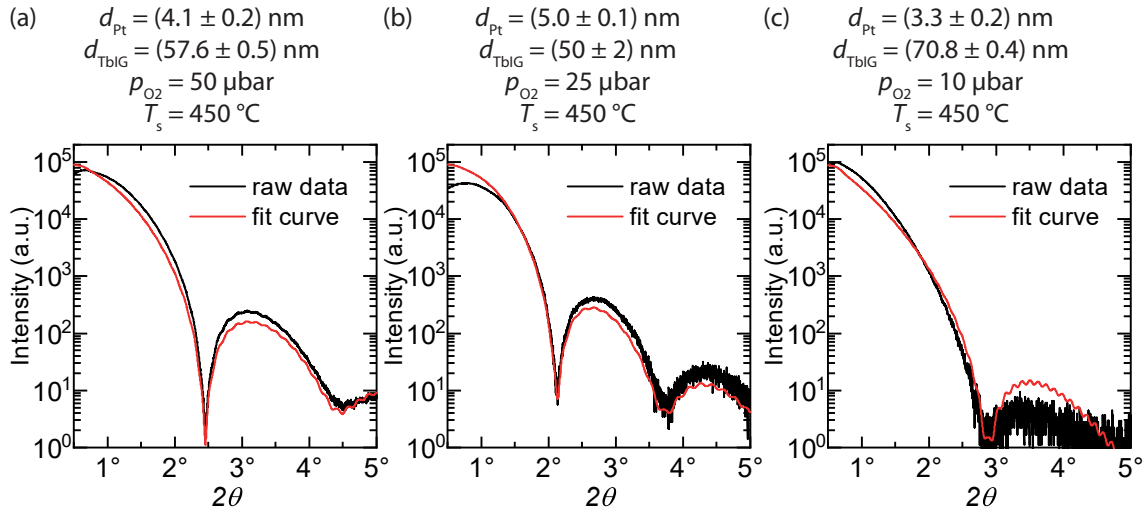
B. Appendix - Supplementary data
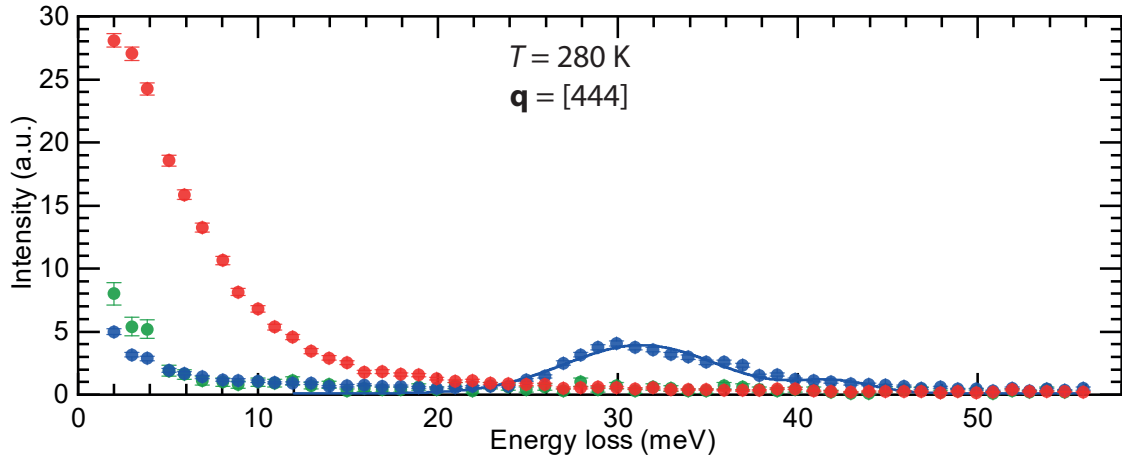
Figure B.0.1.: Inelastic neutron scattering with polarization analysis at $T = 280\,\mathrm{K}$. The color depicts the different scattering channels: non-spin-flip channel (green), spin flip channel with $i \cdot (S^{xy} - S^{yx}) < 0$ (blue) and $i \cdot (S^{xy} - S^{yx}) > 0$ (red). The intensity is normalized to the monitor counts and plotted as a function of the energy loss for $\mathbf{q} = [444]$, which is a Γ-point. The intensity is fitted with superposed Gaussian functions (solid lines). This data is equal to the data shown in Fig. 3.2.1 (a) but plotted with wider range on the intensity-axis, such that the pronounced red tail for $E < 15\,\mathrm{meV}$ is visible. This energy tail is considered as a data point with large error bar of a magnon mode, which is plotted in Fig. 3.2.1 (b).
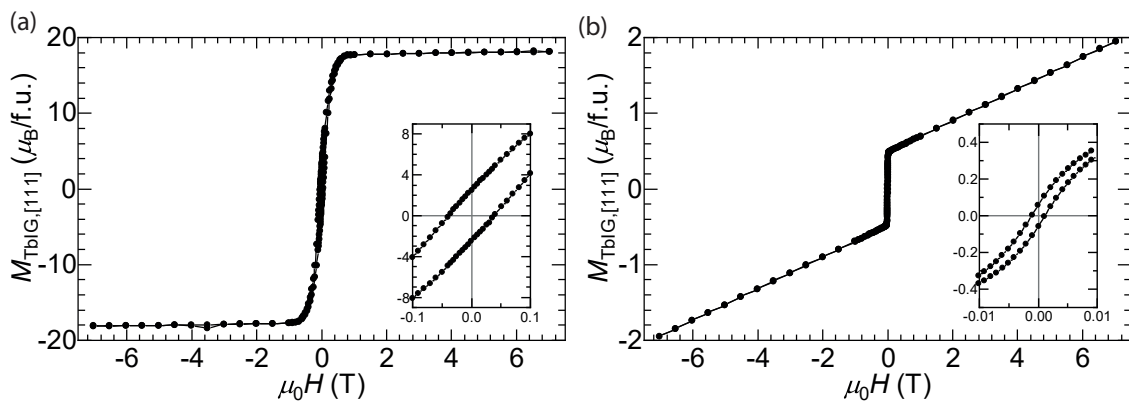
Figure B.0.2.: Field-dependent magnetization measurements $M(H)$ of a TbIG single crystal at $2\,\mathrm{K}$ (a) and at $300\,\mathrm{K}$ (b) with the external magnetic field applied along the cubic $[111]_{\mathrm{bcc}}$-direction. The magnetization is given in Bohr magnetons per formula unit of $\mathrm{Tb_3Fe_5O_{12}}$ ($\mu_{\mathrm{B}}/\mathrm{f.u.}$). The insets show the regions around $\mu_0 H = 0\,\mathrm{T}$ of the respective measurement. The $M(H)$-measurements reveal a narrow hysteresis loop with small coercive fields H_{c} and small relative remanent magnetizations $M_{\mathrm{r}}/M_{\mathrm{s}}$, where M_{s} is the saturated magnetization. The larger field dependence observed in the measurement at $300\,\mathrm{K}$ originates from the suppression of thermal excitations by an external magnetic field.

(a) $d_{Pt} = (4.1 \pm 0.2)$ nm   (b) $d_{Pt} = (5.0 \pm 0.1)$ nm   (c) $d_{Pt} = (3.3 \pm 0.2)$ nm
$d_{TbIG} = (57.6 \pm 0.5)$ nm $d_{TbIG} = (50 \pm 2)$ nm $d_{TbIG} = (70.8 \pm 0.4)$ nm
$p_{O2} = 50$ µbar $p_{O2} = 25$ µbar $p_{O2} = 10$ µbar
$T_s = 450$ °C $T_s = 450$ °C $T_s = 450$ °C

Figure B.0.3.: Reflectometry measurements on TbIG thin film ǀ Pt heterostructures grown on (110)-oriented GGG substrates which are used for spin Seebeck effect experiments within this work. The experimental data (black curve) is plotted together with the LEPTOS-simulation (red curve). The extracted simulation parameters are shown on top of the respective measurement together with the main fabrication parameters (substrate temperature T_s and oxygen pressure p_{O2}).
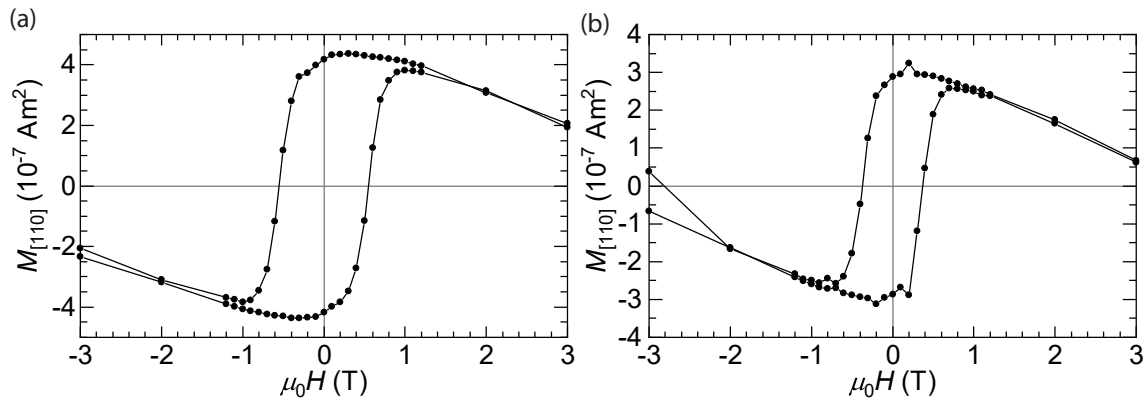

Figure B.0.4.: Field-dependent magnetization measurements $M(H)$ of a TbIG thin film ǀ Pt heterostructure grown on a (100)-oriented $Y_3Al_5O_{12}$ substrate at a sample temperature of $10\,K$ (a) and $50\,K$ (b) with the external magnetic field applied along the cubic $[110]_{bcc}$-direction. The $M(H)$-measurements show a large coercive field H_c and a large relative remanent magnetization M_r/M_s, whereas the coercive field and the relative remanent magnetization are small in TbIG single crystals (see Fig. B.0.2).
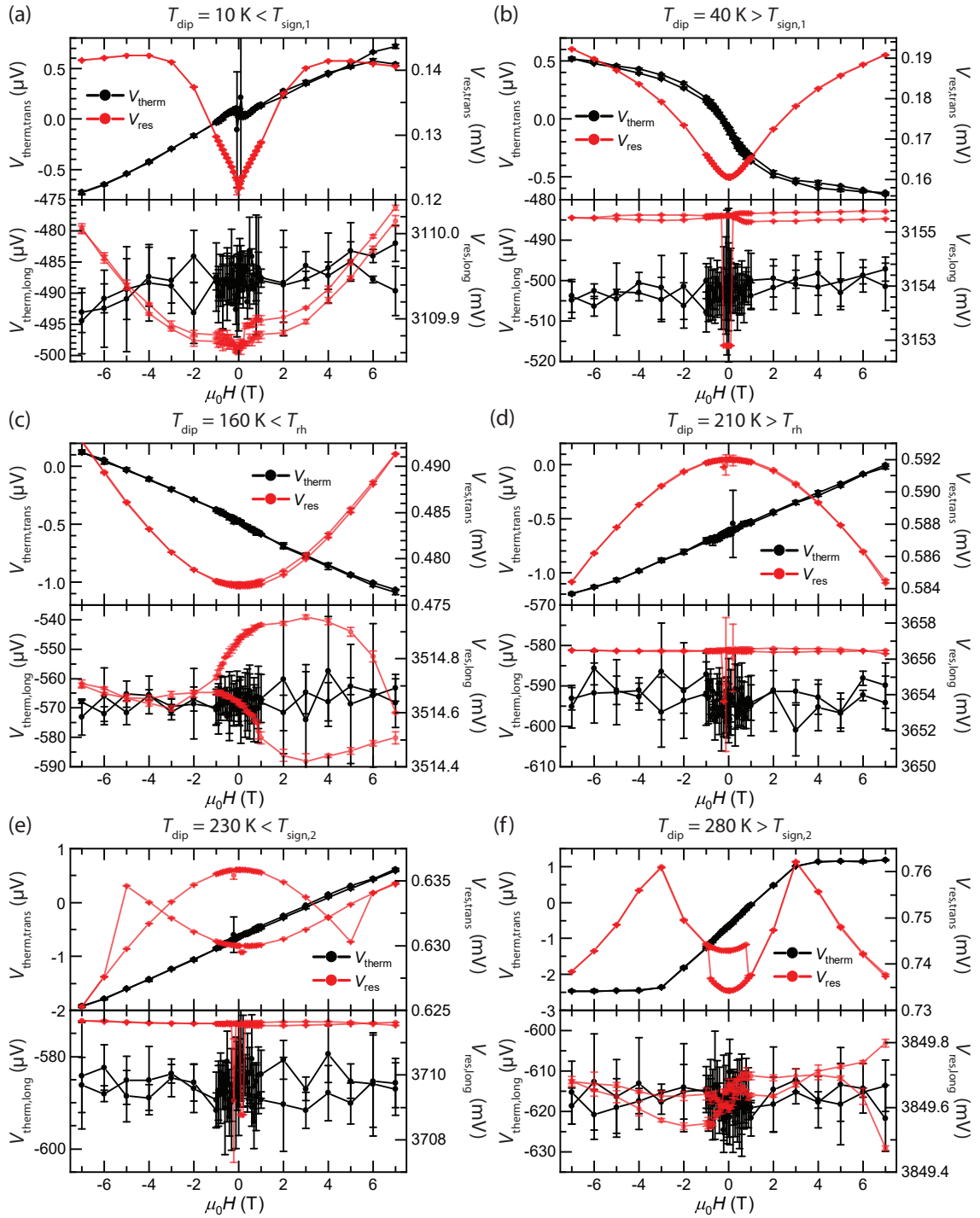
Figure B.0.5.: Thermal (black) and resistive (red) voltage signals measured transverse (upper panels) and longitudinal (lower panels) to the current direction in field-dependent SSE (FD-SSE) experiments using the TbIG (57.6 nm) | Pt (4.1 nm) heterostructure fabricated under an oxygen atmosphere of $p_{O2} = 50\,\mu$bar on a (110)-oriented GGG substrate. The data shown here is measured around the critical temperatures of bulk TbIG ((a),(b) $T_{\mathrm{sign,1,bulk}} = (36 \pm 3)$ K, (c),(d) $T_{\mathrm{rh}} \approx 190$ K, (e),(f) $T_{\mathrm{sign,2,bulk}} = (255 \pm 5)$ K). The transverse thermal voltage signal $V_{\mathrm{therm,trans}}$ is used to calculate the SSE amplitude as a function of the dipstick temperature $V_{\mathrm{SSE}}(T_{\mathrm{dip}})$ shown in Fig. 5.3.1 (d). Overall, the data does not match the expectations, which is mainly originating from the presence of the parasitic crystalline phase TbFeO$_3$ (see Fig. 5.3.1 (a)).
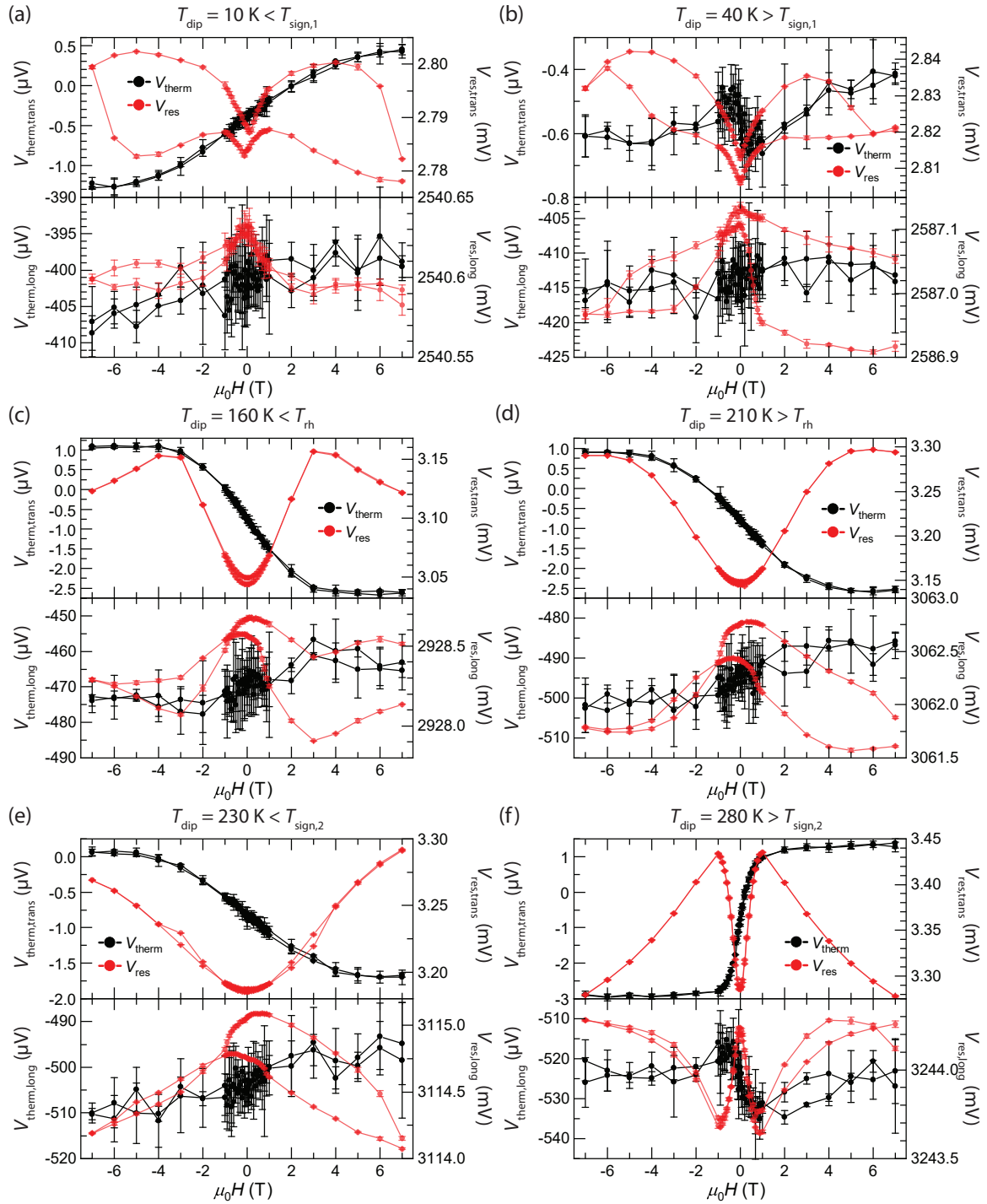
Figure B.0.6.: Thermal (black) and resistive (red) voltage signals measured transverse (upper panels) and longitudinal (lower panels) to the current direction in field-dependent SSE (FD-SSE) experiments using the TbIG (50 nm) | Pt (5.0 nm) heterostructure fabricated under an oxygen atmosphere of $p_{O2} = 25\,\mu\text{bar}$ on a (110)-oriented GGG substrate. The data shown here is measured around the critical temperatures of bulk TbIG ((a),(b) $T_{\text{sign,1,bulk}} = (36 \pm 3)\,\text{K}$, (c),(d) $T_{\text{rh}} \approx 190\,\text{K}$, (e),(f) $T_{\text{sign,2,bulk}} = (255 \pm 5)\,\text{K}$). The transverse thermal voltage signal $V_{\text{therm,trans}}$ is used to calculate the SSE amplitude as a function of the dipstick temperature $V_{\text{SSE}}(T_{\text{dip}})$ shown in Fig. 5.3.1 (e). Overall, the data does not match the expectations, which is mainly originating from the poor sample quality. This is visible in the 2θ-ω-measurement shown in Fig. 5.3.1 (b), where the TbIG-thin film Bragg-reflection is far away from the 2θ-value for the Bragg reflection of a TbIG single crystal which indicates the presence of oxygen vacancies.
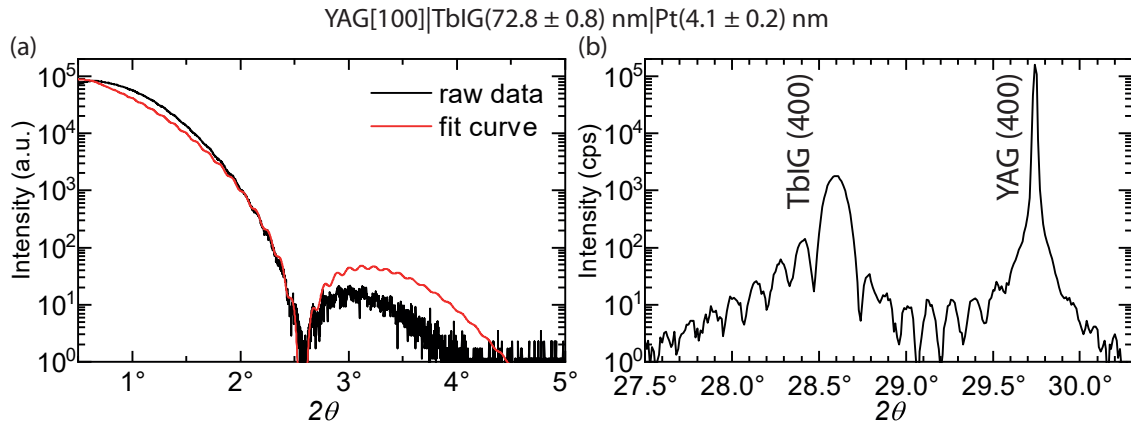
Figure B.0.7.: X-ray diffraction measurements on the TbIG (72.8 nm) | Pt (4.1 nm) heterostructure, which is used for spin Seebeck effect experiments within this work (see section 5.3.4). The heterostructure is fabricated on a (100)-oriented YAG substrate. (a) Reflectometry measurement (black curve) plotted together with the LEPTOS-simulation (red curve). The extracted simulation parameters are $d_{\text{Pt}} = (4.1 \pm 0.2)$ nm and $d_{\text{TbIG}} = (72.8 \pm 0.8)$ nm. (b) 2θ-ω measurement around the (400) YAG substrate Bragg-reflection and the (400) TbIG thin film Bragg-reflection. The proximity of the TbIG thin film Bragg reflection to the bulk value $2\theta_{\text{(400)TbIG,bulk}} = 28.7°$, the high intensity of the TbIG thin film reflection and the pronounced Laue-oscillations are indicators for a high quality crystalline growth of the TbIG (72.8 nm) | Pt (4.1 nm) heterostructure.

Bibliography

[1] M. N. Baibich, J. M. Broto, A. Fert, F. N. Van Dau, F. Petroff, P. Etienne, G. Creuzet, A. Friederich, and J. Chazelas, "Giant Magnetoresistance of (001)Fe/(001)Cr Magnetic Superlattices," *Physical Review Letters*, vol. 61, pp. 2472–2475, nov 1988.

[2] G. Binasch, P. Grünberg, F. Saurenbach, and W. Zinn, "Enhanced magnetoresistance in layered magnetic structures with antiferromagnetic interlayer exchange," *Physical Review B*, vol. 39, pp. 4828–4830, mar 1989.

[3] A. Fert, "Nobel Lecture: Origin, development, and future of spintronics," *Reviews of Modern Physics*, vol. 80, pp. 1517–1530, dec 2008.

[4] C. Chappert, A. Fert, and F. N. Van Dau, "The emergence of spin electronics in data storage," *Nature Materials*, vol. 6, pp. 813–823, nov 2007.

[5] W. Han, S. Maekawa, and X.-C. Xie, "Spin current as a probe of quantum materials," *Nature Materials*, vol. 19, pp. 139–152, feb 2020.

[6] M. Dyakonov and V. Perel, "Current-induced spin orientation of electrons in semiconductors," *Physics Letters A*, vol. 35, pp. 459–460, jul 1971.

[7] M. I. Dyakonov and A. Ioffe, "Possibility of Orienting Electron Spins with Current," *JETP Letters*, vol. 13, no. 11, pp. 467–469, 1971.

[8] Y. K. Kato, "Observation of the Spin Hall Effect in Semiconductors," *Science*, vol. 306, pp. 1910–1913, dec 2004.

[9] K. Uchida, J. Xiao, H. Adachi, J. Ohe, S. Takahashi, J. Ieda, T. Ota, Y. Kajiwara, H. Umezawa, H. Kawai, G. E. W. Bauer, S. Maekawa, and E. Saitoh, "Spin Seebeck insulator," *Nature Materials*, vol. 9, pp. 894–897, nov 2010.

[10] G. E. W. Bauer, E. Saitoh, and B. J. van Wees, "Spin caloritronics," *Nature Materials*, vol. 11, pp. 391–399, may 2012.

[11] L. J. Cornelissen, J. Liu, R. A. Duine, J. B. Youssef, and B. J. van Wees, "Long-distance transport of magnon spin information in a magnetic insulator at room temperature," *Nature Physics*, vol. 11, pp. 1022–1026, dec 2015.

[12] K. Ganzhorn, T. Wimmer, J. Barker, G. E. W. Bauer, Z. Qiu, E. Saitoh, N. Vlietstra, S. Geprägs, R. Gross, H. Huebl, and S. T. B. Goennenwein, "Non-local magnon transport in the compensated ferrimagnet GdIG," may 2017.

[13] S. Datta and B. Das, "Electronic analog of the electro-optic modulator," *Applied Physics Letters*, vol. 56, pp. 665–667, feb 1990.

[14] E.-J. Guo, J. Cramer, A. Kehlberger, C. A. Ferguson, D. A. MacLaren, G. Jakob, and M. Kläui, "Influence of Thickness and Interface on the Low-Temperature Enhancement of the Spin Seebeck Effect in YIG Films," *Physical Review X*, vol. 6, p. 031012, jul 2016.

[15] J. Barker and G. E. W. Bauer, "Thermal Spin Dynamics of Yttrium Iron Garnet," *Physical Review Letters*, vol. 117, p. 217201, nov 2016.

[16] S. Geprägs, A. Kehlberger, F. D. Coletta, Z. Qiu, E.-J. Guo, T. Schulz, C. Mix, S. Meyer, A. Kamra, M. Althammer, H. Huebl, G. Jakob, Y. Ohnuma, H. Adachi, J. Barker, S. Maekawa, G. E. W. Bauer, E. Saitoh, R. Gross, S. T. B. Goennenwein, and M. Kläui, "Origin of the spin Seebeck effect in compensated ferrimagnets," *Nature Communications*, vol. 7, p. 10452, apr 2016.

[17] K. Hagiwara, T. Yano, T. Tanaka, P. K. Das, S. Lorenz, I. Ou, T. Sudo, M. S. Reen, Y. Yamada, T. Mori, T. Kayano, R. Dir, Y. Koshio, M. Sakuda, A. Kimura, S. Nakamura, N. Iwamoto, H. Harada, M. Wurm, W. Focillon, M. Gonin, A. Ali, and G. Collazuol, "Gamma Ray Spectrum from Thermal Neutron Capture on Gadolinium-157," *Exp. Phys*, vol. 2015, p. 0, sep 2018.

[18] F. D. Czeschka, *Spin Currents in Metallic Nanostructures*. Ph.d. thesis, Technische Universität Munchen, 2011.

[19] J. Sinova, S. O. Valenzuela, J. Wunderlich, C. H. Back, and T. Jungwirth, "Spin Hall effects," *Reviews of Modern Physics*, vol. 87, pp. 1213–1260, oct 2015.

[20] S. Hoffman, K. Sato, and Y. Tserkovnyak, "Landau-Lifshitz theory of the longitudinal spin Seebeck effect," *Physical Review B*, vol. 88, p. 064408, aug 2013.

[21] E. F. Bertaut and F. Forrat, "Structure of ferrimagnetic ferrites of rare earths," *C. R. Acd. Sci. Paris*, vol. 242, p. 382, 1956.

[22] F. Tcheou, H. Fuess, and E. F. Bertaut, "I - Parameter refinement at 400 K and magnetic moments at room temperature of some rare earth iron garnets RIG (R = Dy, Er, Yb, Tm) by neutron diffraction," *Solid State Communications*, 1970.

[23] R. Hock, H. Fuess, T. Vogt, and M. Bonnet, "Crystallographic distortion and magnetic structure of terbium iron garnet at low temperatures," *Journal of Solid State Chemistry*, 1990.

[24] R. Pauthenet, "Spontaneous Magnetization of Some Garnet Ferrites and the Aluminum Substituted Garnet Ferrites," *Journal of Applied Physics*, vol. 29, pp. 253–255, mar 1958.

[25] G. F. Dionne, *Magnetic Oxides*. Boston, MA: Springer US, 2009.

[26] T. Kasuya and R. C. Lecraw, "Relaxation mechanisms in ferromagnetic resonance," tech. rep., 1961.

[27] M. Haertinger, C. H. Back, J. Lotze, M. Weiler, S. Geprägs, H. Huebl, S. T. B. Goennenwein, and G. Woltersdorf, "Spin pumping in YIG/Pt bilayers as a function of layer thickness," *Physical Review B*, vol. 92, p. 054437, aug 2015.

[28] A. J. Princep, R. A. Ewings, S. Ward, S. Tóth, C. Dubs, D. Prabhakaran, and A. T. Boothroyd, "The full magnon spectrum of yttrium iron garnet," *npj Quantum Materials*, vol. 2, p. 63, dec 2017.

[29] K. Ganzhorn, J. Barker, R. Schlitz, B. A. Piot, K. Ollefs, F. Guillou, F. Wilhelm, A. Rogalev, M. Opel, M. Althammer, S. Geprägs, H. Huebl, R. Gross, G. E. W. Bauer, and S. T. B. Goennenwein, "Spin Hall magnetoresistance in a canted ferrimagnet," *Physical Review B*, vol. 94, p. 094401, sep 2016.

[30] F. Sayetat, J. Boucherle, and F. Tcheou, "Magnetic structures and magnetoelastic phenomena observed in Tb3GaxFe5-xO12 garnets," *Journal of Magnetism and Magnetic Materials*, vol. 46, pp. 219–232, dec 1984.

[31] D. Rodić and M. Guillot, "The structural properties of Tb3Fe5O12 and growth induced anisotropy," *Journal of Magnetism and Magnetic Materials*, vol. 86, pp. 7–12, apr 1990.

[32] M. Lahoubi, M. Guillot, A. Marchand, F. Tcheou, and E. Roudault, "Double umbrella structure in terbium iron garnet," *IEEE Transactions on Magnetics*, vol. 20, pp. 1518–1520, sep 1984.

[33] M. Lahoubi, "Temperature Evolution of the Double Umbrella Magnetic Structure in Terbium Iron Garnet," in *Neutron Diffraction*, no. 230, InTech, mar 2012.

[34] T. D. Kang, E. Standard, K. H. Ahn, A. A. Sirenko, G. L. Carr, S. Park, Y. J. Choi, M. Ramazanoglu, V. Kiryukhin, and S.-W. Cheong, "Coupling between magnon and ligand-field excitations in magnetoelectric Tb3Fe5O12 garnet," *Physical Review B*, vol. 82, p. 014414, jul 2010.

[35] M. Enderle, "Neutrons and magnetism," *École thématique de la Société Française de la Neutronique*, vol. 13, p. 01002, apr 2014.

[36] "Thermal neutron three-axis spectrometer with polarization analysis IN20." `https://www.ill.eu/users/instruments/instruments-list/in20/characteristics/`. Accessed: 2020-06-02.

[37] S. Toth and B. Lake, "Linear spin wave theory for single-Q incommensurate magnetic structures," *Journal of Physics: Condensed Matter*, vol. 27, p. 166002, apr 2015.

[38] S. Ward and L. Duc, "A crash course on SpinW - Part 1." `https://spinw.org/Ispra2019/#/SpinW`. Accessed: 2019-11-20.

[39] S. Geller and M. Gilleo, "The crystal structure and ferrimagnetism of yttrium-iron garnet, Y3Fe2(FeO4)3," *Journal of Physics and Chemistry of Solids*, vol. 3, pp. 30–36, jan 1957.

[40] D. Rodić, Z. Tomkowicz, L. Novaković, A. Szytula, and M. Napijalo, "The initial magnetic susceptibilities of Gd3Fe5O12 and Tb3Fe5O12 in the compensation point region," *Solid State Communications*, vol. 73, pp. 243–246, jan 1990.

[41] M. Althammer, S. Meyer, H. Nakayama, M. Schreier, S. Altmannshofer, M. Weiler, H. Huebl, S. Geprägs, M. Opel, R. Gross, D. Meier, C. Klewe, T. Kuschel, J.-M. Schmalhorst, G. Reiss, L. Shen, A. Gupta, Y.-T. Chen, G. E. W. Bauer, E. Saitoh, and S. T. B. Goennenwein, "Quantitative study of the spin Hall magnetoresistance in ferromagnetic insulator/normal metal hybrids," *Physical Review B*, vol. 87, p. 224401, jun 2013.

[42] M. Dietlein, *Spin Hall Magnetwiderstand und Spin-Seebeck Effekt in Gd3Fe5O12|Pt Heterostrukturen*. Bachelors thesis, TU München, Walther-Meißner-Institut, 2017.

[43] R. Gross and A. Marx, *Festkörperphysik*. De Gruyter Studium, 2018.

[44] "Welcome to I16 - Diamond Light Source." `https://www.diamond.ac.uk/Instruments/Magnetic-Materials/I16.html`. Accessed: 2020-06-19.

[45] F. Sayetat, "X-ray powder diffraction at low temperature applied to the determination of magnetoelastic properties in terbium iron garnet," *Journal of Applied Physics*, vol. 46, pp. 3619–3625, aug 1975.

[46] H. B. Vasili, M. Gamino, J. Gàzquez, F. Sánchez, M. Valvidares, P. Gargiani, E. Pellegrin, and J. Fontcuberta, "Magnetoresistance in Hybrid Pt/CoFe2O4 Bilayers Controlled by Competing Spin Accumulation and Interfacial Chemical Reconstruction," *ACS Applied Materials & Interfaces*, vol. 10, pp. 12031–12041, apr 2018.

[47] T. D. Kang, E. C. Standard, P. D. Rogers, K. H. Ahn, A. A. Sirenko, A. Dubroka, C. Bernhard, S. Park, Y. J. Choi, and S.-W. Cheong, "Far-infrared spectra of the magnetic exchange resonances and optical phonons and their connection to magnetic and dielectric properties of Dy3Fe5O12 garnet," *Physical Review B*, vol. 86, p. 144112, oct 2012.

[48] F. M. Schade, *Fabrication and Characterization of Y3Fe5O12|Pt|Y3Fe5O12 Trilayers for Spin Current Based Experiments*. Bachelors thesis, TU München, 2013.

[49] K.-W. Nielsen, *Ursache der magnetischen Kopplung in Kobalt-dotiertem ZnO*. Phd thesis, TU München, 2007.

[50] M. McElfresh, *Fundamentals of Magnetism and Magnetic Measurements – Featuring Quantum Design's Magnetic Porperty Measurement System*. 1994.

Acknowledgments

In this last section, I want to thank all those people who supported me during this Master's thesis and made this work possible:

- **Prof Dr. Rudolf Gross** for drawing my interest to magnetism and spintronics during the lecture in solid state physics, for providing the best possible environment at the WMI for this thesis and for all the motivating words.

- **Dr. Stephan Geprägs** for in the first place giving me the opportunity to do my Master's thesis on such an interesting topic. As my supervisor, he supported this thesis with great effort and contributed to my personal development by teaching me scientific methods and a lot of his knowledge in the research field spintronics. Especially, I want to thank him for staying patient despite all the difficulties and providing best support which was making this work possible.

- **Dr. Dan Mannix** for the pleasant, productive and motivating atmosphere during the experiments at ILL in Grenoble.

- **All members of the magnetism group** for the great atmosphere at the WMI, help in the laboratory and insightful discussions.

- **All fellow master students** for the pleasant company in the office, during lunch and coffee breaks as well as for helpful discussions.

- **The WMI staff** for helpful support with all types of problems.